ULTRAFAST OPTICAL RESPONSE AND TRANSPORT PROPERTIES OF STRONTIUM TITANATE-BASED COMPLEX OXIDE NANOSTRUCTURES

by

Lu Chen

B.S., Nankai University, 2012

Submitted to the Graduate Faculty of

the Kenneth P. Dietrich School of Arts and Sciences in partial fulfillment

of the requirements for the degree of

Doctor of Philosophy

University of Pittsburgh

2018

UNIVERSITY OF PITTSBURGH

KENNETH P. DIETRICH SCHOOL OF ARTS AND SCIENCES

This dissertation was presented

by

Lu Chen

It was defended on

November 20th, 2018

and approved by

Jeremy Levy, Professor, Department of Physics & Astronomy

Hrvoje Petek, Professor, Department of Physics & Astronomy

Arthur Kosowsky, Professor, Department of Physics & Astronomy

Roger Mong, Assistant Professor, Department of Physics & Astronomy

Sean Garrett-Roe, Associate Professor, Department of Chemistry

Dissertation Advisor: Jeremy Levy, Professor, Department of Physics & Astronomy

ULTRAFAST OPTICAL RESPONSE AND TRANSPORT PROPERTIES OF STRONTIUM TITANATE-BASED COMPLEX OXIDE NANOSTRUCTURES

Lu Chen, PhD

University of Pittsburgh, 2018

As the silicon-based semiconductor integrated circuits led by Moore's Law approaching their physical limits, the search for a new generation of nanoelectronic and nanophotonic devices is becoming a hot topic in this post-Moore era. The strontium titanate-based complex oxide heterostructure appears to be a promising alternative due to its diverse emergent properties. Being able to control the metal-insulator transition at the polar/nonpolar $LaAlO_3/SrTiO_3$ interface using conductive atomic force microscopy (c-AFM) lithography has made $LaAlO_3/SrTiO_3$, in particular, an attractive platform.

Expanding the class of heterostructures which can be controlled at nanoscale dimensions is important for alternative oxide-based nanodevices. In this dissertation, the writing and erasing of nanostructures at the nonpolar/nonpolar oxide interface of $CaZrO_3/SrTiO_3$ using c-AFM lithography is investigated. Conducting nanostructures as narrow as 1.2 nm at room temperature is achieved. Low-temperature transport measurements based on these nanostructures provide insight into the electronic structure of the $CaZrO_3/SrTiO_3$ interface. Such extreme nanoscale control, with dimensions comparable to most single-walled carbon nanotubes, holds great promise for oxide-based nanoelectronic devices.

Nanophotonic devices operating at terahertz frequencies, on the other hand, offer unique information for many applications. In this dissertation, broadband nanoscale terahertz generators based on c-AFM lithography defined $LaAlO_3/SrTiO_3$ nanojunctions are proved to be able to detect the plasmonic response of a single gold nanorod. By femtosecond pulse shaping using a home-

built pulse shaper, over 100 THz bandwidth selective difference frequency generation at $LaAlO_3/SrTiO_3$ nanojunctions is also demonstrated, which has great potential in both studying fundamental light-matter interaction and realizing selective control of rotational or vibrational resonances in nanoparticles. With this unprecedented control of THz field, the two-dimensional (2D) material graphene and its coupling with the quasi-2D $LaAlO_3/SrTiO_3$ interface are also under investigation. The preliminary data shows evidence for graphene response up to 60 THz. These results help to fill the terahertz gap as well as offer new opportunities for oxide-based nanophotonic devices or even hybrid optoelectronic integrated circuits.

TABLE OF CONTENTS

LIST OF TABLES

LIST OF FIGURES

PREFACE

This dissertation is a summary of my Ph.D. study, which would not be possible without the guidance and help from many people.

First of all, I would like to thank my research advisor, Dr. Jeremy Levy, for his mentorship and support. His passion for research inspired me in so many ways. He is always thinking proactively and constantly coming up with new ideas. I still remember how impressive it was when I first saw the over 100 potential experimental ideas he had listed on Asana. I can't thank him enough for emphasizing the importance of communication and presentation at an early stage of my career, and all those opportunities he has created so I can practice and be better at it. Thank you for a very educational and enlightening graduate research experience. I feel lucky and am grateful to have you as my advisor!

Next, I'd like to thank my beloved labmates, for adding so much fun to this journey. It is such a great memory to share my six years of graduate study with all of you. A special thank you goes to Yanjun Ma, a former graduate student, who not only trained me when I first joined the lab but also was always willing to help even after his graduation. And Erin Sutton, a new graduate student whom I have been working closely with for the past two years, has offered invaluable assistance in building the pulse shaper. I can't wait to see the accomplishment in her own graduate research in the near future.

I would also like to thank my committee, Dr. Hrvoje Petek, Dr. Arthur Kosowsky, Dr. Roger Mong, Dr. Sean Garrett-Roe, and Dr. David Pekker (former committee member) for their commitment and feedback throughout my Ph.D. study. They alerted me when I was making slow

progress or got too obsessed with technical details. I certainly benefitted a lot from all their comments and suggestions.

Without high-quality samples provided by our collaborators, the research for this dissertation is not possible in the first place. So I'd like to thank Dr. Chang-Beom Eom and his group members from the University of Wisconsin, as well as Dr. Nini Pryds and Dr. Yunzhong Chen from the Technical University of Denmark.

A special thanks to my parents, who have always encouraged and supported me to pursue a life I truly wanted. Their unconditional love guided me through numerous difficulties along the way. Last but definitely not least, my dear husband. Thank you for always being there and believing in me, even when I doubted myself. I look forward to continuing this journey knowing that you always have my back.

1.0 INTRODUCTION

The invention of silicon-based integrated circuits in the last century has led to one of the most important industrial revolutions in human history. As the integrated circuits getting smaller and more complex, the current device size is approaching its fundamental limit. Therefore, searching for the next generation material platform is a new driving force for condensed matter physics. One of the promising alternative material systems is the complex oxide heterostructure. The interplay between spin, charge and lattice degrees of freedom in complex oxides gives rise to diverse emergent phases. Additional confinements at the heterostructure interface further bring more exotic properties to the system. The rich physics in complex oxide heterostructures and the capability to control metal-insulator transition at the interface with nanometer-scale resolution make them ideal platforms both for studying fundamental correlated electron interactions and realizing nanoelectronic and nanophotonic devices with higher levels of integration and more functionalities.

Motivated by these points, this dissertation studies the ultrafast optical response and transport properties of strontium titanate-based complex oxide nanostructures, which is arranged as the following: Chapter 1 reviews the material systems and the existing knowledge that are essential to the research in this dissertation. Chapter 2 covers the main instruments involved for experimental measurements. Chapter 3 focuses on creating and erasing nanostructures and use them to study the transport properties at the nonpolar/nonpolar $CaZrO_3/SrTiO_3$ interface. Chapters

4 through 6 present the efforts to probe the response of a single gold nanorod using $LaAlO_3/SrTiO_3$ nanojunctions (Chapter 4), develop a coherent narrow-band terahertz source with a tunability of over 100 THz (Chapter 5), and study the ultrafast response of graphene and its coupling with the $LaAlO_3/SrTiO_3$ interface (Chapter 6). Chapter 7 gives a brief summary and discusses a few possible directions for future experiments.

1.1 STRONTIUM TITANATE-BASED COMPLEX OXIDES

1.1.1 $SrTiO_3$

Strontium titanate $SrTiO_3$ (STO) is a complex oxide material that has a perovskite crystal structure (Figure 1a),[1] with strontium (Sr) atoms on the corners and titanium (Ti) on the center of the lattice. The oxygen (O) atoms are located on each face center of the Sr cube and form an octahedral cage. Bulk STO is a band insulator with an indirect bandgap of 3.25 eV and a direct bandgap of 3.75 eV,[2] making the pristine crystal transparent and colorless. Because of its cubic structure, almost identical refractive index and more than four-fold higher dispersion compared to diamond, STO was once a widely used substitute gemstone.

STO has a lattice constant of 3.905 Å at room temperature. At low temperatures (below 105 K), the cubic structure undergoes an antiferrodistortive transition, where nearby oxygen octahedra rotate in opposite directions, leading to a tetragonal lattice structure (Figure 1b).[1] Domains with tetragonal orientations along x-, y- or z-axis can form within the bulk STO, resulting in ferroelastic domain boundaries. Recent studies have suggested that these naturally formed domain boundaries could potentially play an important role in the transport properties of STO[3]

and STO-based oxide heterostructures.[4, 5] Ferroelastic domains vary from sample to sample and are generally unrepeatable after thermal cycling even within the same sample.[6]

STO is paraelectric at room temperature. When the temperature is further lowered to below 38 K (Figure 1c), STO starts to approach a ferroelectric state but remains paraelectric even at very low temperatures due to quantum fluctuations.[7, 8] However, its proximity to the ferroelectric state, also known as incipient ferroelectric,[9] leads to a dramatic increase in dielectric permittivity from 300 at room temperature to over 20,000 at 4 K.[10, 11] Such large dielectric permittivity makes STO an ideal candidate for effective back-gating substrates. The ferroelectric state can be reached by changing experimental parameters in STO, such as electric field,[12] strain,[8] cation substitution[13] or defects[14].

A density functional theory calculation of the band structure of cubic STO is shown in Figure 1d,[15] where the valence band is primarily derived from oxygen 2*p* orbitals and the conduction band is mainly from titanium 3*d* orbitals with a band minimum at the Γ point.[15, 16] The indirect bandgap corresponds to excitation from *R* to Γ point, while the direct bandgap comes from the Γ to Γ transition. The crystal field splits the 3*d* orbitals into t_{2g} and e_g orbitals. The t_{2g} orbital further split into d_{xy}, d_{yz} and d_{xz} orbitals, sharing the same energy at the Γ point.[15] Dimensional confinements, such as a quasi-2D interface, can lift this degeneracy in the t_{2g} orbital.[17] And if additional confinements are introduced, for instance, in a quasi-1D nanowire, these orbitals can split into subbands.[18] Strain,[19] antiferrodistortive rotation[20] and spin-orbit coupling[21] further complicate the band structure, especially the t_{2g} manifold.

In 1964, Schooley *et al*. reported superconductivity below about 300 mK in reduced STO,[22] making STO the first oxide being observed to be superconductive. The upper critical magnetic field (B_C) is measured to be around 0.2 T[22] and the critical temperature (T_C) is shown

to share a similar dome-shape phase diagram as high-T_C superconductors.[23] STO is also one of the most dilute superconductors, exhibiting superconductivity at a carrier density as low as 10^{17} cm^{-3},[24] which makes it challenging to explain the emergence of superconductivity in STO with the conventional Bardeen-Cooper-Schrieffer (BCS) theory,[25, 26] as the small number of carriers suggests a small Fermi energy. It was proposed that a Bose-Einstein Condensation (BEC) superconductivity may exist in low carrier density Zr-doped STO.[27] This theory predicts that above T_C, electrons are still bonded due to the strong electron-electron attraction even though they are no longer condensed into a superconducting phase.[27] However, even after 50 years of its discovery, the superconductivity in STO still remains largely elusive, demanding more thoroughly invitation into its nature and pairing mechanism.

In addition to the rich transport phenomena, STO also exhibits unparalleled optical properties. Bulk STO is centrosymmetric, leading to a vanished second-order nonlinear susceptibility unless there is a break of the inversion symmetry (such as at the surface or an interface). However, the third-order nonlinear susceptibility in STO has been reported to be exceedingly large, probably the largest among many solid-state materials,[28] making STO a promising platform for realizing nonlinear optical applications.

The closely matched lattice constant to most perovskite oxides grants STO an almost universal substrate for growing various complex oxide heterostructures. Emergent properties rising from the confinement at the oxide interfaces as well as the inherited rich and exotic physics from STO substrate have attracted intense research interest in the past few decades.

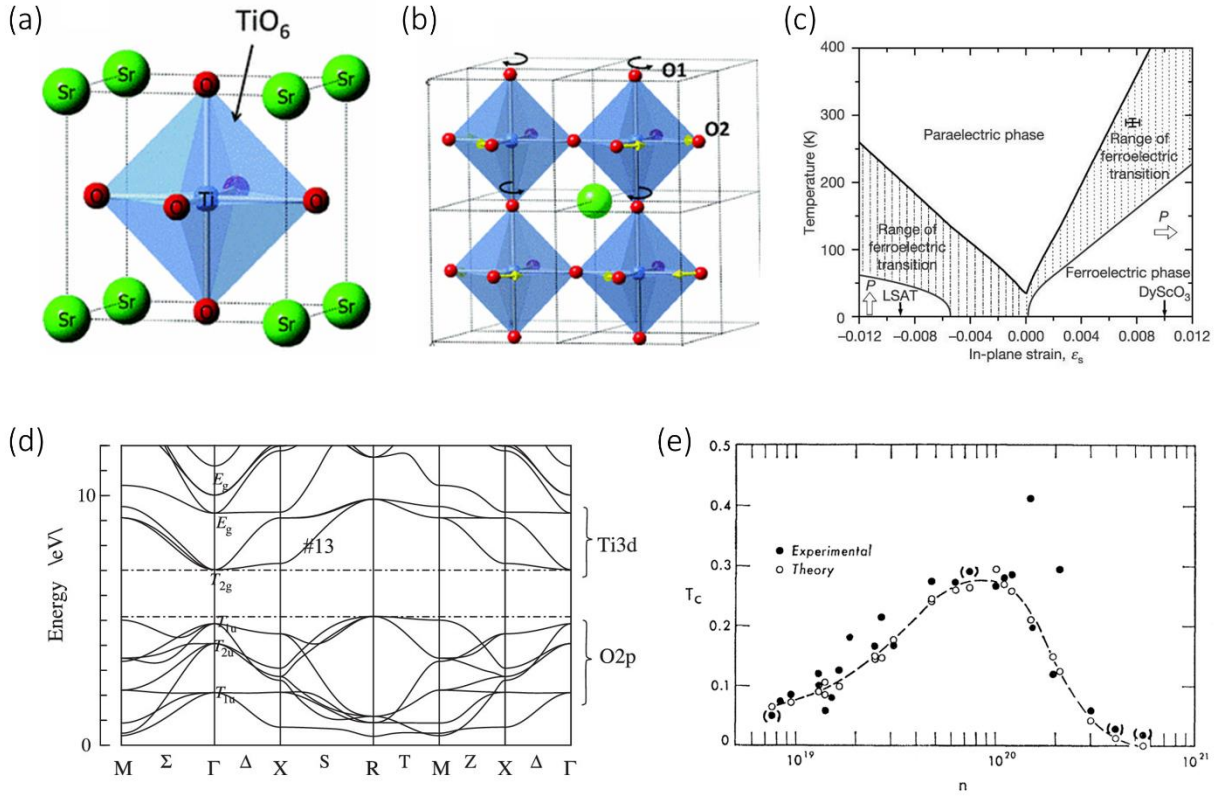

Figure 1 $SrTiO_3$ (STO) crystal structure and properties. (a) STO perovskite crystal structure at room temperature. Ref. [1] (b) Below 105 K, nearby oxygen octahedra in STO rotate in opposite directions, leading to a cubic-to-tetragonal phase transition. Ref. [1] (c) STO starts a paraelectric-to-ferroelectric transition as the temperature is lowered to 38 K, but remains paraelectric due to quantum fluctuations unless applying an in-plane strain. Ref. [8] (d) Density functional theory calculation of the band structure of cubic STO. Ref. [15] (e) The superconducting critical temperature T_C as a function of the carrier density shows a characteristic dome-shape behavior that resembles high-T_C superconductors. Ref. [23]

1.1.2 $LaAlO_3/SrTiO_3$

One of the most celebrated STO-based complex oxide heterostructures is the $LaAlO_3/SrTiO_3$ (LAO/STO) system. Lanthanum aluminate $LaAlO_3$ is another perovskite oxide that has a lattice constant of 3.789 Å, closely matched to STO. LAO is also a band insulator with an indirect bandgap of 5.6 eV. But when LAO is grown on (001) TiO_2-terminated STO by pulsed laser deposition (PLD), a metallic interface can emerge (Figure 2a).[29] As shown in Figure 2b, there is a critical thickness for the LAO layer, around four unit cells, above which the interface between LAO and STO becomes conducting.[30] This conducting region has been experimentally shown to be confined within around 10 nm extending into STO.[31, 32] It is noteworthy that both strain[33] and surface chemistry[34] can shift the critical thickness. Typical carrier density reported in this system is around 5×10^{13} cm^{-2} and the mobility is usually on the order of 10 $cm^2/(Vs)$ at room temperature. High mobility exceeding 10^4 $cm^2/(Vs)$ has been reported at low temperatures for systems with reduced dimensionality.[35] (111) or (110) orientated LAO/STO can also exhibit a conducting interface, but with a different critical thickness of nine or seven unit cells, respectively.[36] On the other hand, SrO-terminated STO, though it is predicted to have a two-dimensional hole system at the LAO/STO interface, has been experimentally found insulating.[29]

Since its discovery in 2004, the origin of the two-dimensional electron system (2DES) at the LAO/STO interface has been extensively debated. Among many possible explanations, the leading mechanism is the polar catastrophe model. Along the [001] direction, LAO can be viewed as alternating LaO^+ and AlO_2^- layers, thus polar, while STO is a series of charge neutral SrO and TiO_2 layers, thus nonpolar. This polar discontinuity leads to a built-in electric field that increases with increasing LAO layer thickness, eventually leading to an electronic reconstruction, where

half an electron per unit cell is transferred to the interface, forming an n-type conducting 2DES.[37] While this model has been quite successful at explaining the formation and critical thickness of the 2DES, it also poses several issues, for example, the inconsistency between the predicted carrier density (3.2×10^{14} cm^{-2}) and the experimentally measured value. Other possible explanations, such as oxygen vacancies,[38] cation intermixing,[39] stoichiometry,[40] surface adsorbates[34] and strain,[41] have been proposed. There are also several attempts to explain the 2DES with a hybrid mechanism involving more than one processes.[42] But until now, this fundamental question of the conductivity mechanism still remains an open question.

When the LAO layer is slightly below the critical thickness, the interface is insulating but highly tunable. Figure 2d shows that the interface can undergo a metal-insulator phase transition at room temperature by applying ±100 V to the back of the STO substrate, and the conducting or insulating behavior persists even after the back gate voltage is removed.[30] Conductive atomic force microscopy (c-AFM) lithography can locally control the metal-insulator transition with nanometer-scale precision,[43] which will be discussed in details in Chapter 2.

Besides the emergence of the conducting 2DES and tunable metal-insulator transition, a variety of remarkable phenomena like interfacial superconductivity,[44] low temperature[45] and room temperature magnetism,[46] Rashba spin-orbit coupling,[47] and even coexistence of superconductivity and magnetism[48] have also been observed in the rich LAO/STO system.

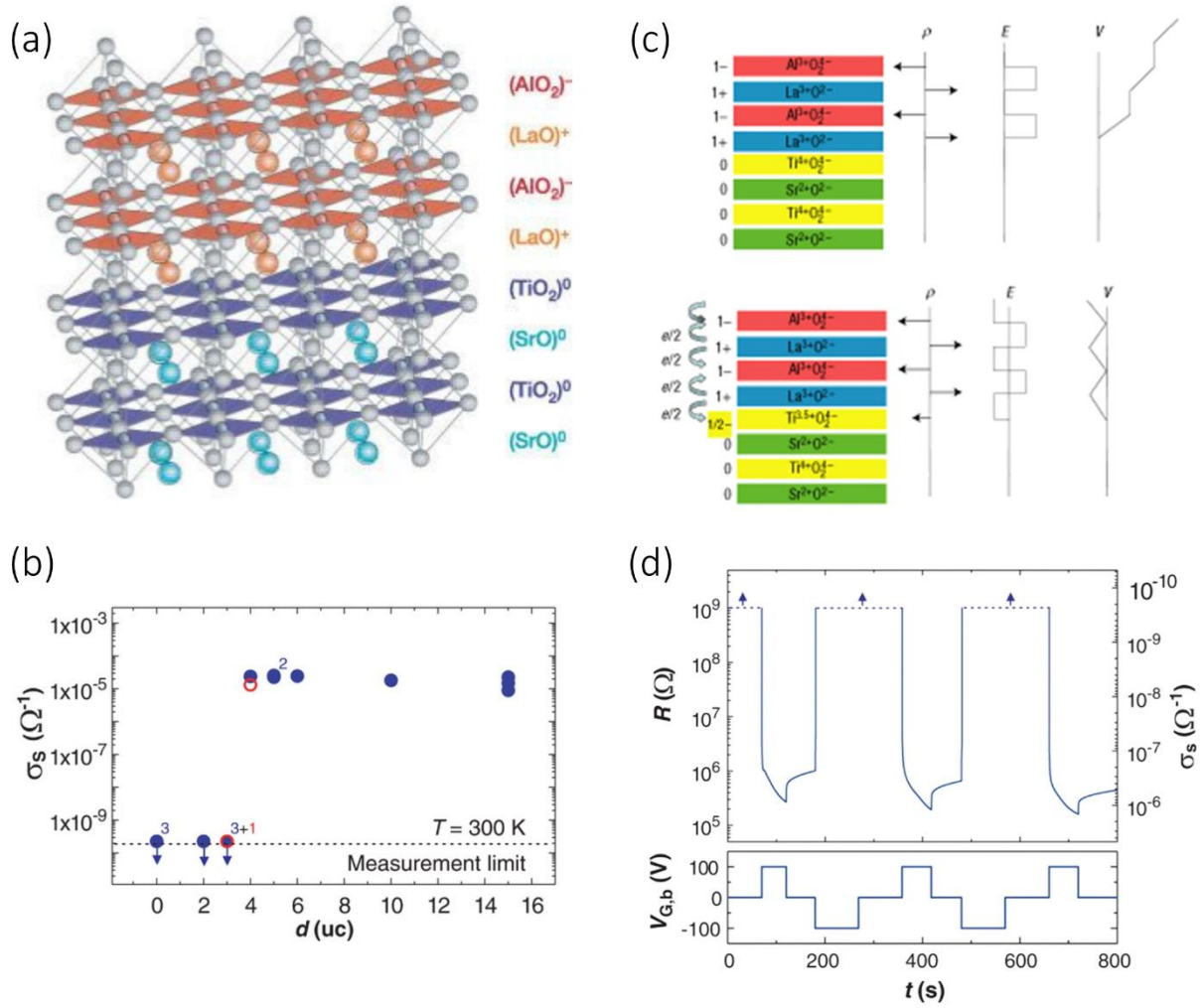

Figure 2 Two dimensional electron system (2DES) at the interface of $LaAlO_3/SrTiO_3$ (LAO/STO). (a) Schematic drawing of the LAO/STO heterostructure. Ref. [29] (b) Sheet conductance as a function of the LAO layer thickness. The interface turns into metallic for LAO layers above four unit cells. Ref. [30] (c) The polar catastrophe model for TiO_2-terminated STO. Half an electron per unit cell is transferred to the interface to compensate for the built-in electric filed from the polar discontinuity. Ref. [37] (d) Sheet resistance as a function of applied back gate voltage showing electric field tunable metal-insulator transition. Ref. [30]

1.1.3 $CaZrO_3/SrTiO_3$

$CaZrO_3/SrTiO_3$ (CZO/STO) is a new member to the family of complex oxide heterostructures with a conducting interface. A 2DES was first experimentally realized by Chen *et al.* in 2015 (Figure 3).[49] Unlike LAO, (001) calcium zirconate $CaZrO_3$ is a nonpolar material. The observed 2DES was attributed to the compressive strain induced polarization.[49] Later, two theoretical calculations using first-principle analysis further confirmed the role of polarization discontinuity.[50, 51]

Like LAO and STO, CZO is a band insulator with a bandgap around 4.1 eV. It has a lattice constant of 4.012 Å, leading to +2.67% lattice mismatch to the STO substrate. As a result, the CZO epitaxial thin film experiences a compressive biaxial strain, causing both Ca^{2+} and Zr^{4+} cations to displace towards the interface in the first few unit cells of CZO (Figure 3b).[49] The lattice distortion results in a polarization pointing towards the interface, providing the driving force to collect electrons from surface donors to form an n-type 2DES at the CZO/STO interface. A critical thickness of seven unit cells has also been observed in this system (Figure 3c), which can be elaborated by the band diagram in Figure 3d.[49] The strain induced polarization generates an electric field across the CZO film, which will bend the electronic bands. As the CZO layer thickness increases, a crossover of the surface donor states and the STO conduction band minimum is reached once the CZO layer is above the critical thickness. Electrons then transfer from donor states to the STO conduction band.[49]

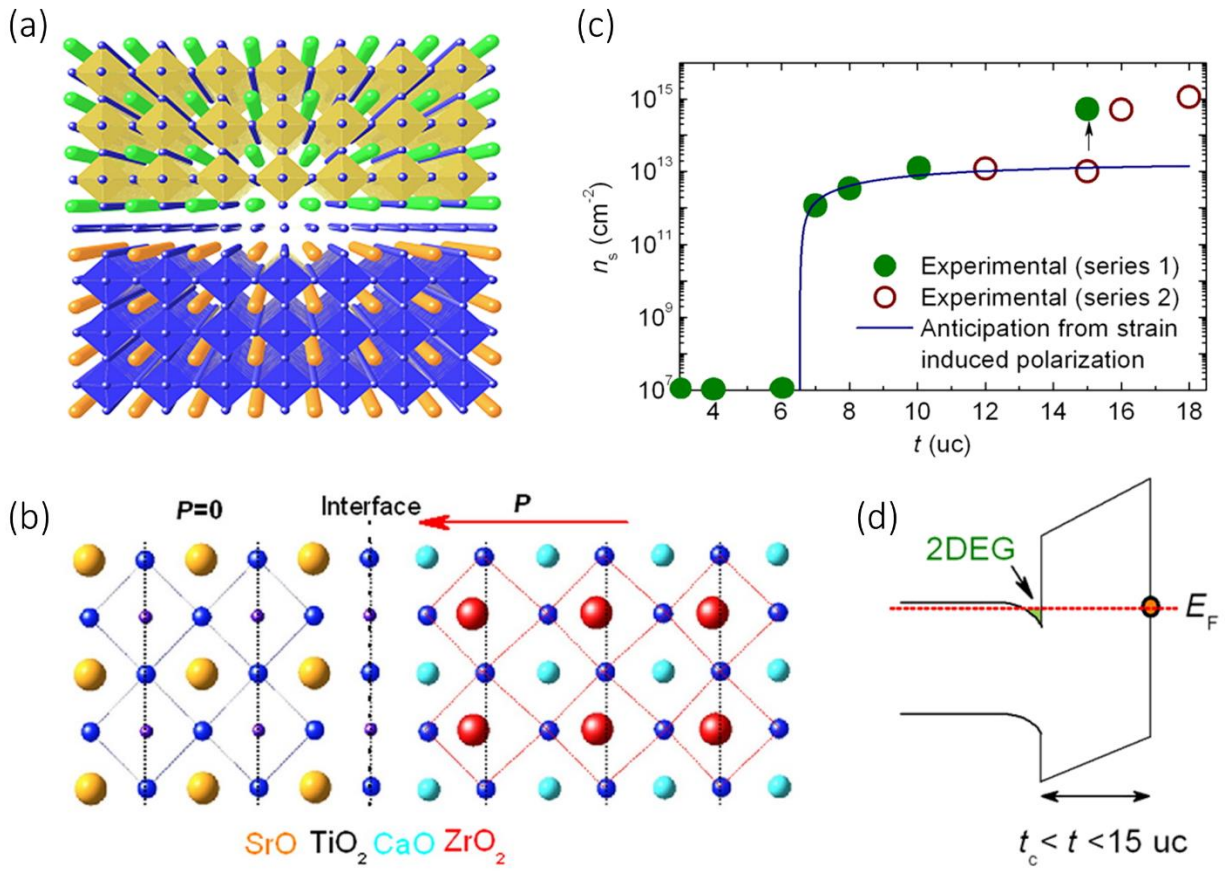

Figure 3 2DES at the $CaZrO_3/SrTiO_3$ (CZO/STO) interface. (a) Schematic drawing of the CZO/STO heterostructure. (b) Polarization discontinuity model. The lattice constant mismatch between CZO and STO induces a lattice distortion near the interface, which produces a polarization pointing towards the interface, driving electrons from surface donors to form an n-type 2DES at the interface. (c) The sheet carrier density as a function of the CZO layer thickness. A critical thickness of seven unit cells is shown. (d) Schematic band diagram when the CZO layer is above the critical thickness. Ref. [49]

1.2 TRANSPORT PROPERTIES

1.2.1 Superconductivity

Superconductivity refers to a phenomenon of zero electrical resistance and magnetic flux exclusion in certain materials below a critical temperature. It was first discovered in mercury in 1911 and has since remained in the center of the research spotlight due to its unparalleled potential in electric power transmission, medicine, ground transportation, quantum computing, and so on. Though the extensive experimental and theoretical studies have led to numerous advances in this field, even rewarded more than a dozen Nobel prizes, the fundamental physics for superconductivity, especially high-temperature superconductivity, is still a mystery.

The core of superconductivity is electron pairing. Conventional BCS theory is the first microscopic theory for superconductivity and was proposed by Bardeen, Cooper, and Schrieffer in 1957.[25] It describes the superconductivity by phonon-mediated weak attractive electron-electron interactions, in which electrons form weakly bonded pairs, known as Cooper pairs. Below the critical temperature, those Cooper pairs condense into a coherent superconducting phase, where all pairs share the same wavefunction. A direct consequence is that the average Cooper pair size is much larger than the distance between electrons. Most traditional superconductors can be well accounted for using the BCS theory. However, it is believed that this theory itself cannot fully explain the phenomenon of high-T_C superconductors.

The BEC theory, on the other hand, describes the superconductivity with tightly bonded electron pairs. The strong attractive interaction leads to a small pair size. Strongly paired electrons form superconductivity when the temperature is lowered below the BEC transition temperature. In 1969, Eagles *et al.* proposed that electrons can remain paired above T_C in Zr-doped STO.[27]

Evidence favoring the unconventional BEC regime has recently been reported in LAO/STO nanowires, where electron pairing without superconductivity was observed.[52]

Understanding the underlying physics for superconductivity, especially high-T_C superconductivity, is central to realizing room temperature superconductors. The extremely low carrier density at which STO exhibits superconductivity and the similarity of its phase diagram to the high-T_C superconductors, together with new opportunities stemming from additional confinement in STO-based heterostructures, imply that the STO-based complex oxide may serve as a promising platform for uncovering this century-long mystery.

1.2.2 Ballistic transport

When talking about transport properties, there are three relevant length scales: the elastic scattering length l_e, the inelastic scattering length l_{in}, and the phase coherence length l_φ.[53] The elastic scattering length, or equivalently, the elastic mean free path, is the average distance an electron can travel ballistically between successive elastic collisions. These collisions happen due to the irregularities in the conductor, such as impurities or dislocations. Elastic collisions only change the electron travelling direction, but keep its kinetic energy conserved. They also don't randomize the electron phase, instead, the phase is only shifted by a well-defined and repeatable value. If a device has a length scale shorter than the elastic scattering length, its electron transport properties are considered ballistic, otherwise, they are diffusive. As can be expected, the electrical mobility μ directly relates to the elastic scattering length by

$$\mu = \frac{e l_e}{m^* v_F} \tag{1.1}$$

where e is the electron charge, m^* is the effective mass and v_F is the Fermi velocity of the electron.

Conversely, inelastic scattering length, or inelastic mean free path, refers to the average distance between subsequent inelastic collisions, such as electron-phonon scattering or electron-electron scattering. Energy transfers occur during inelastic collisions, and electron phase is randomized.

Phase coherence length is a measure of the distance electrons can travel coherently before the phase information is lost. It is worth mentioning that, l_{φ} and l_{in} are not always the same. An electron may lose its phase without transferring energy in certain scatterings, for example, spin-flip scattering. If the device length scale is smaller than the phase coherence length, then electrons are expected to behave quantum mechanically.

The ballistic regime is essential for studying the nature of electron-electron interactions and phenomena related to wave properties of electrons. Ballistic transport is usually observed in 1D or quasi-1D systems, such as metal nanowires, carbon nanotubes or point contacts, leading to quantized conductance in the unit of e^2/h, where e is the electron charge and h is Planck's constant.[54] However, the extreme sensitivity to even a minimum amount of disorders in these narrow structures[55] poses enormous challenges to extend the ballistic regime to micrometer scales or beyond. One way to overcome this limit has been proposed to involve attractive electron-electron interactions.[56]

1.3 ULTRAFAST OPTICS

Ultrafast optical process deals with phenomena that occur on picosecond or femtosecond time scale, revealing information related to the ultrafast dynamics in a material or system that would otherwise be inaccessible. Ultrafast optical experiments rely on short optical pulses generated by

ultrafast lasers. The spectral and temporal profiles of the ultrafast pulse are thus essential to a specific ultrafast optical process.

1.3.1 Ultrafast laser

The word "LASER" is actually an acronym for "Light Amplification by Stimulated Emission of Radiation". Ever since its first realization in 1960,[57] laser has been an irreplaceable building block of numerous research and industrial applications due to its high power and unique coherence nature. In general, there are two types of lasers based on their energy temporal distribution, namely the continuous-wave (CW) laser and the pulsed laser. The pulsed laser generates a train of short pulses mostly through mode-locking, in which a fixed phase relationship is introduced between longitudinal modes supported by the laser cavity.

A laser cavity works as a resonator that allows an infinite set of resonance frequencies in steps of $c/2L$, where c is the speed of light and L is the optical length of the cavity. The supported resonance frequencies are often referred to as longitudinal modes. In practice, the frequency range over which a laser can actually oscillate is determined by the gain bandwidth of the gain material as well as the total loss in the cavity (Figure 4a). Among diverse available gain materials, titanium-doped sapphire (Ti: Sapphire) crystal provides a broad gain bandwidth from 650 nm to 1100 nm, making Ti: Sapphire crystal the most widely used gain medium for ultrafast solid-state lasers.

In general, the phase relationship between the oscillating modes are random and the laser output fluctuates with time. In order to generate a well-defined train of pulses, the relative phase between all the modes need to be locked, and that is how the term "mode-lock" comes in. There are two ways to generate mode-locking, either active or passive. Active mode-locking introduces a periodic modulation of the cavity loss through an acousto-optic modulator or electro-optical

modulator.[58] The modulation is synchronized with the cavity roundtrip period so that the longitudinal modes lock their phases to the modulation. The physical picture is equivalent to all the energy concentrated to a single pulse that traveling back and forth inside the laser cavity. Pulses produced using active mode-locking are usually on the order of picoseconds.

Passive mode-locking, on the other hand, utilizes the nonlinear process to modulate the cavity loss. Before the development of Ti: Sapphire ultrafast laser, adding a saturable absorber was the most common implementation for realizing passive mode-locking.[59] The combined action of the saturable absorber and the gain medium leads to more losses for lower intensity wings, while keep amplifying the high-intensity peak of the pulse until a self-consistent pulse shape is reached.

For Ti: Sapphire ultrafast laser, no additional saturable absorber is required. The mode-locking is achieved through the Kerr lensing effect in Ti: Sapphire crystals.[60] The Ti: Sapphire crystal has a nonlinear refractive index $n = n_1 + n_2 I$, where I is the intensity of light, n_1 and n_2 are the linear and nonlinear refractive index, respectively. Higher intensity thus experiences a higher refractive index. The laser beam has a Gaussian transverse distribution, as shown in Figure 4b. The Ti: Sapphire crystal acts as an effective lens, providing self-focusing as the beam goes through the crystal. The higher intensity portion are subject to less losses due to the smaller size. After travelling back and forth several times, the pulse will research an equilibrium state. Sub-picosecond pulses can be achieved through this process. Further shortening of the pulse is limited by the dispersion inside the cavity. To generate sub-10 fs ultrashort pulses, intracavity group velocity dispersion (GVD) needs to be carefully compensated. Prism pairs and chirped mirrors are often used for precise control of the intracavity GVD.[61] In Chapter 5, a state-of-art sub-7 fs Ti: Sapphire oscillator (Spectra-Physics Rainbow 2 UHP) is used.

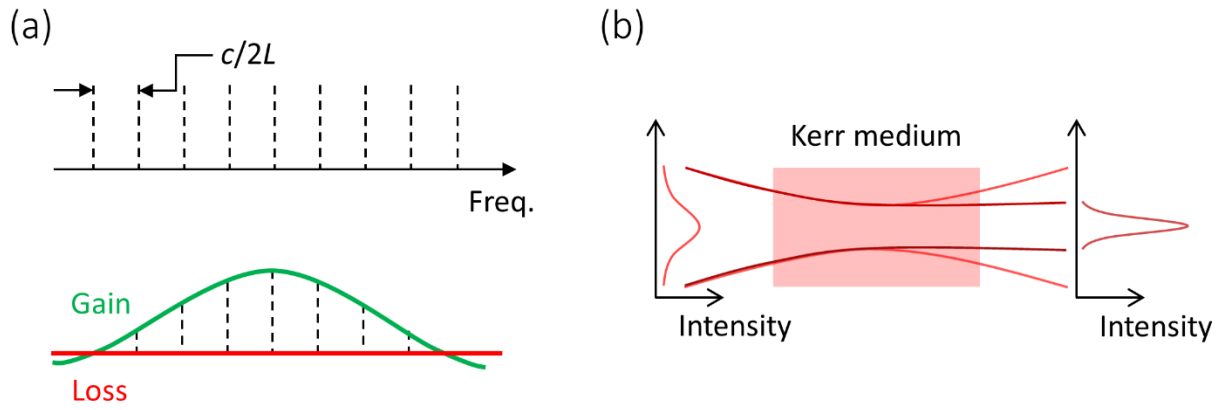

Figure 4 Ultrafast laser. (a) Longitudinal modes supported by a laser cavity (upper) and actually oscillating modes determined by the gain bandwidth of the gain medium as well as the total loss in the cavity (bottom). (b) Kerr lensing effect. The center portion in a Gaussian beam with higher light intensity experiences a self-focusing effect due to the nonlinear refractive index in a Kerr medium.

1.3.2 Pulse characterization

It is important to characterize the properties of an ultrafast pulse before taking measurements to establish the experimental condition. The extreme time scale of ultrafast pulses is way beyond the response time and dynamic range of most optoelectronic devices, especially when it comes to sub-10 fs pulses, thus all-optical methods are introduced, where a replica of the pulse is used to measure itself.

1.3.2.1 Coarse estimation of the pulse duration

Field autocorrelation

The field autocorrelation is defined as

$$\int_{-\infty}^{\infty} E(t)E^*(t-\tau)\,dt \tag{1.2}$$

where $E(t)$ is the electric field of light and τ is the time delay between the two fields. An example schematic diagram for measuring field autocorrelation is shown in Figure 5a. The incoming ultrafast pulses are split into two beams, with pulses in one beam delayed with respect to the other by time τ. Then the two beams are combined and the total field intensity is detected by a linear photodetector.

If we assume the input pulse is Gaussian

$$E_{in}(t) = E_0 e^{-(t/t_p)^2} e^{i\omega_c t} \tag{1.3}$$

where t_p is the pulse width, E_0 is the amplitude and ω_c is the central angular frequency of the pulse wave. Then the total field reaches the linear photodetector is

$$E(t) = \frac{E_{in}(t) + E_{in}(t-\tau)}{2} \tag{1.4}$$

The linear photodetector measures the intensity $I(\tau)$ of this field, and since the response time of a photodetector is much longer than the pulse duration, an integral of t from -∞ to ∞ is needed:

$$\begin{aligned} I(\tau) &= \int_{-\infty}^{\infty} E(t)E^*(t)\,dt \\ &= \frac{1}{4}\left(\int_{-\infty}^{\infty} \left(E_{in}(t)E_{in}^*(t) + E_{in}(t-\tau)E_{in}^*(t-\tau)\right) dt \right. \\ &\quad \left. + 2\int_{-\infty}^{\infty} E_{in}(t)E_{in}^*(t-\tau)\,dt\right) \end{aligned} \tag{1.5}$$

In which the first term is simply the total intensity of each beam, and the second term is the field autocorrelation defined above. After substituting Eq. 1.3 into Eq. 1.5 and simplifying the result, the measured intensity reads

$$I(\tau) = \sqrt{\frac{\pi}{2}}\frac{E_0^2}{8} t_p \left(1 + e^{-\tau^2/2t_p^2}\cos(\omega_c \tau)\right) \tag{1.6}$$

A normalized plot of Eq. 1.6 is shown in Figure 5b, with t_p = 10 fs. Note the ratio

$$\frac{I(\infty)}{I(0)} = \frac{1}{2} \tag{1.7}$$

The Fourier transform of field autocorrelation is exactly the pulse spectrum, so field autocorrelation provides information only relates to the spectral amplitude, without any phase information. However, the field autocorrelation is sensitive to chirp. If a pulse is chirped, its field autocorrelation is narrower than the unchirped counterpart.

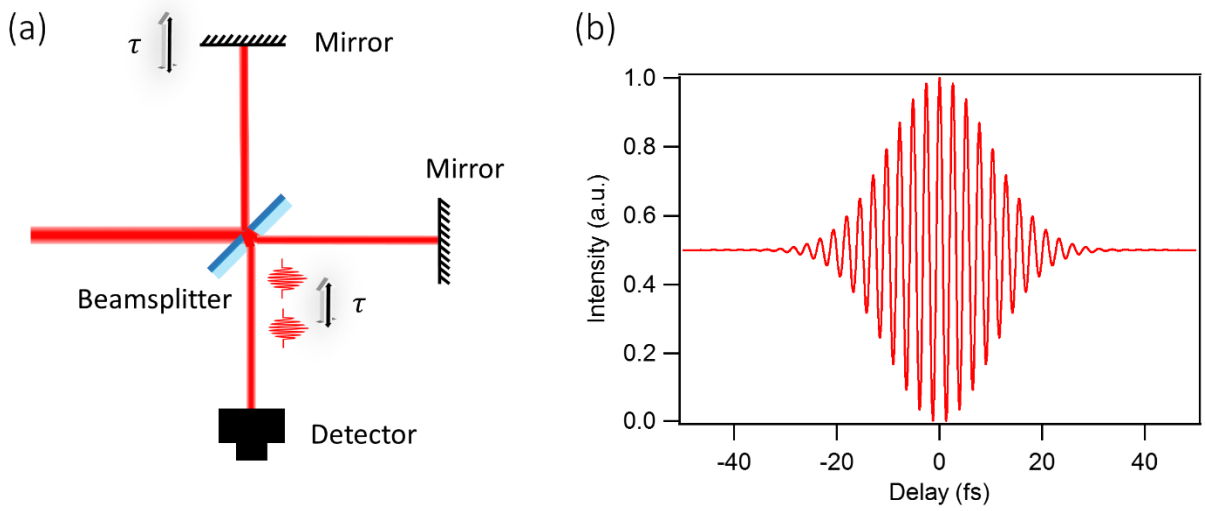

Figure 5 Field autocorrelation. (a) Schematic diagram for a field autocorrelation setup. (b) Normalized field autocorrelation signal as a function of time delay between the two beams.

Intensity autocorrelation

The intensity autocorrelation is defined as

$$\int_{-\infty}^{\infty} I(t)I(t-\tau)\,dt \tag{1.8}$$

which can be achieved by adding a nonlinear crystal (e.g. second-harmonic crystal), and using a non-collinear optical setup as shown in Figure 6a. In this case, one beam is again delayed by τ compared to the other beam before both of them are focused onto the second-harmonic crystal. The generated frequency doubled signal is then detected by a linear photodetector. The non-collinear configuration assures that only the nonlinear signal is detected without interference from the fundamental pulses, which is also often referred to as the "background-free" scheme.

The generated second-order nonlinear field is proportional to

$$E_2(t,\tau) \sim P = \varepsilon_0 \chi^{(2)} E(t) E(t-\tau) \tag{1.9}$$

So the measured intensity of $E_2(t,\tau)$ by the linear photodetector as a function of time delay τ leads to

$$I(\tau) = \int_{-\infty}^{\infty} E_2(t,\tau)E_2^*(t,\tau)\,dt \sim \int_{-\infty}^{\infty} E(t)E(t-\tau)E^*(t)E^*(t-\tau)dt = \int_{-\infty}^{\infty} I(t)I(t-\tau)\,dt \tag{1.10}$$

Again, using the Gaussian input pulse as an example, the intensity autocorrelation gives

$$I(\tau) \sim \frac{\sqrt{\pi}E_0^4}{8} t_p e^{-\left(\frac{\tau}{t_p}\right)^2} \tag{1.11}$$

A normalized plot of the intensity autocorrelation with t_p = 10 fs is shown in Figure 6b.

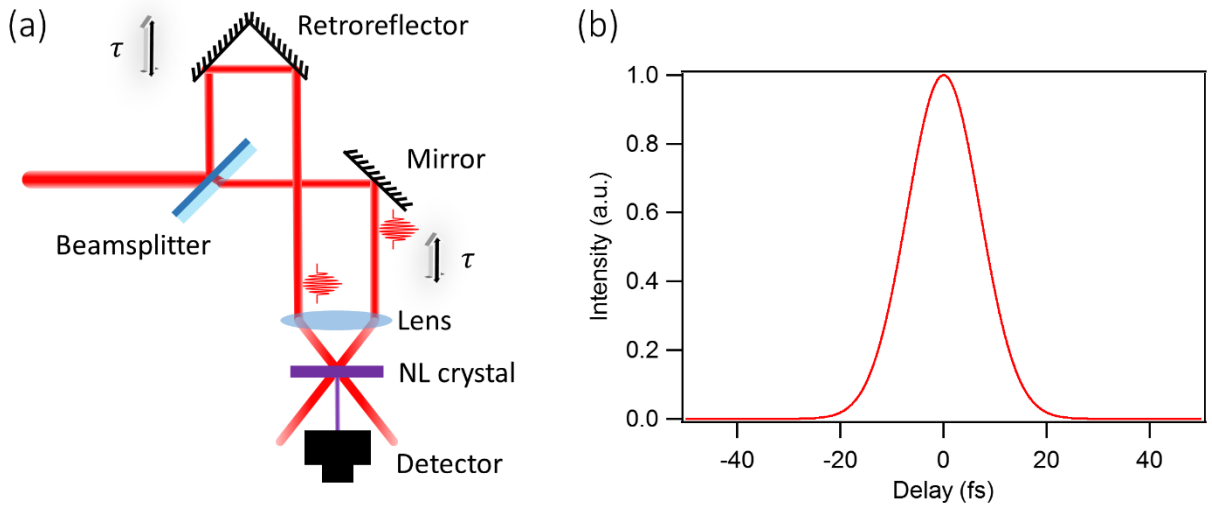

Figure 6 Intensity autocorrelation. (a) Schematic diagram for a non-collinear intensity autocorrelation setup. (b) Normalized intensity autocorrelation signal as a function of time delay between the two beams.

The intensity autocorrelation is often used as a measure of the pulse duration. Its full width at half-maximum (FWHM) has a certain ratio to the pulse width depending on the pulse shape, as examples are shown in Table 1 for two most common pulse profiles. Though the intensity autocorrelation is widely used as a coarse estimation for the pulse duration, it is not sensitive to chirp and has no information regarding the pulse phase. It also tends to underestimate the pulse width if the pulse stability is poor.

Table 1 Pulse parameters for different pulse shape profiles

Shape	Gaussian	Hyperbolic Secant
Electric field	$e^{-(t/t_p)^2}$	$sech(t/t_p)$
Intensity Profile $S(t)$	$e^{-2(t/t_p)^2}$	$sech^2(t/t_p)$
FWHM for $S(t)$: Δt	$1.177t_p$	$1.763t_p$
Intensity Autocorrelation $I(\tau)$	$e^{-(\tau/t_p)^2}$	$\frac{3\frac{\tau}{t_p}\left(\cosh\left(\frac{\tau}{t_p}\right)-\sinh\left(\frac{\tau}{t_p}\right)\right)}{\sinh\left(\frac{\tau}{t_p}\right)^3}$
FWHM for $I(\tau)$: $\Delta\tau$	$1.665t_p$	$2.720t_p$
Spectral Profile $S(\omega)$	$e^{-(\omega t_p)^2/2}$	$sech^2(\pi\omega t_p/2)$
FWHM for $S(\omega)$: $\Delta\omega$	$2.355/t_p$	$1.122/t_p$
$\Delta\omega\Delta t$	2.772	1.978

Other methods to measure the intensity autocorrelation involve a collinear geometry but with orthogonal input polarizations, or averaging over an interferometric autocorrelation signal, which will be discussed in detail below.

Interferometric autocorrelation

In general, there are two ways to measure the interferometric autocorrelation in a collinear geometry, either with a nonlinear crystal in front of a linear detector or directly use a nonlinear (e.g. two-photon absorption, optical rectification, *et al.*) detector. A schematic setup of the first configuration is shown in Figure 7a.

The total field reaching the nonlinear crystal can again be expressed as Eq. 1.4, and the second-order nonlinear process in the crystal gives

$$E_2(t,\tau) \sim P = \varepsilon_0 \chi^{(2)} E(t) E(t) \tag{1.12}$$

The detected interferometric autocorrelation intensity at the linear detector then leads to

$$\begin{aligned} I(\tau) &= \int_{-\infty}^{\infty} E_2(t,\tau) E_2^*(t,\tau)\, dt \\ &= \frac{1}{16} \int_{-\infty}^{\infty} \big(E(t) + E(t-\tau)\big)^2 \big(E(t) + E(t-\tau)\big)^{2*}\, dt \\ &\sim \frac{\sqrt{\pi} E_0^4}{256} t_p \left(1 + 2e^{-\tau^2/t_p^2} + 4e^{-3\tau^2/4t_p^2} \cos(\omega_c \tau) + e^{-\tau^2/t_p^2} \cos(2\omega_c \tau)\right) \end{aligned} \tag{1.13}$$

Figure 7 shows the normalized interferometric autocorrelation intensity for a Gaussian pulse with t_p = 10 fs. Note the ratio

$$\frac{I(\infty)}{I(0)} = \frac{1}{8} \tag{1.14}$$

The interferometric autocorrelation is the only autocorrelation signal that contains phase information. And like the field autocorrelation, it is also sensitive to chirp, leading to an underestimation of the pulse width if chirp exists in the pulse. Though the interferometric autocorrelation can provide some information about the phase, extracting full spectrum and phase from only the interferometric autocorrelation is difficult, as completely different pulses sometimes can give very similar interferometric autocorrelation results.

A cross-check between the measured pulse spectral width and temporal width can help to gain some confidence in the autocorrelation derived pulse duration. The measured FWHM of the laser spectrum, $\Delta\omega$ is related to the measured pulse width Δt through Fourier transform. If no distortion or system error is present, the product of $\Delta\omega$ and Δt should be very close to the shape-dependent value listed in Table 1. Any large deviation from this value alarms unaccounted problems.

Autocorrelations can generate a coarse estimation of the pulse duration, and in some cases with limited phase information, provided that the pulse shape is known or assumed. More sophisticated methods need to be employed to acquire a complete characterization of the pulse amplitude and phase, especially when the pulse width is below 10 fs.

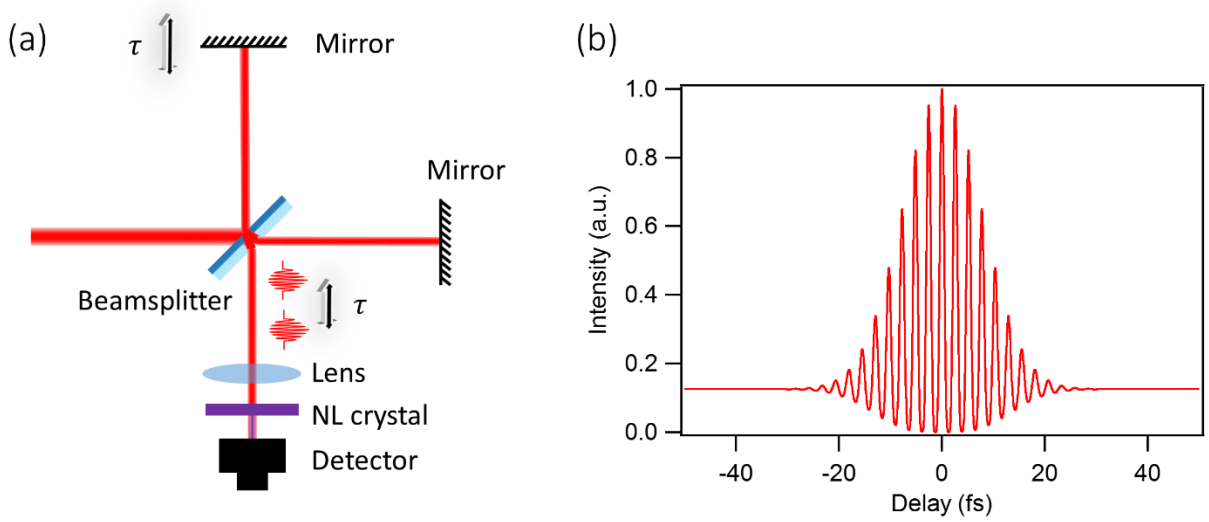

Figure 7 Interferometric autocorrelation. (a) Schematic diagram for an interferometric autocorrelation setup. (b) Normalized interferometric autocorrelation signal as a function of time delay between the two beams.

1.3.2.2 Complete characterization of the pulse amplitude and phase

A pulse can be fully described by its amplitude and phase. With the ultrafast pulse playing an increasingly important role in both fundamental research and daily application, new methods for a complete characterization of few-cycle pulses are constantly being developed and perfected. Below we will discuss several most successful and widely used schemes.

Frequency-Resolved Optical Gating (FROG)

The frequency-resolved optical gating (FROG) was first introduced in 1993.[62] Numerous variations have since been developed for different applications, such as GRENOUILLE and XFROG, but the main idea relies on introducing an ultrafast gate function through the nonlinear process to measure the pulse. A simplified schematic drawing of the FROG measurement is illustrated in Figure 8. The unknown pulses are split into a gate pulse and a probe pulse, with the gate pulse delayed by certain time τ. Unlike the aforementioned autocorrelation techniques, where only the intensity of the nonlinear process is measured, the resulting nonlinear correlation is spectrally resolved using a spectrometer at different time delay τ. As a result, the FROG trace is plotted in a two-dimensional intensity graph as a function of both frequency ω and delay τ. The amplitude and phase of the input pulse can then be retrieved from the FROG trace using an iterative reconstruction algorithm.[62]

For example, if a frequency doubling crystal is used for the nonlinear process, which is also called "SHG FROG", then the linear detector (e.g. a CCD array) maps the FROG trace as

$$I_{FROG}(\omega,\tau) = \left| \int_{-\infty}^{\infty} E(t)E(t-\tau)e^{-i\omega t}dt \right|^2 \tag{1.15}$$

where $E(t)$ is the field of the probe pulse, $E(t\text{-}\tau)$ is the field of the gate pulse, and $e^{-i\omega t}$ comes from taking Fourier transform to convert the time-domain signal to the frequency-domain.

In a FROG measurement, a large amount of data points is taken, usually much more than the required number to extract the complex electric field. This greatly reduces the necessity for each data point to be strictly accurate, thus FROG is a noise-insensitive measurement.

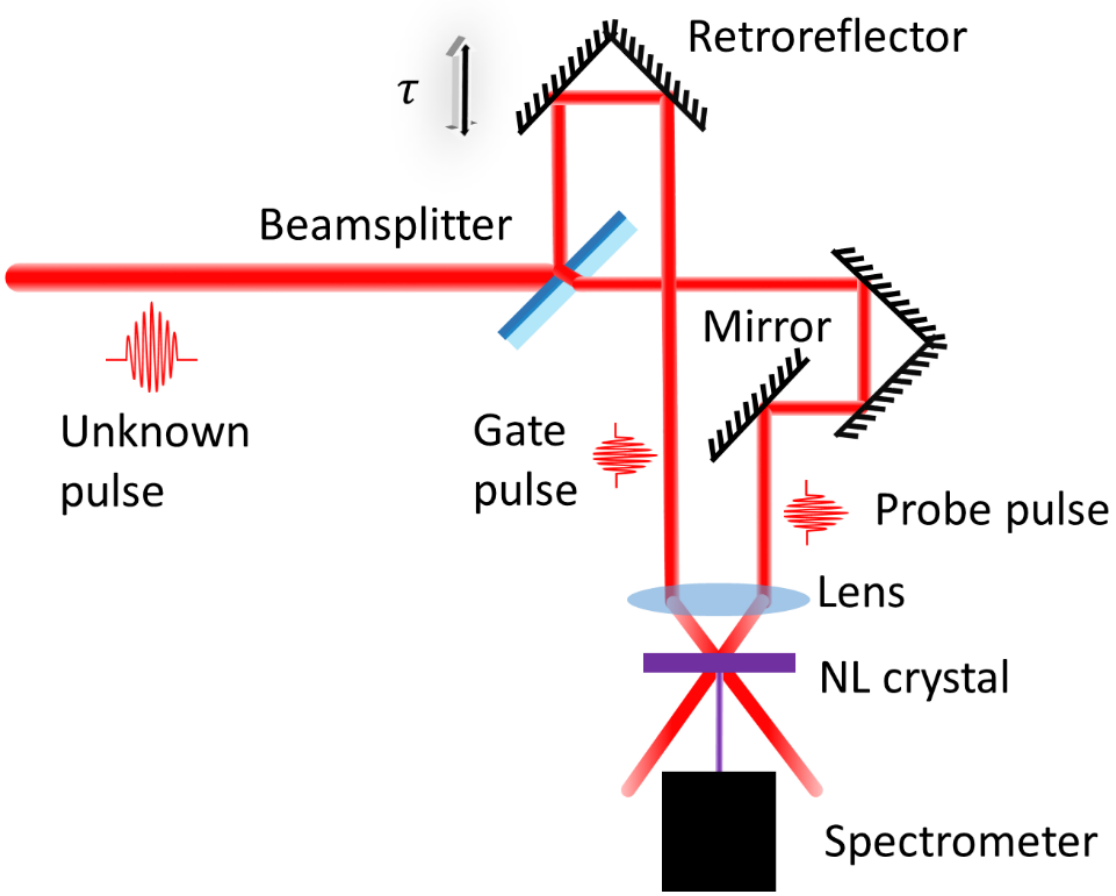

Figure 8 Schematic drawing for the frequency-resolved optical gating (FROG).

Spectral Phase Interferometry for Direct Electric-Field Reconstruction (SPIDER)

The spectral phase interferometry for direct electric-field reconstruction (SPIDER) was developed in 1998[63]. Unlike FROG, SPIDER measures the pulse amplitude and phase in a non-iterative way. The main idea can be summarized as spectral shearing interferometry. As shown in Figure 9, one replica of the unknown pulse is stretched and chirped, and another beam contains two identical replicas of the original pulse with one pulse delayed by τ compared to the other one. Sum-frequency mixing between the two beams in the nonlinear crystal results in two upconverted pulses, and their interference is spectrally resolved by a spectrometer. This process is equivalent to say that the two sum-frequency pulses are spectrally shifted by an amount $\Delta\omega$, and the intensity of the interference pattern can be expressed as

$$\begin{aligned} I_{SPIDER}(\omega,\tau) &= \left|E(\omega) + E(\omega-\Delta\omega)e^{i\omega\tau}\right|^2 \\ &= I(\omega) + I(\omega-\Delta\omega) + 2|E(\omega)||E(\omega-\Delta\omega)|\cos(\Delta\phi) \end{aligned} \tag{1.16}$$

where

$$\Delta\phi = \phi(\omega) - \phi(\omega-\Delta\omega) - \omega\tau \tag{1.17}$$

The spectral phase $\phi(\omega)$ and amplitude $E(\omega)$ of the unknown upconverted pulse can then be unambiguously calculated from the SPIDER signal.[63] If the time delay τ is sufficiently large (much larger than the original pulse duration) and the original pulse is transform-limited, then the interference pattern should follow a cosine profile with a period of $2\pi/\tau$ in the frequency-domain. Any dispersion will lead to a deviation from this period.

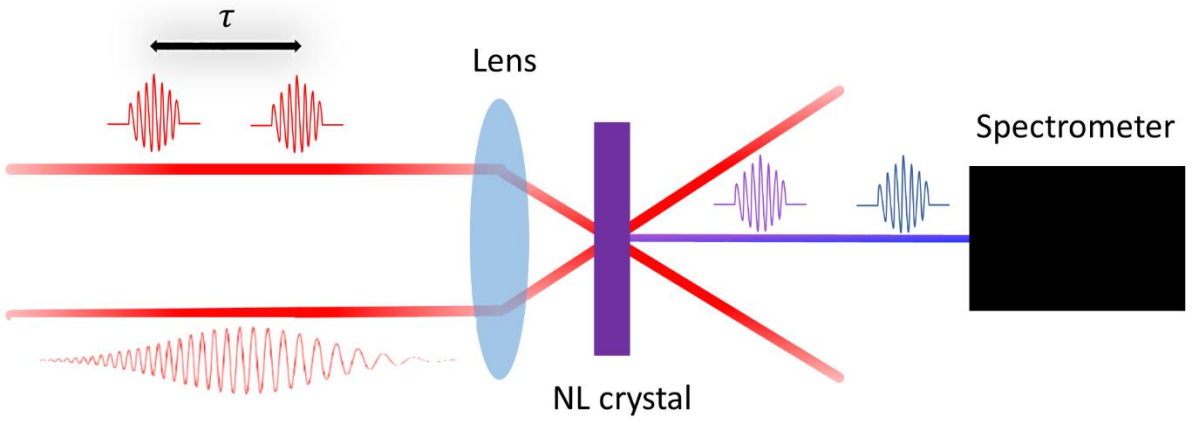

Figure 9 Schematic drawing for spectral phase interferometry for direct electric field reconstruction (SPIDER).

Multiphoton Intrapulse Interference Phase Scan (MIIPS)

Another recently developed technique using a series of well-defined reference phases to measure and even manipulate the ultrafast pulse is called multiphoton intrapulse interference phase scan (MIIPS).[64] In contrast to the previous ones, this is a single beam method that does not involve interferometry. Since its first introduction, MIIPS has demonstrated prominent accuracy and versatility, being quite fruitful in fields like selective microscopic chemical probing,[65] multiphoton microscopy[66] and functional imaging.[67]

A simplified schematic drawing of a basic MIIPS setup is shown in Figure 10a, where the spectral phase of the ultrafast pulse is controlled by a pulse shaper and the resulting second harmonic generation (SHG) spectrum is monitored by a spectrometer as a feedback signal to compress the distorted pulse. To explain the detailed working principle of MIIPS, a closer look at the spectral phase effect on SHG is helpful.

As shown in Figure 10b, the SHG signal at a frequency of 2ω can come from two photons at ω in the fundamental pulse, or one photon with a frequency of ω-ξ and one photon at ω+ξ. So the total intensity of SHG can be expressed as

$$S^{(2)}(2\omega) \propto \left| \int E(\omega+\xi) e^{i\varphi(\omega+\xi)} E(\omega-\xi) e^{i\varphi(\omega-\xi)} d\xi \right|^2 \tag{1.18}$$

For a transform-limited pulse, different frequencies in the pulse share the same phase

$$\varphi(\omega+\xi) + \varphi(\omega-\xi) \equiv constant \tag{1.19}$$

resulting in a maximized SHG intensity as oscillating terms in the integral is minimized in this case. The Taylor expansion of Eq. 1.19 gives

$$\varphi(\omega+\xi) + \varphi(\omega-\xi) = 2\varphi(\omega) + \varphi''(\omega)\xi^2 + \cdots \tag{1.20}$$

which means a transform-limited pulse, or equivalently, a maximized SHG spectrum, requires the second-order phase distortion $\varphi''(\omega)$ to vanish.

In order to measure the spectral phase $\varphi(\omega)$ of an unknown pulse, MIIPS introduces a well-known reference spectral phase function $-f(\omega,\delta)$, where δ is the parameter that can be controlled. The total phase $\phi(\omega)$ now reads

$$\phi(\omega) = \varphi(\omega) - f(\omega,\delta) \tag{1.21}$$

An SHG spectrum is measured at each δ, leading to a two-dimensional intensity map as a function of both ω and δ. As discussed above, the maximal SHG appears at $\phi''(\omega) = 0$, which means

$$\phi''(\omega) = \varphi''(\omega) - f''(\omega,\delta) = 0 \tag{1.22}$$

And since $f(\omega,\delta)$ is a known, the unknown $\varphi(\omega)$ can now be easily retrieved by taking a double integral of the $f''(\omega,\delta)$ value along the maximal MIIPS trace with respect to frequency. This retrieved $\varphi(\omega)$ value is then compensated by the pulse shaper before starting another δ scan to measure any remaining phase distortion. After several iterations, the distorted pulse

should be compressed back to its transform-limited width. The spectral phase of the unknown pulse thus comes from the accumulated $\varphi(\omega)$ from all the iterations before reaching the transform-limited pulse, and the amplitude can simply be derived from the SHG spectrum.

In principle, $f(\omega, \delta)$ can take any arbitrary function. In practice, the most commonly used form is a sinusoidal function

$$f(\omega, \delta) = \alpha \, sin(\gamma\omega - \delta) \tag{1.23}$$

which leads to

$$f''(\omega, \delta) = -\alpha\gamma^2 \, sin(\gamma\omega - \delta) \tag{1.24}$$

α is a fixed parameter (e.g. 1.5π) and γ is the expected transform-limited pulse width, in units of fs. In this case, when the pulse is fully compensated, its remaining second-order phase distortion should vanish, leading to

$$\phi''(\omega) = f''(\omega, \delta) = -\alpha\gamma^2 \, sin(\gamma\omega - \delta) = 0 \tag{1.25}$$

$$\gamma\omega - \delta = n\pi \tag{1.26}$$

So the final MIIPS trace will follow parallel lines with a slope of $1/\gamma$ and separated by π.

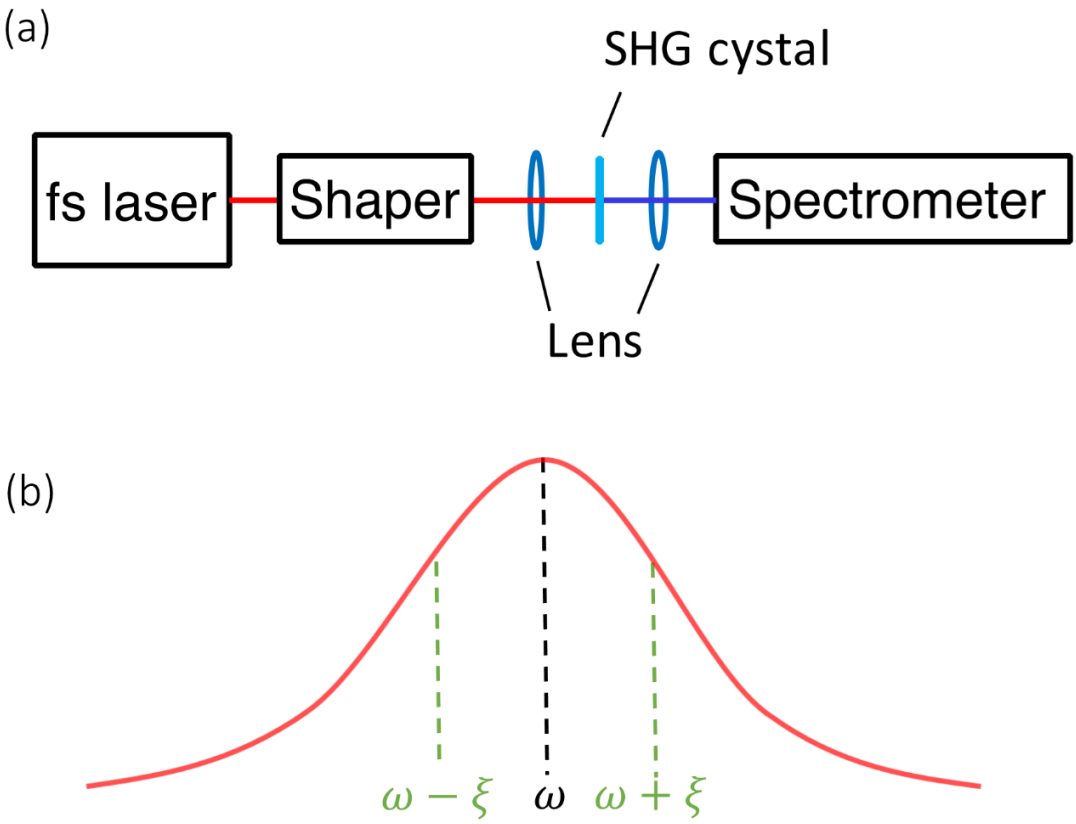

Figure 10 Multiphoton intrapulse interference phase scan (MIIPS). (a) A simplified schematic drawing for the MIIPS setup. A well-defined reference phase function is applied to the unknown pulse through a programmable pulse shaper and the resulting second harmonic spectrum is used as a feedback signal to measure and compensate for the ultrafast pulse at the same time. (b) Frequency pairs that contribute to a second harmonic generation at 2ω.

1.3.3 Pulse compensation

When a transform-limited ultrafast pulse leaves the laser cavity and travels through several optical components, such as lenses, windows, or even just air, its spectral phase gets distorted due to the frequency dependent refractive index. Such distortions largely affect the pulse duration, peak intensity, and other pulse properties, which can be detrimental for many experiments or applications. And worse, shorter pulses suffer more from the same amount of distortion than longer pulses, making pulse compensation a must especially when working with sub-10 fs pulses.

The GVD introduced by optical elements is usually positive for visible to near-infrared wavelengths, which means longer wavelengths arrive earlier than shorter wavelengths in an ultrafast pulse. To compensate for this distortion, a negative GVD needs to be introduced. Figure 11 shows a few examples that are commonly used as pulse compressors. The main idea of negative GVD relies on forcing the longer wavelengths to travel along an additional optical path, so eventually, they arrive at the same time with the shorter wavelengths. In many cases, more than one scheme is adopted. For example, negatively chirped mirrors often work with a pair of thin prisms to achieve a continuous tuning of the introduced negative dispersion.

When pulse duration reduces below 30 fs, not only the second-order dispersion but also dispersion of higher orders need to be carefully compensated. More sophisticated compensation requires an accurate measure of the pulse phase using one of the aforementioned pulse characterization techniques. Then a proper compensation scheme (or a combination of schemes) can be engineered to provide the necessary negative dispersion. The MIIPS system, on the other hand, has a built-in functionality to compress the pulse back to its transform-limited width while measuring the pulse characteristics, which can be convenient for experiments where consistent pulse duration is required.

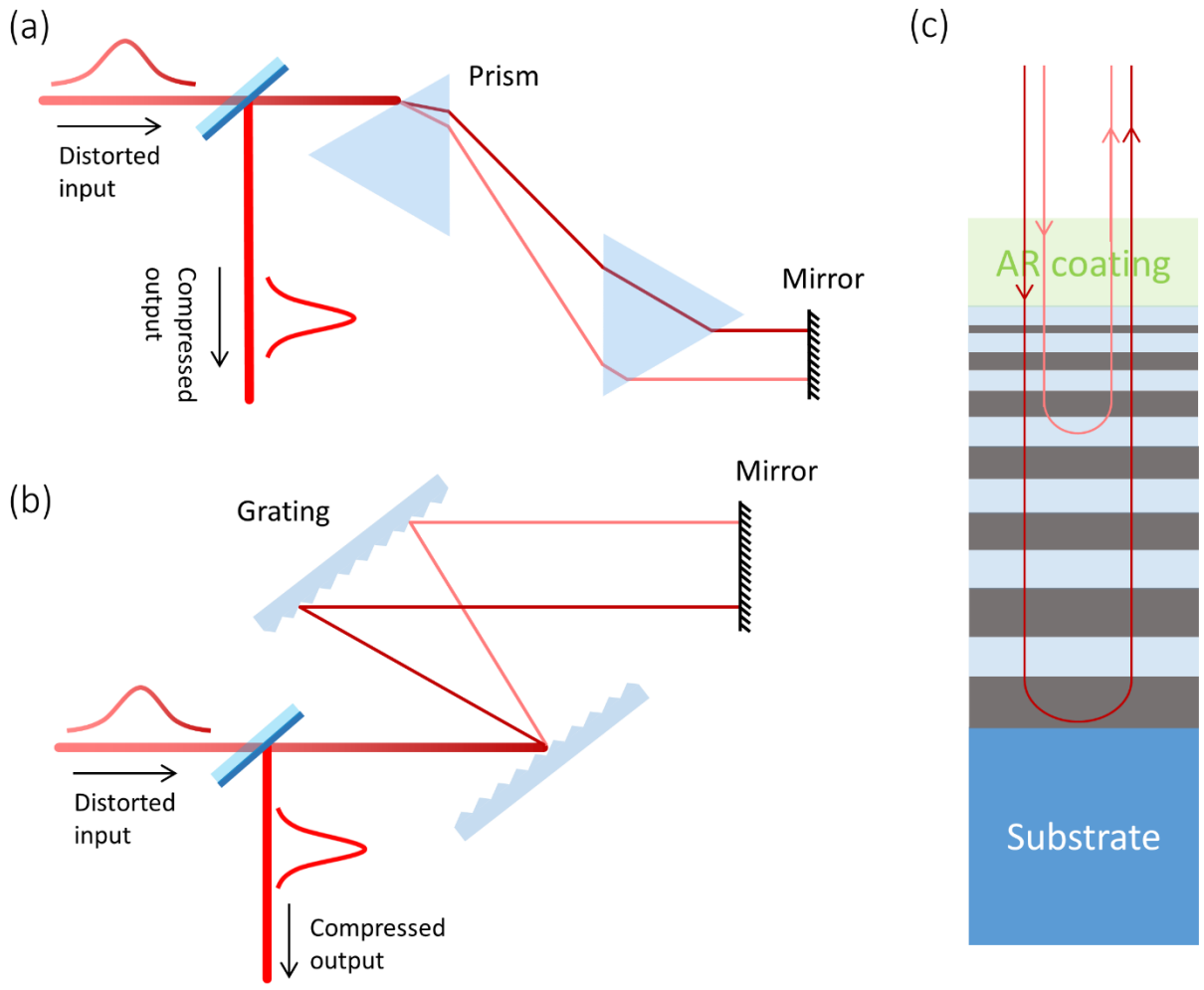

Figure 11 Pulse compression schemes. (a) The incoming distorted pulse is compressed with a pair of prism back to the transform-limited pulse by introducing an additional optical path to the longer wavelength. (b) Pulse compression with a pair of gratings. (c) The multi-layer structure for a double-chirped mirror provides a negative dispersion.

1.3.4 Pulse shaping

On top of pulse compression, ultrafast pulses can also be shaped into nearly arbitrary waveforms for user-specified applications, by controlling the amplitude, phase, and polarization of ultrafast pulses. Pulse shaping has wide-spread applications, including coherent controls for spectroscopy, optical communications, selective excitations of nonlinear optical process, and so on.[68]

There are two major approaches to pulse shaping, namely in the time-domain or in the frequency domain. Among them, Fourier transform pulse shaping is the most commonly used technique. An example of grating-based pulse shaper is shown in Figure 12. The two lenses act as the Fourier transformation elements. In this configuration, if $L > f$, then the system provides a negative phase dispersion, so it is a pulse compressor. If $L < f$, on the other hand, a positive dispersion is added to the input pulse, so now the system is a pulse stretcher. These represent simple pulse shaping schemes. More complicated waveforms can be achieved by setting $L = f$ and adding a phase mask at the focal plane, which is also known as a 4f pulse shaper.

A programmable pulse shaper can be realized by inserting an active phase mask at the 4f focal plane, for example, a spatial light modulator (SLM). More details of the working principle of SLM are discussed in the Appendix. In principle, a single-layer SLM can achieve either phase or amplitude modulation of the pulse, while a double-layer SLM has full access to both phase and amplitude degrees of freedom. Arbitrary complex waveforms thus can be controlled by programming a double-layer SLM for various applications. In Chapter 5, the spectral amplitude control of sub-7 fs pulses has been demonstrated to generate selective narrow-band THz emission at LAO/STO nanojunctions with an over 100 THz ultra-broad bandwidth tunability.

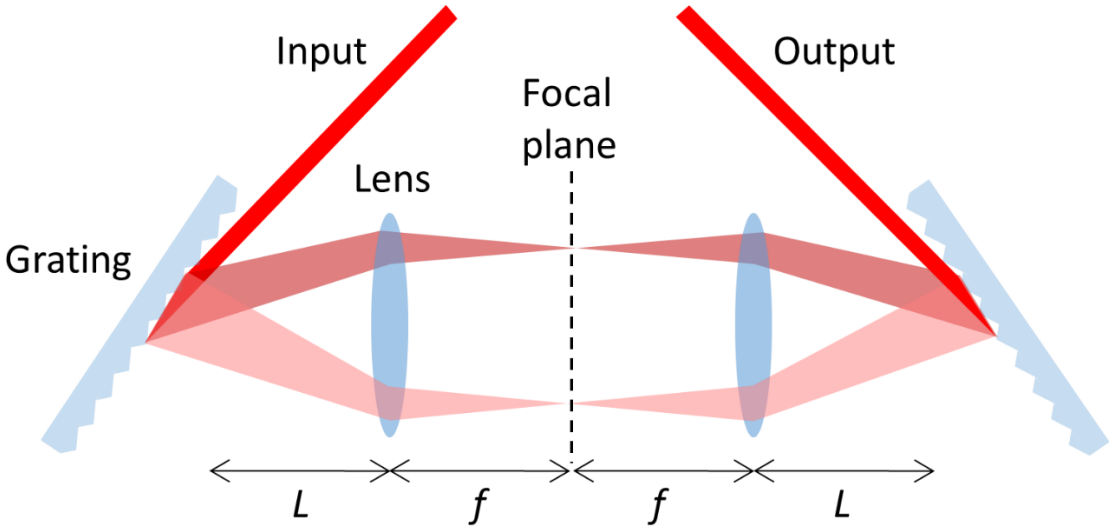

Figure 12 Grating-based Fourier transform pulse shaper.

1.4 TERAHERTZ SPECTROSCOPY OF NANOSCALE OBJECTS

Terahertz (THz) radiation is an electromagnetic wave with a frequency range occupying the gap between microwave frequencies and optical frequencies. THz radiation can penetrate thin layers of non-conducting materials, and its lower energy compared to X-rays makes THz radiation an excellent safe alternative for security scanners. THz frequencies are also known as the characteristic frequencies for intramolecular and intermolecular motions, providing unique spectral fingerprints of materials.[69] Despite its great potential in both fundamental research and industrial applications, the THz technology is still at its early stage and faces limitations in bandwidth, tunability, spatial resolution and so on.

1.4.1 THz sources and detectors

The advances of the THz technology largely depend on the development of THz sources and detectors. Tremendous efforts have been focused on both broadband and narrow-band THz generation and detection schemes, and a considerable amount of devices have been created.

1.4.1.1 Broadband THz

A thermal source, such as an arc lamp, can generate broadband radiation in the THz regime. But thermal sources are incoherent. Here, we focus on coherent broadband THz pulses that are usually produced by ultrafast laser pulses. There are two most commonly used approaches for generating coherent broadband THz pulses: photo-carrier acceleration and nonlinear process like optical rectification.

The first approach exploits the transition current in a high-speed photoconductor.[70] Ultrafast laser pulses with a photon energy larger than the material bandgap create electron-hole pairs that can be accelerated by a bias electric field and generate a transient photocurrent. And this time-varying photocurrent radiates electromagnetic waves in the THz regime.

The second approach relies on the inverse process of the electro-optic effect in a nonlinear material.[71] Frequency components in the ultrafast laser pulses mix through optical rectification, and the difference frequencies are generated in the THz regime. Such a process depends on the material's nonlinear coefficient. Compared to the photo-carrier approach, optical rectification usually provides lower output power, but much higher bandwidth, though the bandwidth is often limited by the phase-matching condition in the material. It has been reported that an ultra-broadband (0.1-100 THz) THz radiation can be generated from a thin GaSe crystal through the optical rectification.[72]

Other coherent broadband THz generation schemes include but not limited to free-electron lasers,[73] plasmon oscillations,[74] and microwave-drove nonlinear transmission lines.[75]

Similarly, the detection of broadband THz waves can be achieved using thermal detectors, or through the photoconductive sampling or the electro-optic process as well.

1.4.1.2 Narrow-band THz

The narrow-band THz radiation provides a higher resolution for spectral applications as well as insights into the fundamental light-matter interaction by selective excitations of specific resonances. Various methods have been developed for the narrow-band THz generation, such as the upconversion of microwave frequencies,[76] the downconversion of optical frequencies,[77] and gas lasers.[78] Among them, the optical method delivers a tunable coherent narrow-band THz radiation through photo-mixing between two frequency-offset lasers or different frequency components from a single multimode laser.

A continuously tunable narrow-band coherent THz source with a large bandwidth is essential for numerous applications. As mentioned above, another big limitation for THz frequencies is the spatial resolution. Due to the long wavelength of THz fields, diffraction usually limits the spatial resolution to around 10~100 μm, making it difficult to resolve features much below this scale. In Chapter 5, a selective difference frequency generation technique at LAO/STO nanojunctions is discussed with over 100 THz bandwidth through femtosecond optical pulse shaping, which provides an exceptional spatial precision of 10 nm.

1.4.2 Broadband THz generation and detection at 10 nm scale

In 2013, Ma *et al.* reported a broadband THz generation and detection technique at 10 nm scale (Figure 13).[79] This new class of THz sources and detectors is realized using LAO/STO nanojunctions. The experimental implementation is shown in Figure 13a. Two nanojunctions, labeled A and B, are created at the LAO/STO interface using c-AFM lithography. The separation is around 12 μm, which is confirmed by the photovoltage scan and the reflection scan that are taken simultaneously (Figure 13b and c).

To acquire the reflection and the photovoltage scan, one input laser beam is modulated by a chopper and raster scanned across the sample surface using a piezoelectric stage. A constant bias voltage is applied on the source (S) electrode, while the drain (D) electrode is grounded. The photo-induced voltage change ΔV across the two voltage sensing electrodes V_+ and V_- ($\Delta V = V_+ - V_-$) is measured at the same time as the reflection. Then the reflection and the ΔV are demodulated by a lock-in amplifier and plotted on a *xy* intensity map, respectively. The reflectance contrast between patterned gold electrodes and the oxide surface in the reflection image shows the sample position, while the simultaneously acquired photovoltage scan identifies the nanojunction.

The nanojunction photoresponse in the visible to near-infrared regime may seem bizarre, as both LAO and STO have large bandgaps. This can be explained, however, by mid-gap states existed in the STO substrate[80] that could originate from oxygen vacancies or unintentional dopings of STO. Electrons in mid-gap states can be excited into the conduction band with sub-bandgap lights and the photoexcited electrons will then be driven across the nanojunction by the bias field, leading to a photo-induced voltage change ΔV.[81]

Ultrafast pulses coming from a Ti: Sapphire oscillator are split into two beams. One beam is modulated at frequency f_A and focused on the nanojunction A, while the other beam is delayed

by time τ, modulated at frequency f_B focused on the nanojunction B. The photo-induced voltage change ΔV across the nanojunction is monitored as a function of time delay τ for both devices in a way that for device A, the signal ΔV_A is demodulated at a frequency f_B through a lock-in amplifier, while for device B, the signal ΔV_B is demodulated at a frequency f_A through another lock-in amplifier. In this configuration, the signal generated at one nanojunction is actually detected by the other nanojunction. The amplitudes for both ΔV_A and ΔV_B are plotted in Figure 13d with respect to τ. Each curve is an average of 100 measurements. A time delay around 44 fs is observed between the two signals. Figure 13e shows the corresponding fast Fourier transform spectra, both exhibiting a broad spectrum extending to 10 THz.

The generation and detection mechanism has been attributed to the third-order nonlinear response in STO. As mentioned in Chapter 1, compared to many other materials, STO has unusually large third-order nonlinear optical susceptibility $\chi^{(3)}$. Frequency components in the ultrafast pulses mix at the nanojunction through a DC bias field mediated third-order nonlinear process, and generate emission at THz frequencies. The generated THz field from one nanojunction propagates to the other nanojunction, where its near field components are detected. The observed 44 fs time delay in Figure 13d corresponds to the THz field travelling 12 μm in vacuum.[79]

Through the third-order nonlinear effect, ultrafast pulses provide temporal confinement to the THz emission, resulting in a broadband nature, while the LAO/STO interface nanojunction offers spatial confinement, leading to a nanoscale precision around 10 nm. Such nanoscale control of the THz emission, with a spatial resolution four orders of magnitude smaller than the diffraction limit, opens up new possibilities for probing a single nanoscale object at THz frequencies.

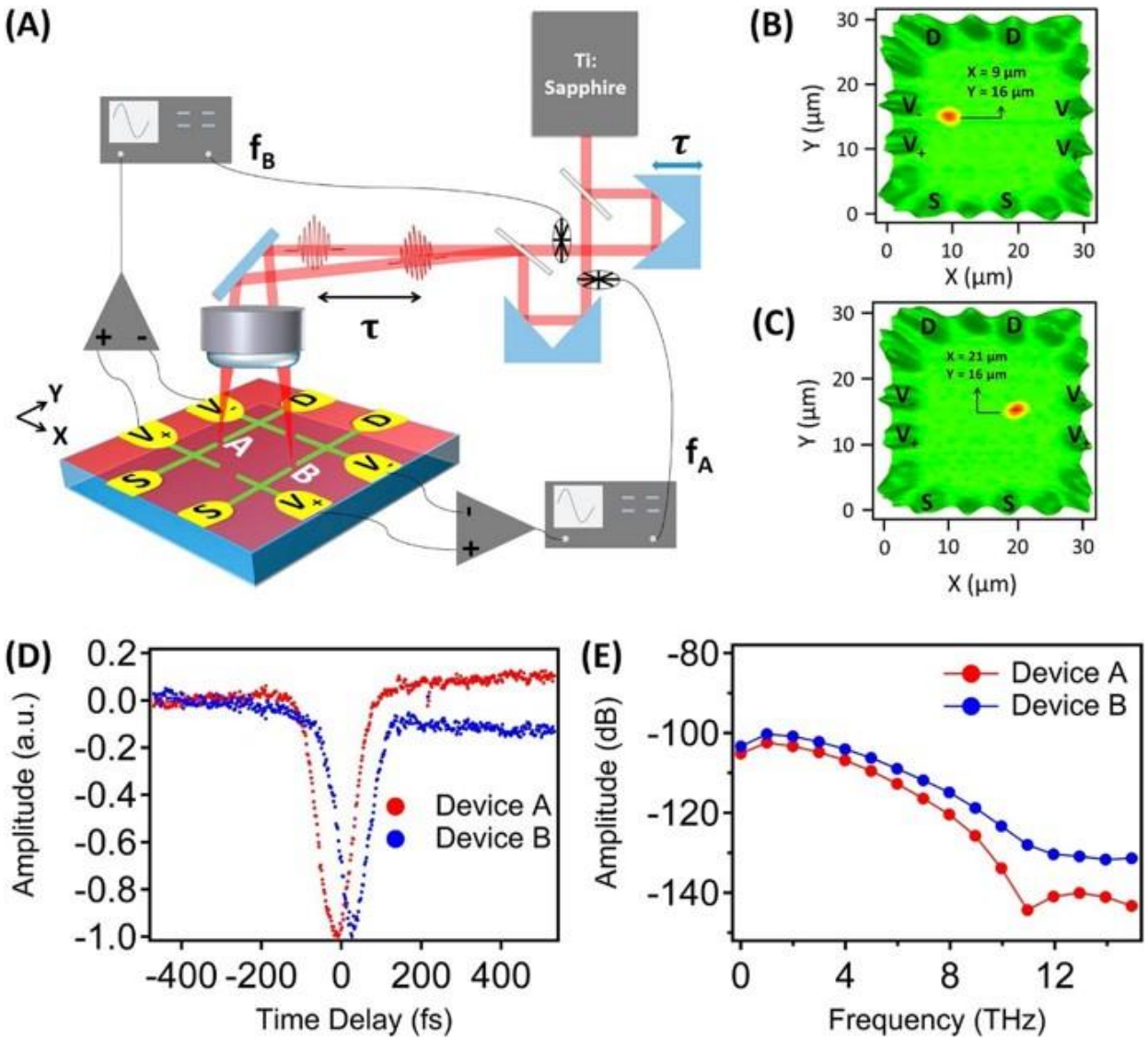

Figure 13 Broadband terahertz generation and detection at 10 nm scale at LAO/STO nanojunctions. (a) Schematic drawing of the experimental setup for the double-junction measurement. (b) and (c) are photovoltage images overlapped with the reflection scans that are taken simultaneously, showing the position of each nanojunction. (d) Time-resolved photovoltage changes across the two nanojunctions. A time delay around 44 fs is observed between the two signals. (e) The corresponding fast Fourier transform spectra of (d). Ref. [79]

2.0 EXPERIMENTAL METHODS

This chapter describes the main experimental methods employed in the following work, including the c-AFM lithography for creating nanostructures at the complex oxide interfaces, the optical cryostat or dilution refrigerator and the electronic connections for low temperature measurements, the compact Michelson interferometer for probing the ultrafast optical responses, and the pulse shaper that is critical for ultrafast pulse compression and pulse shaping.

2.1 C-AFM LITHOGRAPHY

2.1.1 AFM working principle

The atomic force microscopy (AFM) is one of the scanning probe microscopy (SPM) techniques, with a sub-nanometer resolution. It was first invented in the early 1980s, as a by-product of the development of scanning tunneling microscope (STM), and soon became one of the most widely used tools for nanoscale imaging, characterization, and manipulation.

An AFM employs a sharp tip mounted on the free end of a cantilever. The curvature of the sharp tip is usually on the order of a few nanometers to tens of nanometers. When the cantilever approaches the sample surface, atomic forces between atoms at the very end of the tip and atoms on the sample surface bend the cantilever, which is detected to gain information about the sample.

Depending on the distance between the tip and the sample, the atomic force can be either repulsive or attractive, as shown in Figure 14. When the tip is relatively far away from the sample

surface, the attractive force causes the cantilever to bend towards the surface. By contrast, when the tip is in close proximity to the sample, the cantilever is bent away from the surface by a repulsive force. The region in between is an intermediate area. Correspondingly, the AFM can be operated in three modes, namely the non-contact mode when the tip is far away from the sample, the contact mode where the tip is pressed to form direct contact with the sample surface, and the tapping mode when the tip is operating in between. Details of the three modes will be discussed further below.

One common scheme to quantify the deformation of the cantilever involves a laser and a quadrant photodetector (Figure 15). The input laser beam reflects off the cantilever top surface onto the photodetector, and the relative position of the reflected beam with respect to the quad-segmented regions A, B, C, and D is measured by V_A, V_B, V_C, and V_D, respectively. The sum of these voltages gives the "Sum" value displayed in the software

$$Sum = V_A + V_B + V_C + V_D \tag{2.1}$$

The vertical bending of the cantilever can be quantified using "Deflection" defined as

$$Deflection = (V_A + V_B) - (V_C + V_D) \tag{2.2}$$

The lateral twisting of the cantilever is characterized using

$$Lateral = (V_A + V_C) - (V_B + V_D) \tag{2.3}$$

Compared to other nanoscale probing techniques, such as STM, SEM, and TEM, AFM can work in air or liquid, and do not require special treatments for the sample. Different variants of the AFM have also been developed for varies applications over the years, including electrostatic force microscopy (EFM), Kelvin probe force microscopy (KPM), magnetic force microscopy (MFM), piezoresponse force microscopy (PFM), just to name a few.

2.1.1.1 Contact mode

Contact mode is the first mode developed for imaging sample topography with AFM. In contact mode, the tip is brought into a firm contact with the sample, which is sitting on a xyz piezoelectric stage, as shown in Figure 15. The force between the tip and the sample can be described by Hooke's law

$$F = -k \times D \tag{2.4}$$

where k is the cantilever spring constant and D is the vertical bending distance, which can be mapped to the induced deflection change. When the tip is scanned across the sample surface, the interaction force F changes, resulting in a change in the deflection. The sample topography in contact mode can be measured directly using the deflection change, or more commonly, using a feedback loop. In the latter scenario, the deflection is kept the same as the setpoint throughout the scanning by constantly feeding the difference into a feedback loop while controlling the piezo z movement. The topography image can then be plotted spatially using the z piezo height change across the scanned area.

In ambient condition, water molecules in the environment usually form a liquid meniscus layer. Contact mode can penetrate through this layer, thus gives an accurate measure of the sample surface. But this "dragging" in water meniscus also increases the risk of damaging soft samples or getting the tip stuck to sample surface. Another possible problem with contact mode is the degrading of the tip (and/or even a rigid sample surface) after several scans. To solve these difficulties, tapping mode was introduced.

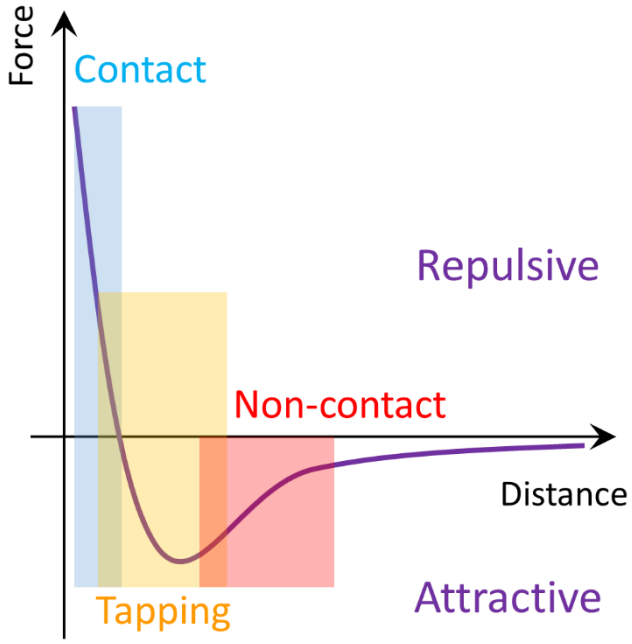

Figure 14 Atomic force microscopy (AFM) force curve.

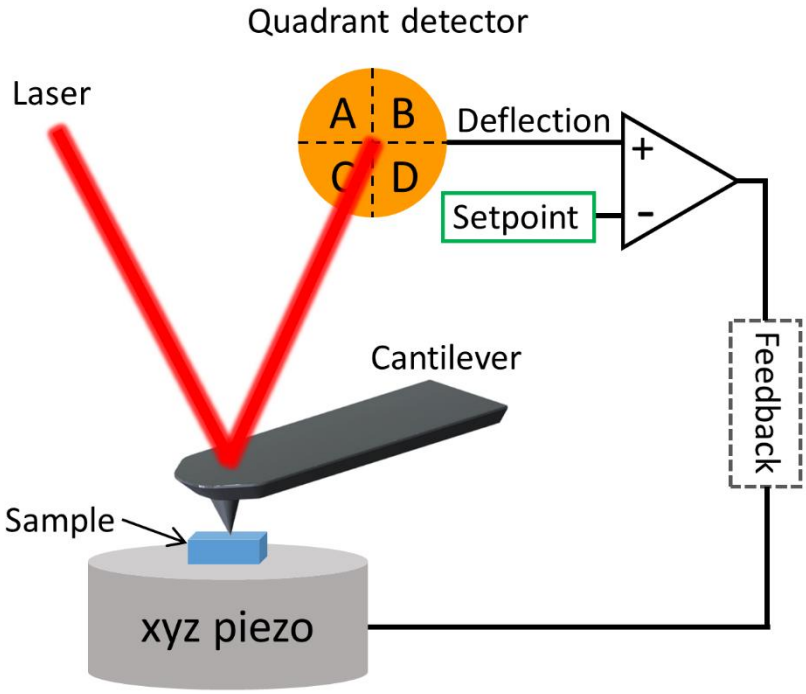

Figure 15 Schematic drawing of the AFM contact mode setup.

2.1.1.2 Tapping mode

In tapping mode, the cantilever is operated in a dynamic scheme, thus is also called dynamic contact mode or sometimes AC (alternating current) mode. A piezo shaker attached to the cantilever or a modulated thermal source (e.g. infrared laser beam) drives it to oscillate at or near its resonance frequency (Figure 16), which leads to an oscillating deflection. A lock-in amplifier demodulates the AC deflection and outputs both its amplitude and phase. When the tip is closer to the sample surface, the interaction forces changes the amplitude of the cantilever oscillation (generally becomes smaller). The difference between the amplitude and the setpoint is fed into the feedback loop to control the z-axis of the piezoelectric stage underneath the sample to maintain a constant amplitude *A*.

The oscillation amplitude in tapping mode is large, typically lies between several nanometers to 200 nm, so the tip can be close enough to measure short-range forces. The tip still strikes against the sample surface but detaches within each oscillation cycle. This mechanism largely reduces the lateral force, together with the small contact duration, making tapping mode less harmful to both the sample and the tip. Tapping mode is probably the most frequently used AFM mode, especially in ambient conditions or in liquids.

In addition to topography or equivalently, height image, tapping mode also generates a phase image. This channel contains information regarding the oscillation energy dissipation difference across the sample surface. Areas with different types of materials can be differentiated, even if they exhibit the same height.

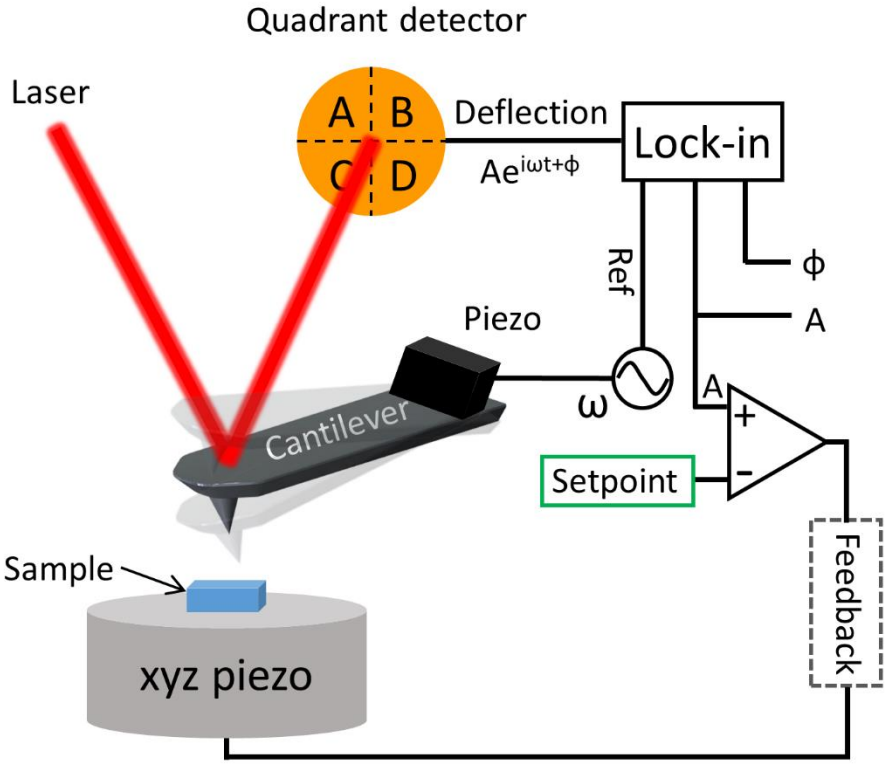

Figure 16 Schematic drawing for the AFM tapping and non-contact mode setup.

2.1.1.3 Non-contact mode

Just as its name implies, in non-contact mode, the AFM tip does not contact the sample surface. The cantilever also oscillates at or close to its resonance frequency, but with much smaller amplitude (generally within a few nanometers) compared to tapping mode. Only long-range forces are measured in this case. Either amplitude modulation or frequency modulation can be used to form a feedback loop in non-contact mode.

The non-contact mode is the gentlest mode among the three. No degradation is expected for tip nor sample even after repeated scans. However, the trade-off is the image validity in the presence of water meniscus, as the tip cannot penetrate through the meniscus layer.

2.1.2 c-AFM lithography

In 2008, Cen *et al.* reported the ability to create and erase nanoscale conducting regions at the interface of LAO/STO using the c-AFM lithography technique.[43] This was done on a sample with 3.4 unit cells of LAO layer, which is just below the critical thickness. The interface is thus insulating but highly electric field tunable. As shown in Figure 17a and b, when scanning a positively biased AFM tip in contact mode from one electrode to the other, a conducting nanowire at the LAO/STO interface can be created, which is confirmed by the two-terminal conductance jump once the tip reaches the second electrode. And this process is reversible: a negatively biased AFM tip scanned across the existing nanowire can locally restore the interface back to an insulating state, and a conductance drop is observed as the tip erases the nanowire (Figure 17c and d).[43] The width of the nanowire can be estimated by fitting to the conductance drop. It has been shown that the nanowire width at the LAO/STO interface depends sensitively on the writing voltage. At +3 V, a wire width of 2~3 nm can be reached. But as the writing voltage increases, the nanowire width increases monotonically.[43, 82] With the most commonly used writing voltages (+10~15 V), the wire width is typically around 10 nm.[18, 79, 83, 84]

This reconfigurable and versatile technique has made LAO/STO a quite fruitful platform for both studying correlated electron interactions as well has realizing devices with various functionalities. A large number of nanostructures, such as field-effect transistors,[82] electric rectifiers,[85] sketched single-electron transistors,[83] ballistic electron waveguides,[18] photodetectors,[81] and broadband THz sources and detectors,[79] have been created and characterized.

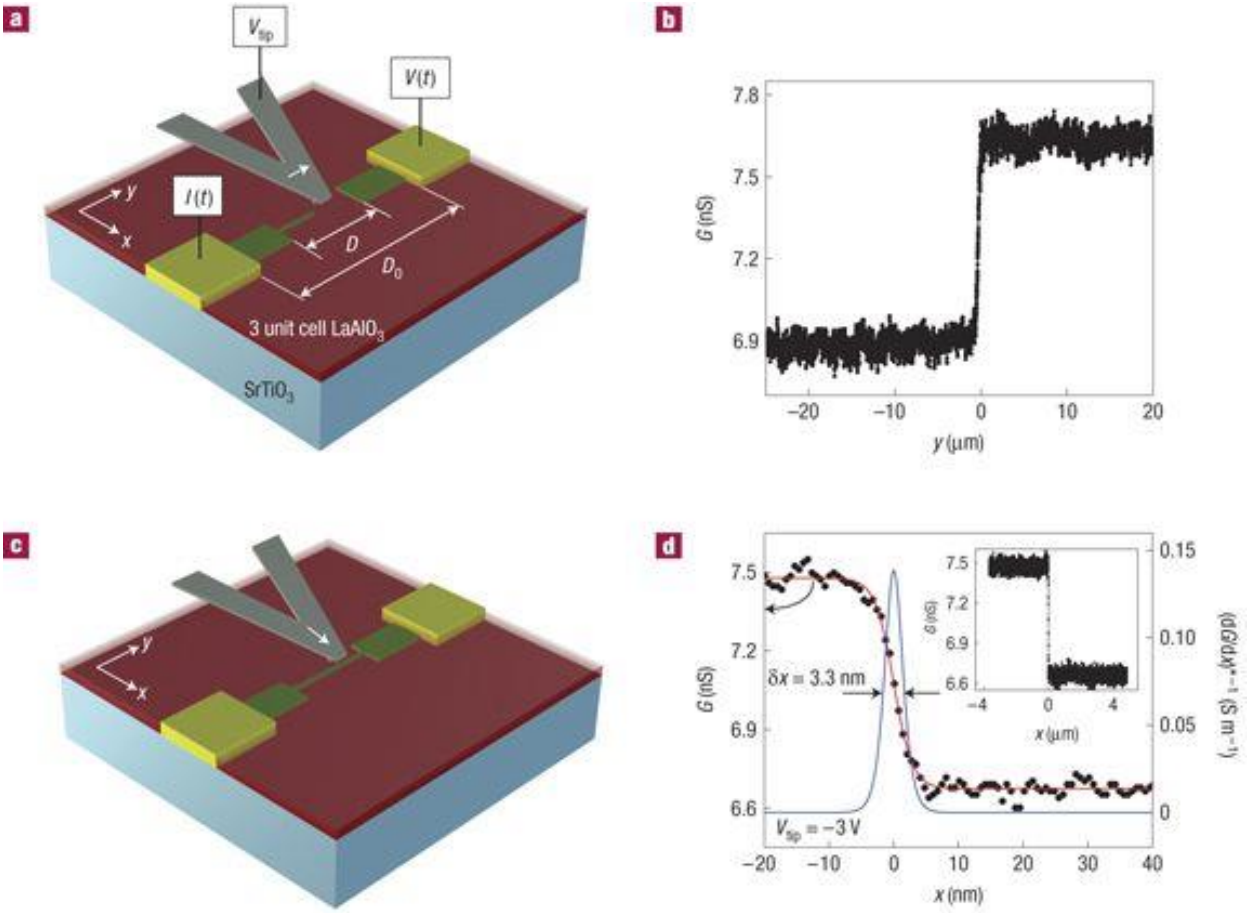

Figure 17 c-AFM lithography. (a) Schematic drawing of creating a conducting nanowire at the LAO/STO interface by scanning a positively biased AFM tip between two electrodes. (b) The conductance between the two electrodes is monitored during writing and a conductance jump is observed once the tip reaches the second electrode. (c) Schematic drawing of erasing an existing nanowire at the LAO/STO interface by cutting with a negatively biased AFM tip. (d) A conductance drop is observed, from which the nanowire width can be extracted. Ref. [43]

2.1.3 Surface protonation and de-protonation

The mechanism for the writing/erasing process is believed to involve the surface protonation/de-protonation.[34, 86] Water molecules in the atmosphere are absorbed on the LAO surface and dissociate into H^+ and OH^- ions. The positively biased AFM tip removes a portion of the OH^- ions along its path, thus locally charging the surface with the excessive H^+. Similar to the modulation doping, the protonated surface will locally switch the LAO/STO interface from insulating to conducting. In the reverse process, the negatively biased AFM tip removes the extra H^+, restoring the interface to an insulating state. The surface protonation/de-protonation process allows multiple writing and erasing cycles without degrading the oxide heterostructure.

The c-AFM lithography creates nanoscale conducting regions in a gentle and non-destructive way, leading to a much smoother confinement profile for the electrostatically confined nanowire. Also, the embedded conducting regions at the interface are not directly in contact with surface defects, edges or surface adsorbates, unlike nanostructures defined by the conventional lithography.

2.2 LOW-TEMPERATURE MEASUREMENT

2.2.1 Optical cryostat

Ultrafast optical responses are measured at cryogenic temperatures using a Montana Instruments optical cryostat. It is a closed-cycle operation system, with a temperature range from 4 to 350 K. The temperature stability is less than 10 mK and vibration stability is below 5 nm. It is also

equipped with radiation-blocked optical windows and electronic connections, providing both optical and electronic access to the sample.

The cryostat has four main components: a compressor, a control unit, the cryostat with a sample chamber, and a computer user interface. A schematic block diagram of the system is shown in Figure 18. The cooling is mainly provided by a two-stage cryo-cooler, which is part of the closed-loop helium flow circle. Thermometers and heaters are attached to both stages to accurately measure and control the stage temperature. A thermal radiation shield surrounding the sample is thermally coupled to the first stage, and the sample is mounted to a post that is thermally coupled to the second stage. A vacuum is created in the chamber to thermally isolate the sample, radiation shield, and outer shell. A PID feedback loop is used to control the helium flow and the heater power to maintain a set temperature.

The sample is placed on a chip carrier that is attached to the PCB board (Figure 19a). The sample mount can be positioned either pointing up or sideways. Light can enter the sample chamber through any one of the windows, and the reflection or transmission after sample can be collected from the same or a different window, depending on the experimental scheme and sample mount orientation. Electronic properties of the sample can be measured through the 28 electrical feed-throughs, as shown in Figure 19b. In our system, the yellow spring wires are replaced by a ribbon cable that is connected to a Fisher connector to establish the electrical connection to instruments outside the sample chamber.

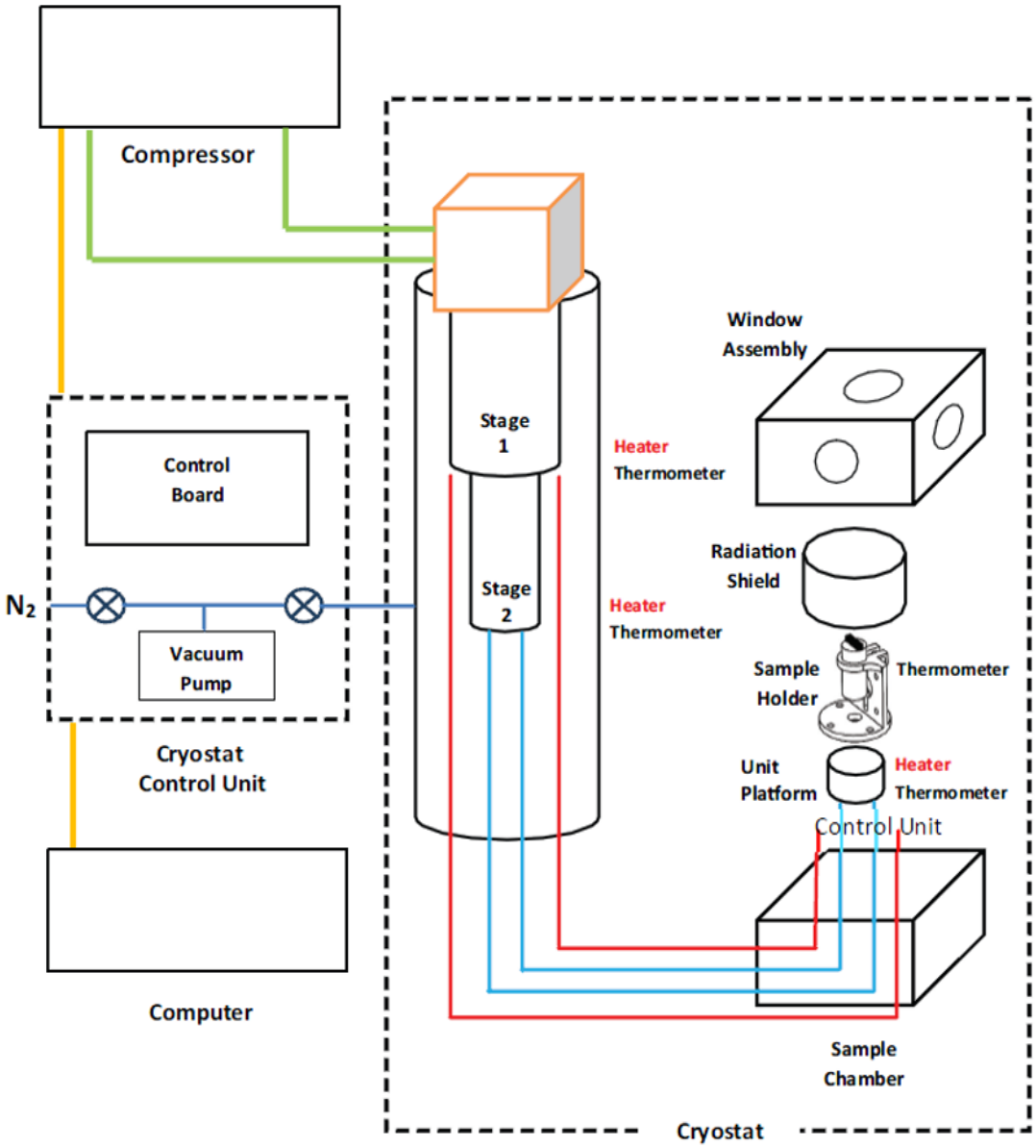

Figure 18 Montana Instruments optical cryostat block diagram. Image adopted from the Montana Instruments cryostat user manual.

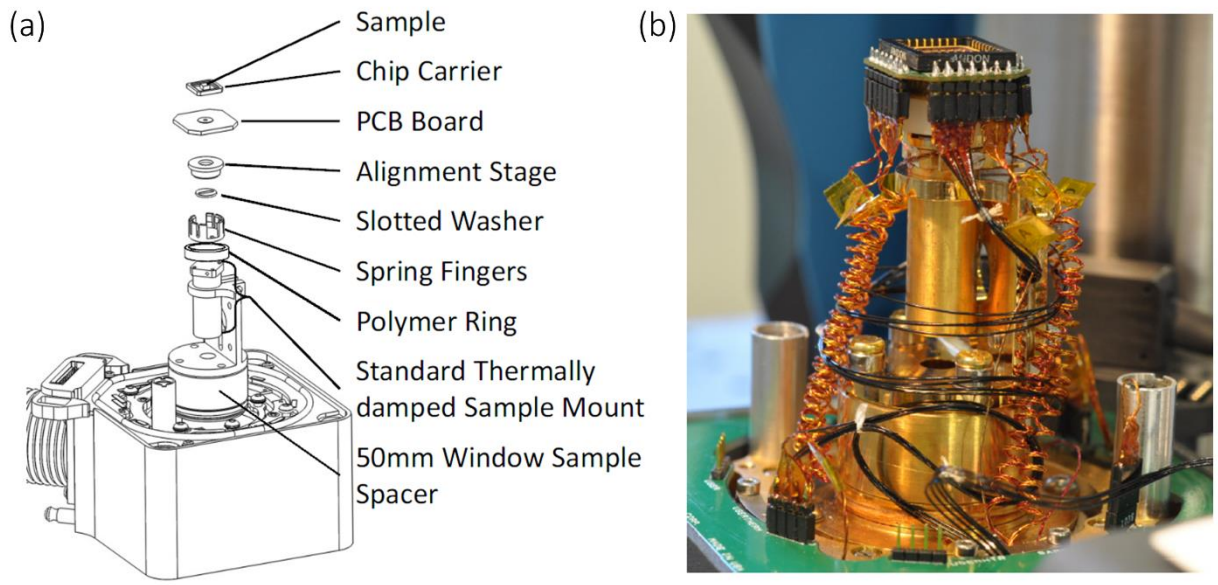

Figure 19 Montana Instruments optical cryostat sample holder. (a) Internal components of the sample holder. (b) Picture of the sample holder and electronic connections. Images adopted from the Montana Instruments cryostat user manual.

2.2.2 Dilution refrigerator

Transport properties are measured at millikelvin temperatures using a Quantum Design Physical Property Measurement System (PPMS) that can reach a base temperature of 50 mK and a magnetic field of ±9 T.

At atmospheric pressure, the boiling temperature of helium is around 4 K. Pumping can further reduce its temperature to 1.8 K. The millikelvin base temperature is achieved through a Quantum Design dilution refrigerator (DR) insert. The working principle for a DR can be explained by Figure 20. A phase diagram of ^{3}H and ^{4}H is shown in Figure 20a, where X is defined as the percentage of ^{3}H in the ^{3}H and ^{4}H mixture. As the temperature decreases, the ^{3}H and ^{4}H mixture (33% ^{3}H and 66% ^{4}H) approaches from the normal stage to the forbidden state, and part

of the mixture turns into a concentrated ^{3}H phase, while others reach a ^{4}H + 6% ^{3}H dilute phase. As the ^{3}H has a lower boiling point (because it is lighter), when the turbo-pump pumps on the "still" (Figure 20b), the ^{3}H vapor is pulled away mostly (~90%), reducing the ^{3}H concentration in the dilute layer. So more ^{3}H from the concentrated layer will come into the dilute layer, and this process absorbs heat.

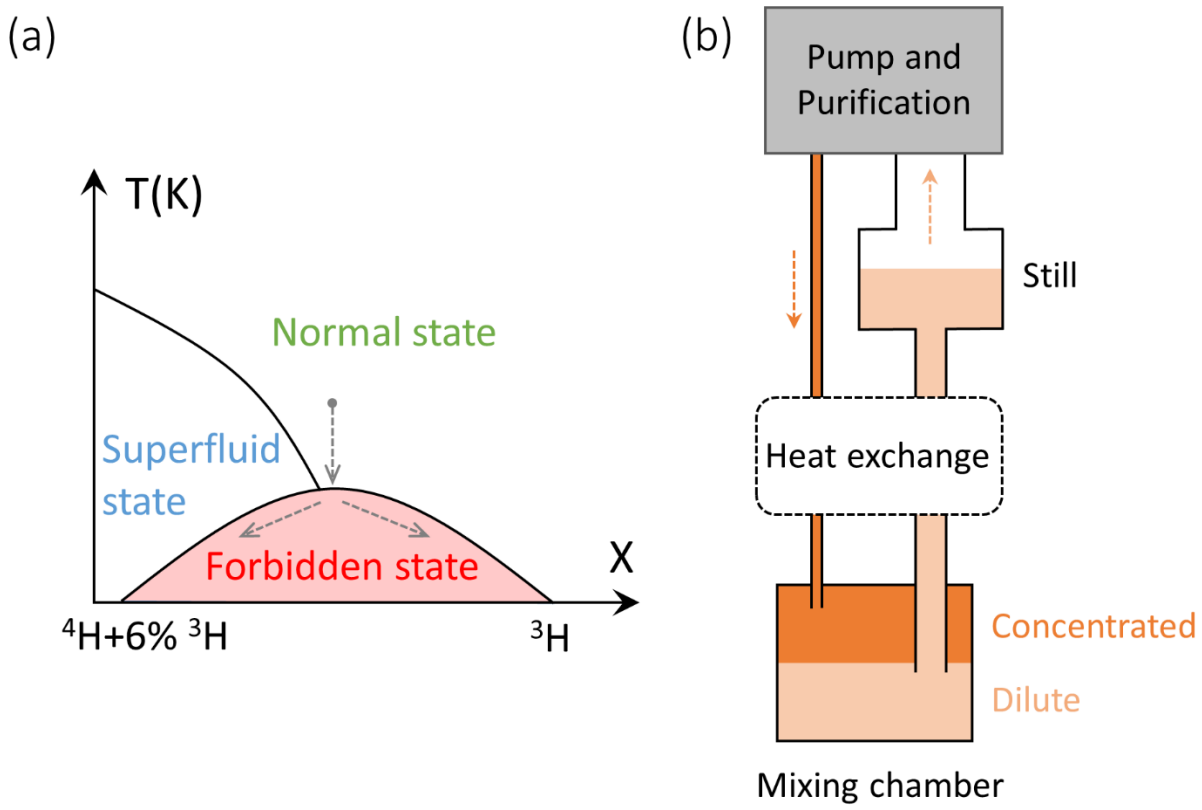

Figure 20 Dilution refrigerator working principle. (a) Phase diagram of ^{3}H and ^{4}H. (b) Simplified functional diagram of the dilute refrigerator.

2.3 COMPACT MICHELSON INTERFEROMETER

The core component of the optical setup for studying ultrafast optical responses based on LAO/STO nanojunctions is a compact Michelson interferometer. A three-dimensional CAD drawing of the interferometer design is shown in Figure 21. Input laser pulses are directed into the compact interferometer by a plane mirror. There are two small irises for cross-checking the alignment. Then the pulses are divided by a 50/50 ultrafast beam splitter into two arms. The upper arm contains a compensation plate to fine tune the dispersion difference between the two arms. A piezoelectric state is also placed in the upper arm as an optical delay line. Its total closed-loop travel range is around 500 μm, corresponding to about 3.3 ps round-trip time delay. The right arm is sitting on a mechanical stage, which serves as a coarse adjustment of the relative time delay between the two arms. Each arm has a polarizer, so the light polarization can be varied independently before reflected back by a reflective chopper (Boston Micromachines Corporation). The reflected beams are then combined by the same 50/50 beam splitter and focused onto the sample through an objective. A second ultrafast beam splitter is designed for measuring the reflectance as well as monitoring ultrafast pulses. The objective is mounted on another three-axis piezoelectric stage that can scan in the *xy* plane and fine-tune the focus with the *z*-axis. A high-quality reflection image can be taken using this configuration. Again, the three-axis piezoelectric stage is mounted on a three-axis mechanical stage for coarse position adjustments.

There are three major merits with this interferometer design. First, the ultra-compact design gives precise control over beam positions. Its close proximity to the sample chamber guarantees a minimized optical path that light needs to travel before reaching the sample. By varying the angle of the mirror mount in each arm, each beam can be positioned independently to any location within the 30 μm × 30 μm canvas on the sample precisely. Experiments involve two nanojunctions can

thus be easily configured. Second, the piezoelectric stage in the upper arm provides very high resolution and repeatability for the optical delay. Last but not least, the conventional mechanical chopper is abandoned, instead, a reflective chopper is adopted for each arm. Basically, a reflective chopper can be viewed as a reflective diffraction grating that consists of a mirror membrane supported by an underlying actuator array. Light modulations are achieved by switching between an unpowered flat mirror-state and a powered diffractive state. Since essentially there are no moving parts in the reflective chopper, the vibrational noise is negligible. In addition, the modulation frequency can be as high as 200 kHz, and the two beams can either be modulated with the same frequency or different frequencies.

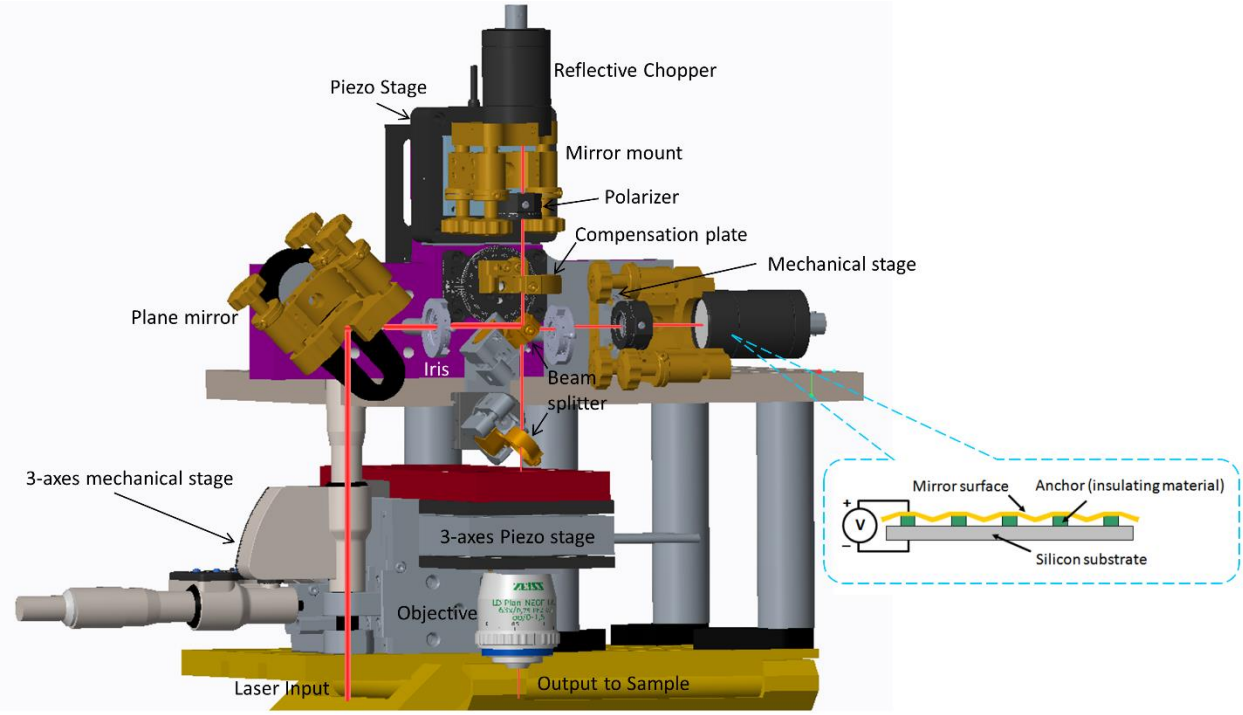

Figure 21 3D drawing for the compact Michelson interferometer design. Inside the blue dashed callout is a schematic drawing for the reflective chopper (image adopted from the Boston Micromachines Corporation website).

2.4 PULSE SHAPER

A picture of the actual home-built pulse shaper is shown in Figure 22. Main components include a grating, a concave mirror, and a programmable spatial light modulator. The basic idea is similar to the 4*f* Fourier transform pulse shaper introduced in Chapter 1, except a reflection configuration is adopted here to save space and a concave mirror acts as the Fourier transform element instead of a lens.

Input pulses go through an input iris and get redirected by a plane mirror followed by a plane square mirror. Square mirrors are selected in this design to give the best clearance for beams at different heights. Then the beam incidents onto a ruled reflection grating with 600 g/mm and 13° blaze angle. Different wavelengths are diffracted with different first order diffraction angles. The spread beam is then collected by a square mirror and focused onto the liquid crystal layers in the SLM by a concave mirror (focal length 200 mm). The SLM is set up in a reflection mode, and the reflected (and manipulated) beam travels back following almost the same path to the grating where different wavelengths are recombined spatially. To separate the input and the output beam, a small tilting in the z-direction (beam height slowly increases as it travels) is adjusted on purpose. The output beam goes through an iris and gets redirected by three plane mirrors before leaving the pulse shaper through the output iris.

One important detail that needs to be mentioned is that, due to the intentional tilting in the z-direction, the beam experiences a conical diffraction from the grating. As a result, the diffracted wavelengths lie in a cone instead of a plane. In addition, the off-axis input for the concave mirror will also add additional spherical aberrations. But compared to other ways of separating the output

beam from the input beam, like adding a beam splitter, displacing the output beam vertically provides a much higher output power.

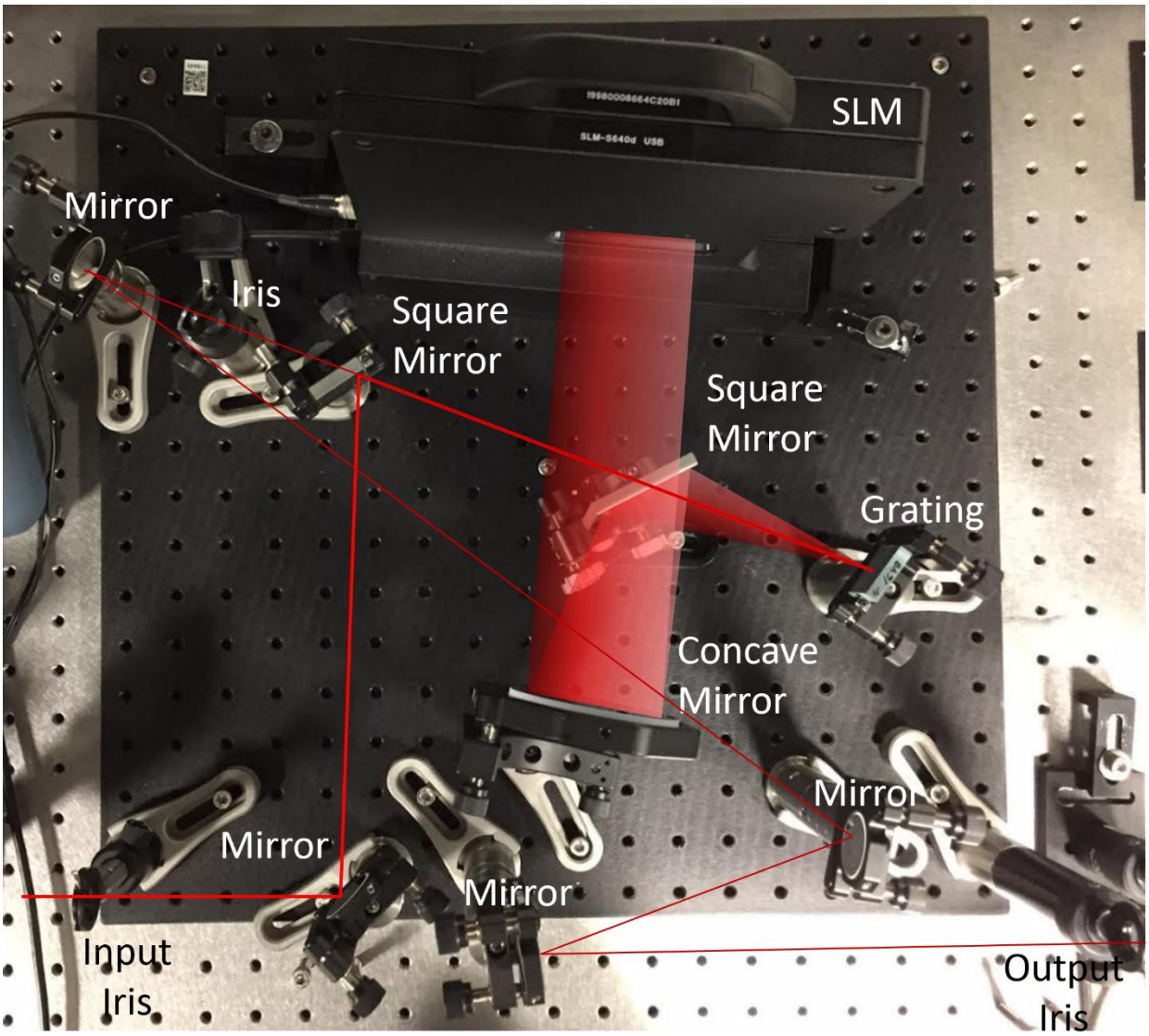

Figure 22 Picture of the home-built pulse shaper.

3.0 EXTREME RECONFIGURABLE NANOELECTRONICS AT THE CZO/STO INTERFACE

The contents of this chapter represent a collaborative work published in Chen, Li, Tang, Pai, Chen, Pryds, Irvin and Levy, *Advanced Materials* **30**, 1801794 (2018).

Complex-oxide heterostructures have fascinating emergent properties that originate from the properties of the bulk constituents as well as from dimensional confinement. The conductive behavior of polar/non-polar LAO/STO interface can be reversibly switched using c-AFM lithography, enabling a wide range of devices and physics to be explored. Here, extreme nanoscale control over the CZO/STO interface, which is formed from two materials that are both nonpolar, is achieved. Nanowires with measured widths as narrow as 1.2 nm were realized at the CZO/STO interface at room temperature by c-AFM lithography. These ultra-thin nanostructures have spatial dimensions at room temperature that are comparable to single-walled carbon nanotubes, and hold great promise for alternative oxide-based nanoelectronics, as well as offer new opportunities to investigate the electronic structure of the complex oxide interfaces. The cryogenic properties of devices constructed from quasi-one-dimensional channels, tunnel barriers, and planar gates exhibit gate-tunable superconductivity, quantum oscillations, electron pairing outside of the superconducting regime, and quasi-ballistic transport. This newly demonstrated ability to control the metal-insulator transition at nonpolar oxide interface greatly expands the class of materials whose behavior can be patterned and reconfigured at extreme nanoscale dimensions.

3.1 INTRODUCTION

Complex oxide heterostructures exhibit diverse emergent properties, including a tunable metal-insulator transition,[30]magnetism,[45] superconductivity,[87] and spin-orbit coupling.[47, 88] The ability to create and reconfigure nanoscale conducting regions at the polar/nonpolar LAO/STO interface using the c-AFM lithography technique has made LAO/STO an attractive platform for both studying the fundamental physics of correlated electronic systems and developing future oxide-based nanoelectronic devices. Various nanostructures have since been realized in the LAO/STO system, including sketched single-electron transistors,[83] ballistic electron waveguides,[84] field-effect transistors,[82] photodetectors,[81] and broadband THz sources and detectors.[79] But to date, few devices created by c-AFM lithography have been reported[89] outside of the LAO/STO system.

A two-dimensional electron system (2DES) can also be formed at the nonpolar/nonpolar oxide interface of CZO/STO by strain-induced polarization when the CZO layer is more than the critical thickness.[49-51] Here we report extreme nanoscale control of the nonpolar CZO/STO interface at room temperature using c-AFM lithography (Figure 23a). Conductive structures are stable with feature sizes as small as 1.2 nm at room temperature. A variety of nanodevices are created and characterized at low temperature, providing insight into the electronic confinement of the CZO/STO interface. The ability to create nanostructures at the nonpolar CZO/STO interface with the same c-AFM lithography technique expands the class of heterostructures which can be controlled at extreme nanoscale dimensions.

3.2 MATERIALS AND METHODS

High quality (001) CZO film is grown on top of (001) TiO_2-terminated STO substrate by pulsed laser deposition (PLD) in a 2D layer by layer growth mode. A thickness of the CZO is chosen to be close to the metal-insulator transition (eight unit cells), and the film thickness is monitored during growth by counting the intensity oscillations of the reflection high-energy electron diffraction (RHEED) pattern measured in-situ. Details of the growth conditions are reported elsewhere.[49] Terraces can clearly be seen from the AFM topography scan image (Figure 23b), confirming the CZO film is atomically smooth.

CZO/STO samples are patterned with standard photolithography using AZ4210 photoresist. The exposed CZO/STO after developing is etched with an argon ion mill (Commonwealth Scientific Ion Mill) at 500 W and 10 mA for 25 minutes. Electrodes contacting the interface are formed by filling the etched trenches with 4 nm of titanium and 25 nm of gold using a Perkin Elmer 6J sputtering system. Excessive metals are lifted off in Microposit Remover 1165 at 50°C for 18 hours. Bonding pads are sputtered onto the top surface with 4 nm titanium and 50 nm gold. The sample is finally cleaned in acetone and isopropyl alcohol with an ultrasonic cleaner, followed by oxygen plasma using an IPC Barrel Etcher, before measurement. The interface is found to be highly insulating (>0.5 GOhm between nearby electrodes which are separated by 2 μm) after sample processing.

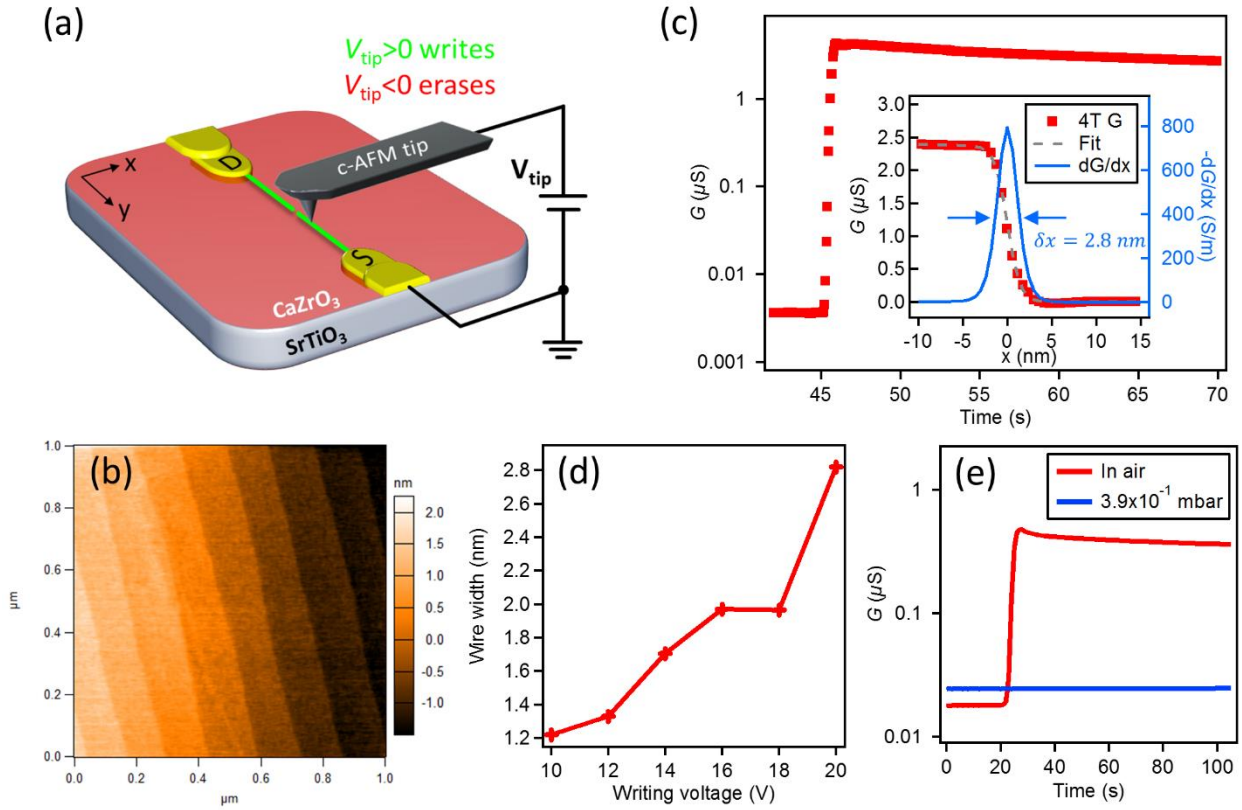

Figure 23 Creating and erasing nanostructures at the $CaZrO_3/SrTiO_3$ (CZO/STO) interface. (a) Schematic drawing of c-AFM lithography. Gold electrodes are in direct contact with the CZO/STO interface. Green wires indicate the nanoscale conducting regions at the interface created by scanning a positively biased AFM tip from one electrode to the other. The junction in the middle of the nanowire is formed by applying a negative voltage on the AFM tip and cutting across the nanowire. (b) AFM topography image showing an atomically smooth CZO surface. (c) The four-terminal conductance increases over three orders of magnitude when a nanowire is written. The inset shows the steep drop in conductance once the nanowire is cut. The width of the nanowire can be extracted by fitting to the conductance drop and calculating its corresponding differential conductance -dG/dx as a function of tip position x. The full-width at half-maximum of the nanowire is 2.8 nm. (d) Nanowire width plotted as a function of writing voltage. (e) Comparison of writing

in air and under modest vacuum. The nanowire here is ten times longer than the nanowire in (c) and the conductance background comes from photoconductance residue.

3.3 RESULTS AND DISCUSSION

3.3.1 Creating and erasing nanostructures at the CZO/STO interface

The c-AFM lithography set up is shown in Figure 23a. An Asylum Research MFP-3D AFM is used under an ambient condition with a typical relative humidity around 35% at 27°C, unless otherwise specified. The DC writing voltage is applied to the c-AFM tip (highly doped silicon) through a 1 GΩ series resistor, and the interface of CZO/STO is grounded during writing. Nanoscale conducting regions are created by applying a positive voltage (+20 V) on the AFM tip while scanning the tip in contact mode along a designed path. A sharp conductance jump can be observed once the path is complete (Figure 23c), indicating that a conducting channel has been formed at the interface. The positive threshold voltage for forming conducting channels is around +6 V. This process is reversible: when the AFM tip is biased with a negative voltage (-20 V) and moved across the existing wire, a steep drop in the conductance is observed (Figure 23c inset). The AFM topography image after c-AFM lithography shows no visible deformation of the sample surface, even after repeated write/erase cycles. The width of the conducting channel can be extracted by fitting the drop in the conductance to a function of the form $G(x) = c_0 + c_1 x + c_2 \tanh(x/h) + c_3 x \tanh(x/h)$[43] (where c_{0-3} are fitting coefficients, x is the tip position, and h is the cutting length) and calculating the full-width at half-maximum of the corresponding differential conductance dG/dx. The wire width extracted in the inset of Figure 23c is around 2.8

nm. As shown in Figure 23d, when the tip bias voltage decreases from 20 V to 10 V, the nanowire width at the CZO/STO interface decreases to 1.2 nm. The nanowires created at the CZO/STO interface remain extremely narrow at all writing voltages tested, in contrast to nanowires formed at the LAO/STO interface, where the wire width depends sensitively on the writing voltage.[43] Compared to nanowires defined by conventional lithographic processes, ultrathin conducting regions created by c-AFM lithography are electrostatically confined which have much smoother confinement profiles, and are physically separated from the surface charges that define their shape thus are less susceptible to atomic-scale defects.[35] Such high-quality and highly reconfigurable nanostructures, with dimensions comparable to most single-walled carbon nanotubes, hold great promise for alternative oxide-based nanoelectronics with length scales beyond the current semiconductor technology node, as well as offer new opportunities to study novel physics in CZO/STO heterostructures.

The ability to achieve a metal-insulator transition locally and reversibly by the same c-AFM lithography technique at a nonpolar/nonpolar interface naturally raises the question of the physical mechanisms responsible for the formation and suppression of conducting channels at complex oxide interfaces. To narrow down the possible physical mechanisms at play in the writing and erasing process, we compare the writing in air and under modest vacuum in a customized Nanomagnetics Instruments LT-AFM, as shown in Figure 23e. Before each writing, the sample is raster-scanned with a negative voltage to remove any remaining conducting patterns. The four-terminal conductance shows a well-defined jump (red line) when writing in air with a relative humidity around 43% at 22 °C. After erasing the existing nanowire, the AFM chamber is evacuated to a pressure of 3.9×10^{-1} mbar. The same four-terminal structure is then written with identical writing parameters, but no conductance jump is observed under this modest vacuum (blue

line). A subsequent writing is repeated after re-exposing the sample to air and a four-terminal conductance jump is again observed. The inability to write under vacuum is consistent with the same H_2O-mediated surface protonation process as with the LAO/STO system.[34, 86] LAO/STO has a critical thickness of four unit cells,[30] and three-unit-cell LAO/STO can be hysteretically switched between conductive and insulating states either by application of +/-100V[30] or by c-AFM lithography.[43] For this system, the polarization of the LAO layer brings the interface close to the metal-insulator transition. Application of strain (e.g., from LSAT substrate[33]) can shift the critical thickness due to strain-induced polarizations. The CZO layer is nonpolar, but is not lattice matched with the STO substrate. In this case, the polarization discontinuity arises solely due to strain-induced effects. When the strain-induced polarization is close to the metal-insulator transition, the interface can then be switched between conducting and insulating state through surface protonation arising from c-AFM lithography. Such a process allows numerous writing and erasing cycles without degradation of the oxide heterostructures, confirmed by repeated writing and erasing in the same region. The narrower nanostructures created at the CZO/STO interface may also be explained by variations in surface chemistry that result in a smaller water meniscus size formed under the AFM tip on CZO surface compared to LAO. Further insight into the writing and erasing mechanism could come from a more comprehensive study with different atmospheric conditions or surface adsorbates. For example, experiments similar to Ref. [34] could be used to gauge whether protons are the primary ionic species.

3.3.2 Tunable superconductivity in the nanowire device

At low temperatures, the electronic widths are expected to greatly increase[4, 18] due to the increase in dielectric permittivity of STO from 300 at room temperature to over 20,000 at low

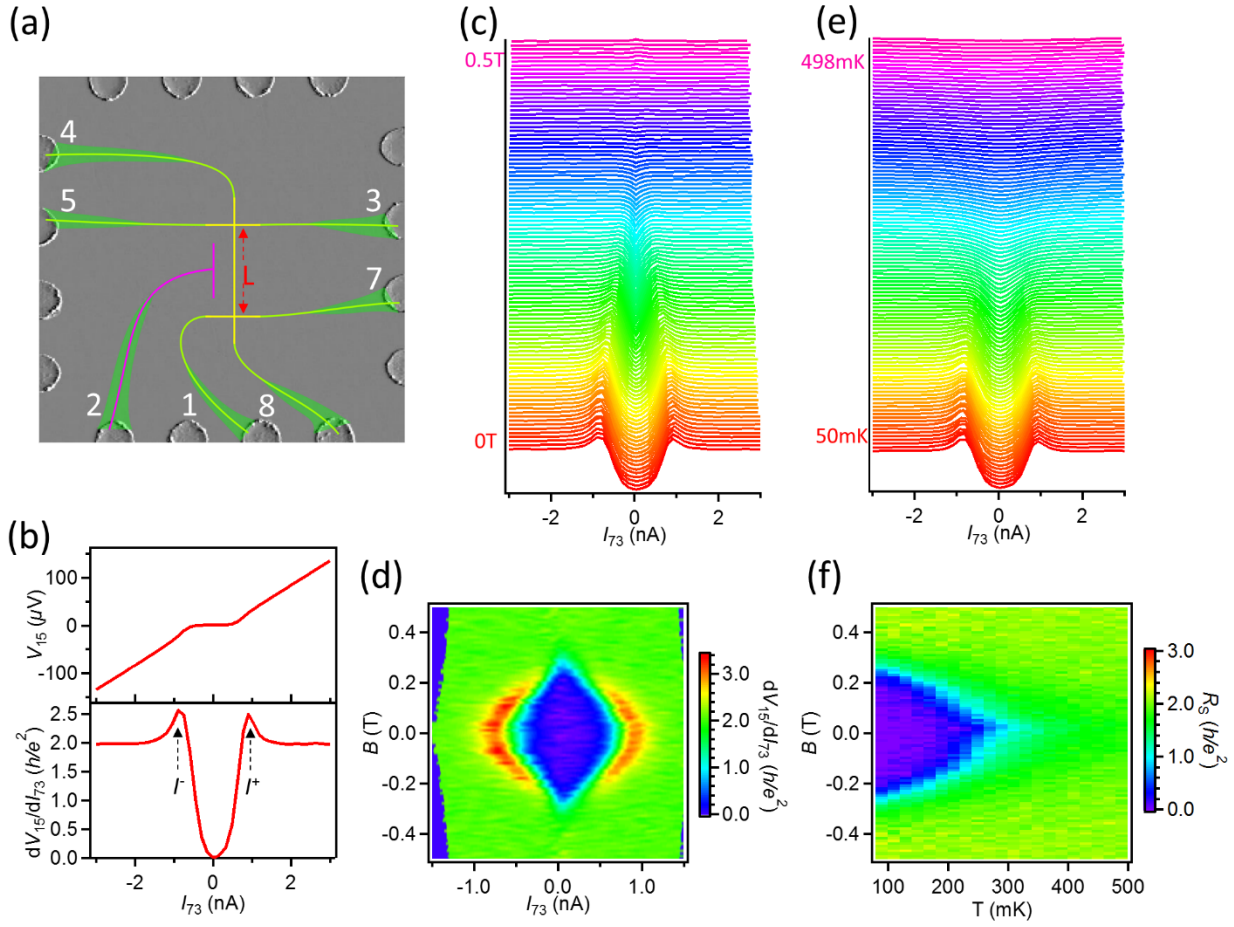

Figure 24 Superconductivity in a nanowire created at the CZO/STO interface. (a) Designed c-AFM lithography pattern overlaid on an AFM topography image of the canvas. The main channel length is L = 5 μm. (b) The four-terminal I-V curve (top) acquired at 0 T and 50 mK and the corresponding differential resistance dV/dI curve (bottom) show a superconducting state with zero resistance within the resolution of the measurement. The critical current is I_C = 0.9 nA. (c) dV/dI curves at 50 mK with increasing out-of-plane magnetic field through the superconducting transition. (d) dV/dI intensity map as a function of magnetic field and bias current. (e) Temperature-dependent dV/dI curves at zero magnetic field. (f) Complete temperature and field phase diagram. The normal state is restored for temperatures above 270 mK and field values above 0.26 T.

temperatures[10]. To investigate the low-temperature electronic properties of CZO/STO nanostructures, we focus on three types of devices, all created within the same 20 μm × 20 μm region ("canvas"). Before writing each device, the canvas is restored to a fully insulating phase by raster-scanning the entire canvas with a negative voltage, both vertically and horizontally at high resolution (5 nm spacing). Transport properties of a conducting nanowire at the CZO/STO interface are explored by writing a 5 μm-long nanowire device, as shown in Figure 24a. A T-shaped side gate, located 1.1 μm away from the main channel, acts to adjust the chemical potential of the nanowire. Magnetotransport measurements are taken in a Quantum Design PPMS dilution refrigerator with a superconducting magnet whose axis is oriented out-of-plane with respect to the sample surface. Four-terminal current-voltage (*I*-*V*) curves are acquired by sourcing voltage from electrode 7, measuring current I_{73} from electrode 3, and measuring the voltage V_{15} across electrodes 1 and 5. Source voltages are applied by a 24-bit digital/analog converters (National Instruments PXI-4461), which can also simultaneously perform 24-bit analog/digital conversion. The drain current is measured after amplified by a sub-femto-ampere current amplifier (Femto DDPCA-300). The four-terminal voltage drop is measured by a 1 TΩ input impedance true differential voltage amplifier (Femto DLPVA). The upper panel of Figure 24b shows the average of ten *I*-*V* curves, acquired at $T = 50$ mK and $B = 0$ T. A flat region is observed for small current values. The bottom of Figure 24b is the differential resistance d*V*/d*I* calculated from the averaged *I*-*V* curve in units of the resistance quantum (h/e^2), where *e* is the electron charge and *h* is Planck's constant. A superconducting state is observed, with zero resistance within the resolution of the measurement. We define the critical current I_C as the averaged current position of the two differential resistance peaks, i.e. $I_C = (|I^+| + |I^-|)/2$. In this device, $I_C = 0.9$ nA. In the superconducting state ($|I| < I_C$), there

is a finite resistance that increases with current, which may be attributed to thermally activated phase slips[90] or Joule heating.[91, 92]

The superconducting state disappears at elevated temperatures or higher magnetic fields. Figure 24c shows the differential resistance calculated from *I*-*V* curves acquired at 50 mK and under different magnetic fields from 0 T to 0.5 T with 0.005 T steps. Each curve is shifted by 0.1 h/e^2 for clarity. We denote the lowest differential resistance in the superconducting state ($|I| < I_C$) to be R_S and the differential resistance in the normal state ($|I| \gg I_C$) to be R_N. As the magnetic field increases through the superconducting transition, I_C gradually decreases while R_S and R_N both increase. Figure 24d shows an intensity map of the differential resistance as a function of magnetic field and bias current. The signal is symmetric and repeatable when reversing the direction of the magnetic field. There is an asymmetry with respect to the bias current, which will be discussed below. Similarly, Figure 24e shows the differential resistance calculated from *I*-*V* curves measured at zero magnetic field while stepping the temperature from 50 mK to 500 mK in steps of 4 mK. A broad transition from the superconducting state to the normal state is observed, which is usually explained by thermally activated phase slips as reported in other superconducting nanowires.[23] A complete phase diagram of R_S as a function of both temperature and magnetic field is shown in Figure 24f. Here we define the critical temperature T_C (field B_C) as the temperature (field) at which the differential resistance is half of R_N, yielding T_C = 270 mK and B_C = 0.26 T. The critical temperature and critical magnetic field observed for this system are consistent with superconductivity that originates primarily in the STO substrate.[23]

This superconducting state can also be tuned by applied gate voltages, as shown in Figure 25. *I*-*V* curves are measured at 50 mK and zero magnetic field with different gate voltages applied to the back of the STO substrate. When sweeping the back gate voltage V_{bg} from 0.28 to 2.18 V,

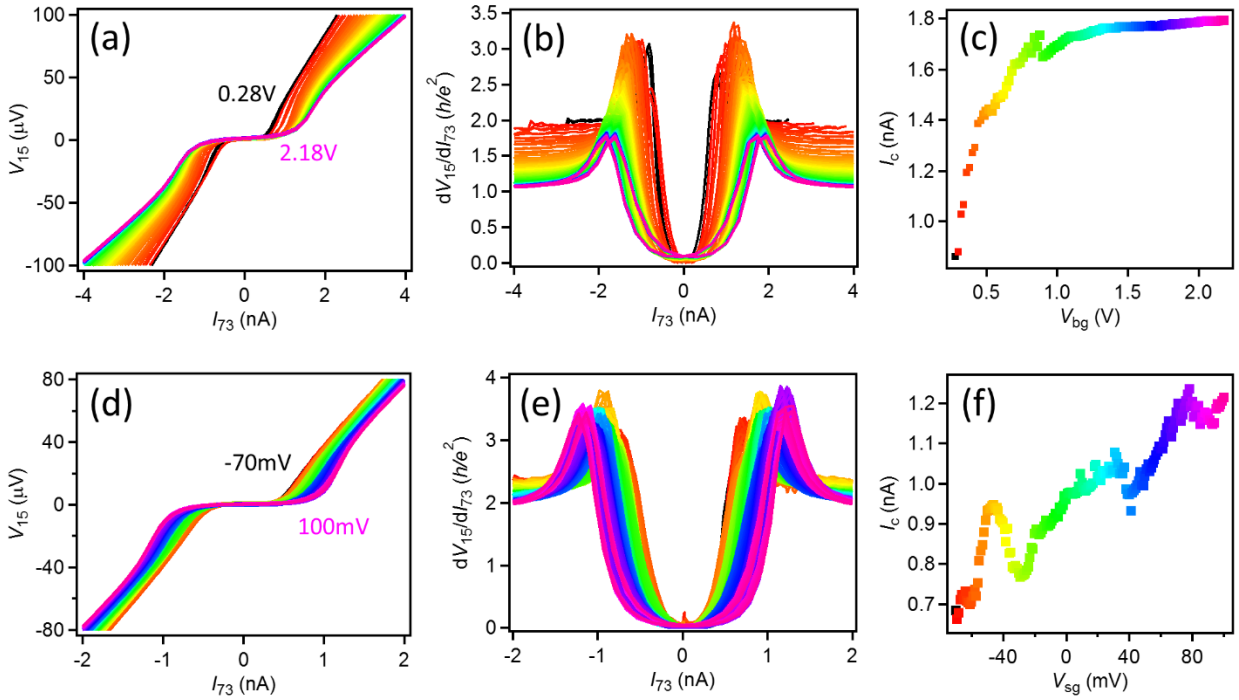

Figure 25 Gate tuning of superconductivity in the nanowire device. (a) and (b) *I-V* curves and the corresponding differential resistances at different back gate voltages. (c) Critical current I_C (extracted from (b)) increases with V_{bg} and saturates above 1.3 V. (d) and (e) *I-V* curves and the corresponding differential resistances at different sidegate voltages. (f) Critical current I_C (extracted from (e)) increases with V_{sg}.

the superconducting resistance R_S increases slightly, while the normal resistance R_N decreases by almost a factor of two (Figure 25b). The critical current I_C also increases with V_{bg} and saturates above V_{bg} = 1.3 V (Figure 25c). The gate-dependent resistance modulation in both the normal (R_N) and superconducting state (R_S and I_C) is consistent with a superconducting gap that depends non-monotonically with carrier concentration.[93] Note that the narrow width of the nanowires produces significant electric flux focusing, so a relatively small back gate voltage is sufficient to tune the carrier concentration in the thin nanowires.[94] The *I*-*V* curves exhibit hysteresis that increases with increasing V_{bg}, which has been attributed to motion of ferroelastic domains.[95] The asymmetry in the differential resistance intensity map (Figure 24d) provides additional evidence of this hysteretic behavior, where we only measured the *I*-*V* curves in one direction. Similar gate-dependent resistance modulation in both the normal and superconducting state can also be observed when tuning the device with a side gate (Figure 25d-e), except the critical current I_C continues to increase even at the largest side gate voltage tested (100 mV) (Figure 25f). Further tuning of the superconductivity might be available by increasing the side gate voltage range.

3.3.3 Quantum oscillations in the Hall bar device

Properties of 2D CZO/STO channels are investigated by writing a Hall bar structure (Figure 26) with channel width w = 0.5 μm and length L = 3 μm. This pattern is created by raster-scanning the c-AFM tip within the designed rectangular regions in both horizontal and vertical directions with a line spacing of 10 nm. The longitudinal Hall resistance R_{xx} (transverse Hall resistance R_{xy}) is measured as a function of magnetic field at 50 mK by sourcing voltage from electrode 1, measuring current from electrode 3 and measuring V_{xx} (V_{xy}) from electrode 2 (7) and electrode 5 (2). The mobility μ_{Hall} and the carrier density n_{Hall} extracted from the Hall measurement are 3,600 cm^2V^-

$^{1}s^{-1}$ and 2.47 × 10^{13} cm^{-2}, respectively. The n_{Hall} is comparable to other STO-based oxide heterostructures, while the μ_{Hall} is relatively high.[96-101] R_{xx} shows a large positive magnetoresistance and oscillations at higher magnetic fields, which are more obvious after subtraction of a smooth background and plotted as a function of 1/*B* (Figure 26c). Such oscillations resemble the Shubnikov-de Haas (SdH) effect, despite the modest mobility and high carrier density. A fast Fourier transform (FFT) shows a broad peak around 30.6 T, corresponding to a carrier density of n_{SdH} = 1.48 × 10^{12} cm^{-2}. The discrepancy of carrier densities obtained from low field Hall measurement and high field SdH oscillations have been widely reported in other STO-based 2D devices,[102-106] and recently it has been attributed to the naturally formed quasi-1D ferroelastic domain boundaries in these 2D systems, where the magnetic field depopulates the energy sub-bands.[4] Quantum oscillations are also observed in R_{xy}. The measured R_{xy} shows a slight deviation from antisymmetry for positive and negative magnetic fields, and an offset at zero field, which can be attributed to the mixing of R_{xx} and R_{xy}, and is likely enhanced by naturally occurring ferroelastic domain structure within the Hall bar channel.[107]

3.3.4 Quasi-ballistic transport in the waveguide device

To further characterize the electronic confinement of the interfacial nanostructures, a more complicated waveguide device that consists of two highly transparent barriers has also been written and characterized (Figure 27a). The barriers are 5 nm wide and separated by 50 nm and the total length of the main channel is 500 nm. This device is created in two steps. First, a positive voltage (+20 V) is applied to the AFM tip to write the main channel, then the tip is biased with a small positive voltage (+5 V) and moved along the same writing path, during which two negative voltage

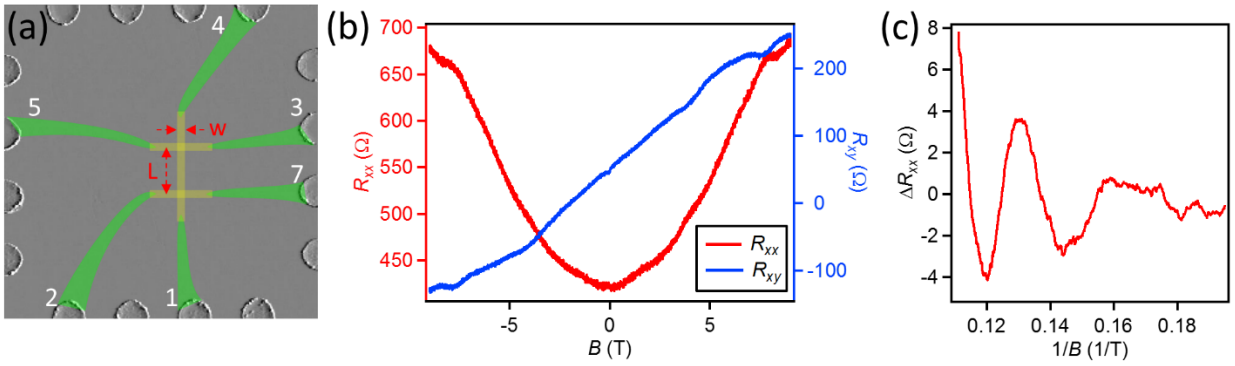

Figure 26 Hall bar device written at the CZO/STO interface. (a) Designed c-AFM lithography pattern overlaid on an AFM topography image of the canvas. The width is $w = 0.5$ μm and length is $L = 3$ μm. (b) R_{xx} and R_{xy} plotted as a function of magnetic field. The mobility and the carrier density extracted from the Hall measurement are 3,600 $cm^2V^{-1}s^{-1}$ and 2.47×10^{13} cm^{-2}, respectively. R_{xx} also shows large positive magnetoresistance and quantum oscillations that resemble the SdH effect. Additional features also present in R_{xy}. (c) Oscillations in R_{xx} after subtraction of a smooth background.

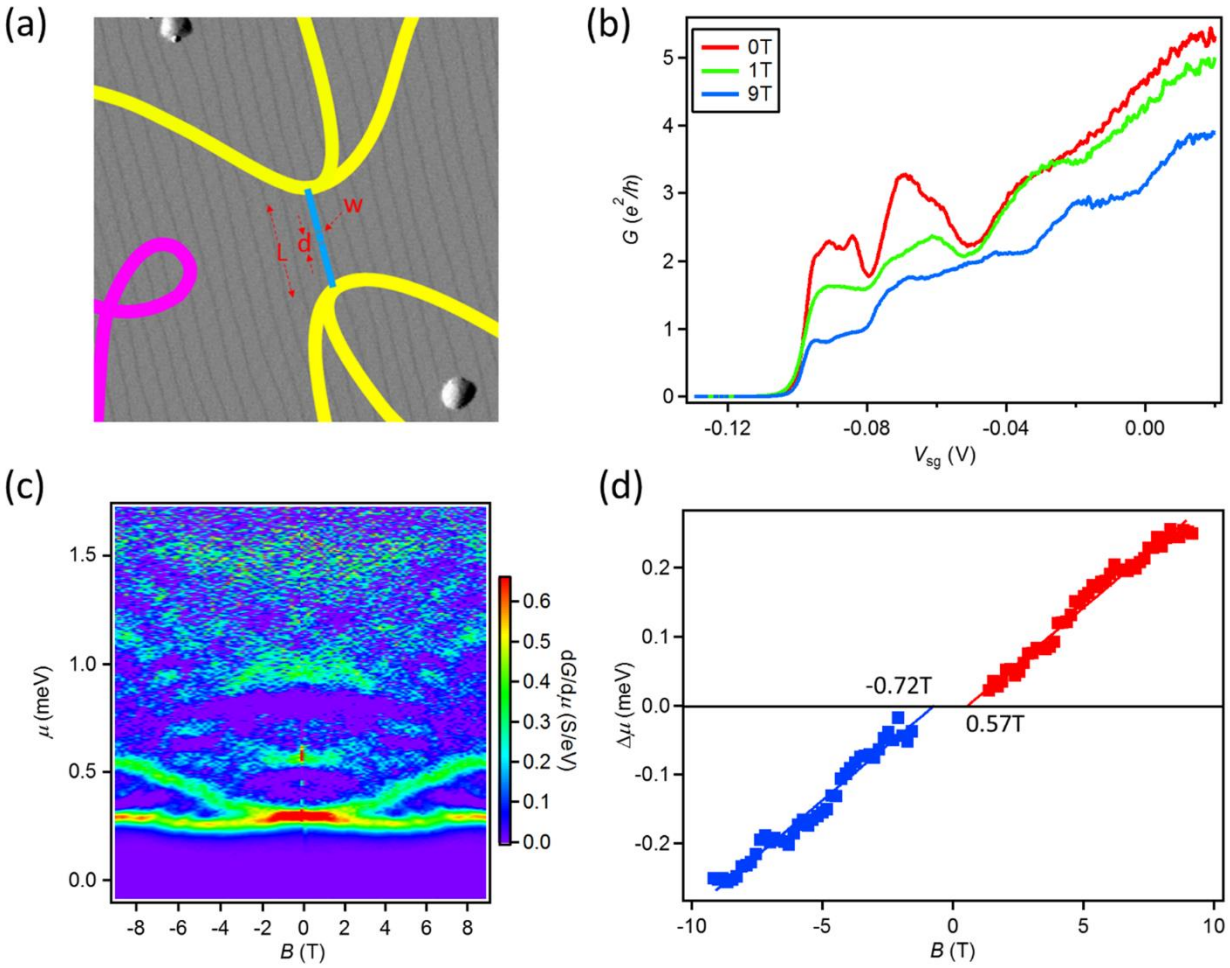

Figure 27 Waveguide device written at the CZO/STO interface. (a) Designed c-AFM lithography pattern overlaid on an AFM topography image of the canvas. The total length of the main channel is L = 500 nm, the width of the barrier is w = 5 nm, and the separation between the two barriers is d = 50 nm. (b) Zero-bias four-terminal conductance as a function of side gate voltage at 0 T, 1 T, and 9 T. Quantized conductance plateaus develop at high magnetic fields. (c) The transconductance as a function of chemical potential μ and magnetic field B shows peak splittings above a critical magnetic field. (d) The chemical potential difference of the split peaks as a function of magnetic field. Pairing fields can be extracted from the intercepts of the linear fit, and are larger than the upper critical magnetic field for superconductivity.

pulses (-11 V) are applied to create the two narrow barriers. The chemical potential μ of the nanowire segment between the two barriers is tuned by a side gate that is located 800 nm away from the main channel. Zero-bias four-terminal conductance $G = dI/dV$ is measured as a function of side gate voltages at 50 mK and under different magnetic fields (Figure 27b). At large negative side gate voltages, the waveguide conductance is tuned to zero. As the side gate voltage is increased, the four-terminal conductance increases to more than 5 e^2/h (conductance quantum) at 0 T (red line). Signatures associated with the superconducting regime appear as sharp increases in conductance. Such sharp increases disappear for magnetic fields $|B| > 0.26$ T (green line). The remaining additional features may be attributed to either quantum mechanical tunneling through the barriers, scattering due to impurities in the waveguide, or both. For an ideal coherent quantum waveguide, each spin-resolved energy sub-band contributes one conductance quantum (e^2/h) to the total conductance.[18] At 9 T, clear quantized plateaus near 1, 2, 3, and 4 e^2/h are resolved (blue line). However, the conductance steps are not precisely quantized at integer values of e^2/h. Nonetheless, the ability to tune the device to the lowest spin-resolved conductance plateau ($\cong e^2/h$) is a good indication that quasi-ballistic transport can be achieved in the waveguide created at the CZO/STO interface. The electronic width at low temperatures, while larger than the room-temperature width, is still significantly smaller than the measured scattering length.

The transconductance $dG/d\mu$ is calculated by taking derivative of the conductance curves with respect to the chemical potential μ (Figure 27c), revealing transitions where each new sub-band contributes to transport. The chemical potential μ is converted from V_{sg} by the lever-arm α, which can be extracted from the finite-bias spectroscopy measurement.[18] *I-V* curves are taken under different side gate voltages at 9 T and 50 mK. Figure 28 shows the corresponding transconductance map calculated by taking the derivative of dI/dV with respect to V_{sg}. Lever-arm

$\alpha = e\Delta V_{sd}/\Delta V_{sg}$, where the source-drain voltage difference ΔV_{sd} and side gate voltage difference ΔV_{sg} mark the same transition between adjacent subbands. α extracted here is around 12.2 μeV/mV, which gives a Landé g-factor $g = e\Delta V_{sd}/\mu_B B \approx 0.5$ (μ_B is the Bohr magneton). As mentioned above, signatures associated with the superconducting regime are observed near zero magnetic field and disappear at higher magnetic fields. The lowest two spin-resolved sub-bands are split with an offset $B_p \sim 0.6$ T (Figure 27d), signifying residual electron pairing outside of the superconducting regime.[52] Pairing field (B_p) can be extracted from the intercepts of the linear fits for both positive (0.57 T) and negative (-0.72 T) magnetic fields, and are larger than the upper critical magnetic field for superconductivity in this system (0.26 T). Such electron pairing without superconductivity has been reported in LAO/STO, where attractive electron-electron interactions are believed to suppress backscattering from impurities and lead to electron pairing without superconductivity.[52] The attractive electron-electron interaction is also believed to be responsible for the increased mobility in the nanowires created by c-AFM lithography at the LAO/STO interface when the channel width is reduced below 100 nm.[35]

The transconductance is also measured at $T = 500$ mK and $T = 900$ mK (Figure 29b-c), and we observe the same splitting even at 900 mK, which is far above the transition temperature for superconductivity (270 mK). It is also interesting to note that the electron pairing field appears to increase with increasing temperature, reaching $B_p = 3$ T at $T = 900$ mK (Figure 29d-f), in contrast to what has been observed in LAO/STO. Further experiments, such as characterizations of the temperature dependence of g-factor, are needed to understand the physical mechanism responsible for this increase.

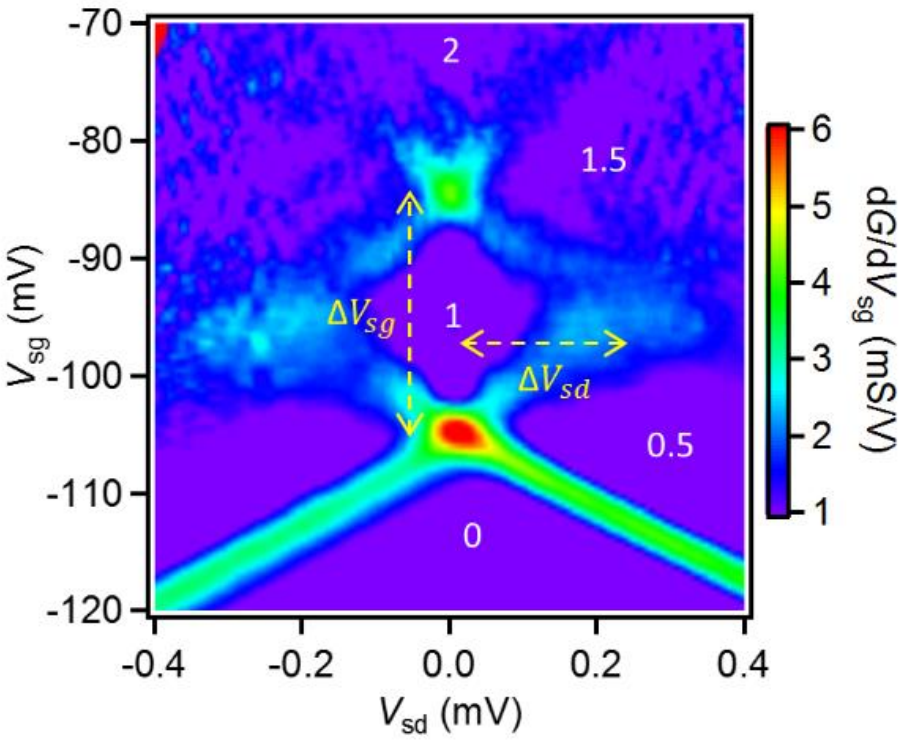

Figure 28 Transconductance of the waveguide device measured at 9 T and 50 mK. Each purple region represents a conductance plateau. Quantized conductance numbers are labeled accordingly. Bright regions represent transitions between different plateaus. The side gate coupling factor can be calculated by $\alpha = e\Delta V_{sd}/\Delta V_{sg}$. Here $\Delta V_{sd} = 0.25$ mV, $\Delta V_{sg} = 20.62$ mV.

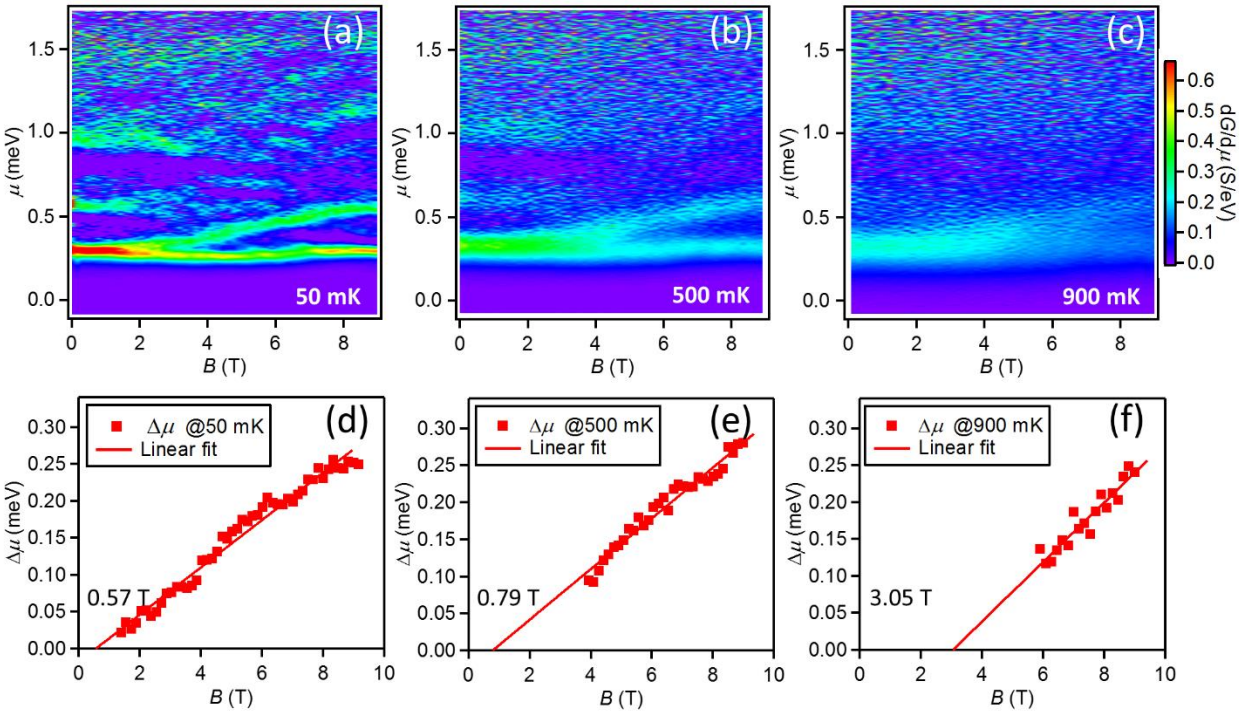

Figure 29 Temperature dependent zero-bias measurement in the waveguide device. (a) (b) and (c) Transconductances (same color scale) as a function of chemical potential and magnetic field acquired at 50 mK, 500 mK, and 900 mK, respectively. The peak splitting still exists even at 900 mK. (d) (e) and (f) show the corresponding linear fits to the chemical potential difference as a function of magnetic field at 50 mK, 500 mK, and 900 mK. The extracted pairing fields are 0.57 T, 0.79 T, and 3.05 T, respectively.

3.4 CONCLUSIONS

The ability to create arbitrary conducting nanostructures that can access quasi-1D, 2D, and local electronic properties of the complex oxide interface enables a new pathway to study fundamental questions of low-dimensional systems. Here, we have shown that c-AFM lithography can control the metal-insulator transition at the nonpolar CZO/STO interface, despite the lack of intrinsic polar discontinuity at the interface. The mechanism for writing/erasing has been attributed to a similar surface protonation/deprotonation process as in the LAO/STO system. Nanoscale conducting regions appear to be extremely narrow at room temperature. Nanodevices such as nanowires, Hall bars, and waveguides are created, through which tunable superconductivity, quantum oscillations, electron pairing outside the superconducting regime, and quasi-ballistic transport properties of the CZO/STO interface have been characterized. The success with extreme nanoscale control over the metal-insulator transition at the nonpolar CZO/STO interface opens up new opportunities both for fundamental research and future oxide-based nanoelectronics.

4.0 PHOTOCONDUCTIVE RESPONSE OF A SINGLE GOLD NANOROD COUPLED TO LAO/STO NANOJUNCTIONS

The contents of this chapter represent a collaborative work published in Jnawali, Chen, Huang, Lee, Ryu, Podkaminer, Eom, Irvin and Levy, *Applied Physics Letters* **106**, 211101 (2015).

Terahertz (THz) spectroscopy is an important tool that provides resonant access to free carrier motion, molecular rotation, lattice vibrations, excitonic, spin, and other degrees of freedom. Current methods using THz radiation suffer from limits due to diffraction or low-sensitivity, preventing application at the scale of single nanoscale objects. Here, the coupling between plasmonic degrees of freedom in a single gold nanorod and broadband THz emission generated from a proximal LAO/STO nanostructure is presented. A strong enhancement of THz emission is measured for incident radiation that is linearly polarized along the long axis of the nanorod. This demonstration paves the way for the investigation of near-field plasmonic coupling in a variety of molecular-scale systems.

4.1 INTRODUCTION

Studying a single nanoscale object, such as a single molecule or an isolated nanoparticle, by detecting its photoconductive response is one of the most challenging applications in nanoscale optics. Terahertz (THz) radiation is an ideal probe to detect and analyze such objects because it can couple to a range of excitations in molecules or nanoparticles, revealing their unique spectral

fingerprints.[108-112] The THz portion of the electromagnetic spectrum is of particular interest since it directly interrogates the dynamics of the free carriers without the complication of interband transitions.[110, 113] Current techniques involving THz radiation such as THz time-domain spectroscopy[113] are severely limited by diffraction, resulting in low spatial resolution and diminished detection sensitivity for nanoscale objects.

Efforts to improve the sensitivity of THz spectroscopy have focused on enhancing the interaction between the THz radiation and the specimen. For example, waveguide-assisted THz sensing,[114-117] metamaterial-based THz sensors,[118] and nanoslit-based techniques[119, 120] have been successfully employed for a variety of spectroscopic investigations on thin layers of biomolecules, explosives, and drugs. However, the necessary spatial resolution or sensitivity to detect single nanoscale objects has not been achieved using the aforementioned techniques. Surface-enhanced methods[121-124] are particularly promising for molecular-scale spectroscopy by exploiting local field enhancement in the vicinity of a plasmonic nanostructure. However, it requires lengthy lithographic fabrication procedures for patterning nanoscale plasmonic structures such as a narrow constriction or apertures and proper positioning technique to locate the specimen. Signal-to-noise is also an issue due to the low transmission through these sub-wavelength apertures.

Recently Ma *et al.*[79] have demonstrated a broadband THz spectrometer operating at 10 nm length scales, opening up the possibilities for THz spectroscopy at molecular scales. The nanojunction device is fabricated by writing nanowires at the interface of an LAO/STO heterostructure using c-AFM lithography.[43, 82] THz field is generated and detected using the same nanojunction by illuminating short laser pulses in a pump-probe setup, thus allowing the probing of the ultrafast photoresponse of a nanoscale object located on the junction. The writing

cycle can be accomplished reversibly, i.e., the nanojunctions can be formed or reformed on demand, enabling the object to be first located with the AFM and then a nanojunction formed around it for optical measurements.

Here, we demonstrate some of the promises of this technique by probing the photoconductive response of a single isolated gold nanorod (AuNR) on an LAO/STO sample. AuNR is of particular interest because it exhibits localized plasmon resonances,[125-129] which cause strong enhancement of radiative properties such as absorption and scattering.[130-134] As will be discussed in more detail below, the photoconductive response is measured by detecting induced THz fields at two orthogonal polarizations of the incident laser pulses with respect to the nanorod axis. The THz field is generated at the nanojunction of the LAO/STO nanowire device via optical excitation. Since a single AuNR is precisely positioned at the nanojunction during device writing process, the effective interaction with its plasmonic fields will be probed by detecting the change of THz field at on and off-resonance conditions.

4.2 MATERIALS AND METHODS

LAO/STO heterostructures are fabricated by growing a 3.4-unit cell thick (~1.2 nm) LAO film on a TiO_2-terminated STO(001) substrate using pulsed laser deposition (PLD). The LAO thickness is calibrated by in-situ monitoring of reflection high-energy electron diffraction (RHEED) spot intensity during growth. Details about growth conditions and fabrication of electrical contacts to the LAO/STO interface are described elsewhere.[33] A commercially available organic AuNR solution (Nanopartz Inc.) was used to deposit nanorods on a patterned LAO/STO sample. Prior to deposition, AuNR was characterized by optical absorption measurements using a UV-vis

spectrophotometer (Lambda 35, Perkin Elmer). The collected light signal, i.e., the extinction spectrum (absorption and scattering response), of AuNRs dispersed in an aqueous solution is shown in Figure 30. As expected from the light scattering properties of AuNR,[125-128] the spectrum exhibits two localized plasmon resonances that correspond to light-induced electron oscillations perpendicular and parallel to the long axis of the rods. The parallel or longitudinal mode peaks at 810 nm, while the perpendicular or transverse mode peaks at 517 nm. The resonance peaks are inhomogeneously broadened due to the intrinsic polydispersity in nanorod size.

Since the original AuNR solution is highly concentrated and dissolved in organic solvents, it is necessary to prepare a clean and residue free AuNR solution, which preserves the clean surface of LAO/STO even after nanorod deposition. The original AuNR solution was diluted by 1/10 of the original concentration by adding deionized water and mixing in an ultrasonic bath for one minute. The resultant AuNR solution was then centrifuged at 6,000 rpm for ten minutes and the supernatant was gently removed. The remaining precipitate of the AuNR solution was re-dispersed in deionized water and centrifuged again. The centrifuging process was repeated three times to completely remove excess residue. In order to deposit the nanorods on the substrate surface, the sample was immersed in the prepared AuNR solution for three minutes. The sample was then washed for several seconds in deionized water followed by an ethanol rinse, and finally dried with nitrogen gas. An AFM is used to identify a single AuNR. C-AFM lithography is then used to define a four-terminal interfacial nanowire device with a nanojunction underneath the single AuNR (Figure 31a). All lithography procedures are performed under ambient conditions with a typical temperature of 27˚C and relative humidity of 28%.

Figure 31a shows the non-contact AFM image of AuNRs deposited on LAO/STO sample. Several single, multiple, and clusters of nanorods are clearly visible as blue dots. Among them,

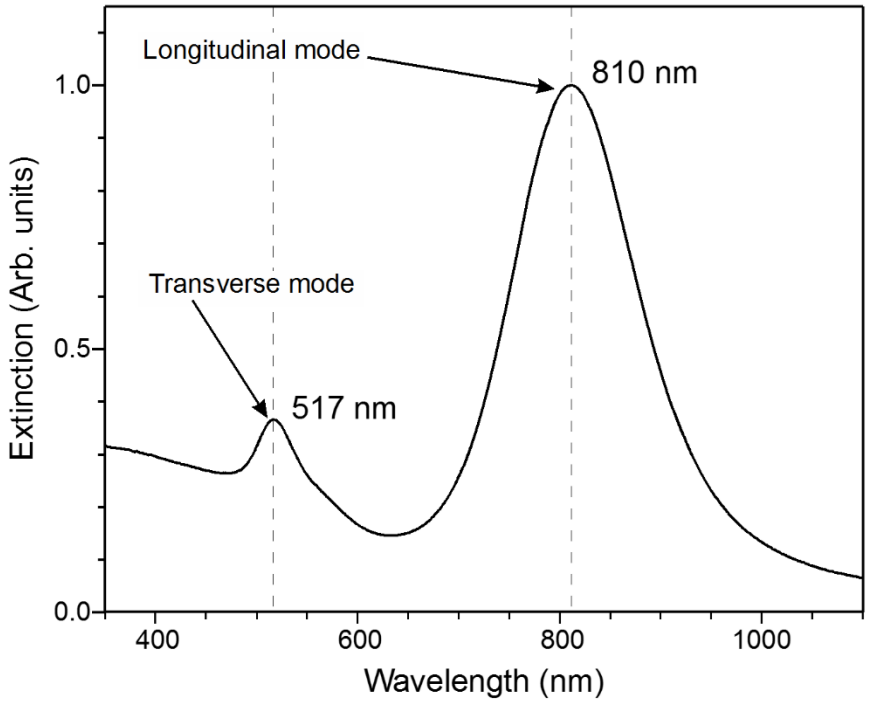

Figure 30 UV-Vis extinction spectra acquired from an aqueous solution of gold nanorods (AuNRs). Two broad peaks at near-Infrared and visible spectral regions are due to localized plasmon resonances parallel to the long axis of the AuNR and perpendicular to it. Plasmon resonance at 810 and 517 nm are denoted as longitudinal and transverse modes, respectively.

single isolated AuNRs are identified by performing a high-resolution topographic image as shown in Figure 31b. The height profiles are measured along two orthogonal directions indicated by ∥ and ⊥, i.e., along the long axis of the nanorod and perpendicular to it, respectively. The length of a single AuNR is 80 nm and the width is 40 nm, as confirmed by AFM height profiles (Figure 31c). The four-terminal interfacial nanowire device is created by moving a c-AFM tip with positive bias along the sketched region, as shown in Figure 31a. The dashed white lines correspond to the interfacial nanowires, which are connected to metallic gold electrodes by "virtual electrodes" (green triangles). Virtual electrodes are created in a wedge-shaped pattern using a tip voltage $V_{tip} = +20$ V and tip scanning speed of $v_{tip} = 400$ nm/s to form a robust electrical contact to the oxide interface, followed by curved single lines from one electrode to another using a $V_{tip} = 15$ V and $v_{tip} = 400$ nm/s.

To verify that the nanorod is located precisely on the path of the nanowire, a non-contact AFM image is acquired before and after the writing process. During c-AFM lithography, the conductance between the electrodes and conductance decay rate are monitored, as shown in Figure 32. There is a conductance jump when two lines are connected to each other, indicating the formation of a fully conducting path, i.e., an uninterrupted interfacial nanowire at the interface. The width of the nanowire is approximately 10 nm, estimated from writing and cutting experiments performed under similar conditions. As a final and crucial step, a nanojunction is created directly underneath the AuNR by softly approaching the negatively biased tip in non-contact-mode. Once the AuNR image is scanned, the tip is moved towards the edge of the rod and softly engaged on the nanorod surface. As soon as the tip touches the surface of the nanorod, a junction is created, which is identified by a sharp decrease of conductance between the source (*S*) and drain (*D*) electrodes, as indicated by red arrow in Figure 32. After making the junction, a close-up image is

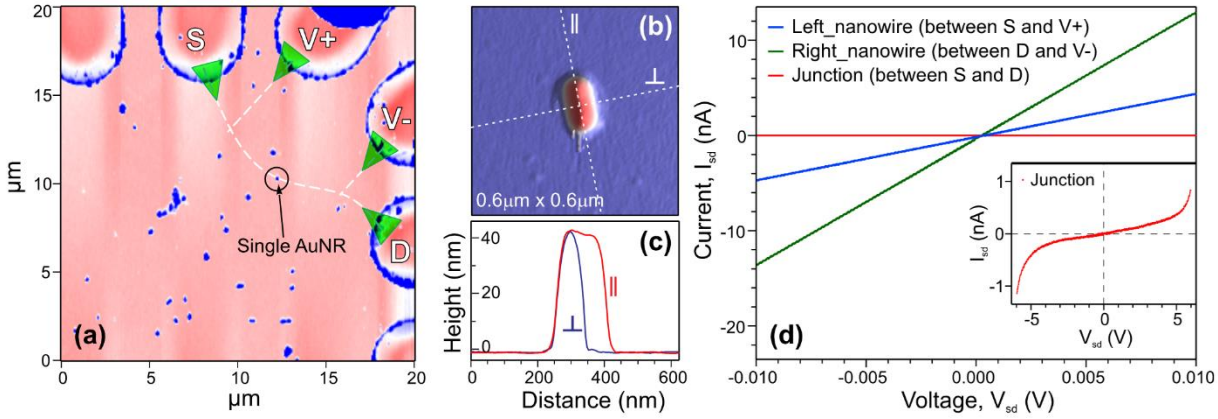

Figure 31 LAO/STO nanojunction device targeting a single AuNR. (a) non-contact AFM height image showing the surface morphology of AuNRs deposited on LAO/STO sample. The upper right side of the sample is used to sketch-write four-terminal nanojunction devices using c-AFM lithography. White dashed lines are the writing path for nanowire device and green structures show the virtual electrodes to connect wires to the gold electrodes, which are connected to the interface. Black arrow points to a single AuNR located on the path of the nanowire. (b) 3D view of an AFM height image of a single AuNR. (c) AFM height profiles across the single AuNR along parallel (red curve) and perpendicular (blue curve) to the longer axis of the nanorod, as indicated by the white dashed line in (b). (d) Typical two-terminal current-voltage (*I*-*V*) characteristics of the nanowire device measured between the electrodes as indicated in (a). The inset shows the typical nonlinear *I*-*V* curve between the source (*S*) and drain (*D*) electrodes, indicating the formation of nanojunction.

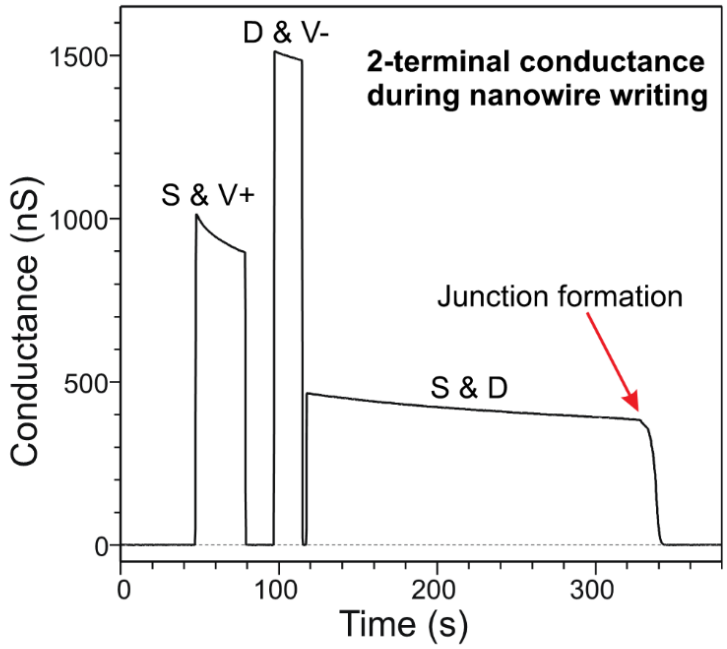

Figure 32 Typical two-terminal conductance of nanowires during fabrication of a four-terminal device by c-AFM lithography. As soon as the writing path is finished by scanning the positively biased tip from one electrode to another as indicated, there is a sharp jump of conductance and it decays slowly due to exposure to ambient conditions. Nanojunction is created between source and drain electrodes (*S* & *D*) by cutting (erasing) the nanowire path with negatively biased tip. As soon as the junction is created, conductance drops to zero as shown by the red arrow.

recorded again in non-contact mode to ensure that the nanorod has not been displaced following the creation of the junction. The sample is then quickly mounted into a cryostat integrated to the optical setup.

The nanojunction device is characterized at low temperature (120 K) by performing current-voltage (*I*-*V*) measurements between each electrode pairs. Figure 31d shows typical two-terminal *I*-*V* curves acquired by connecting different electrodes. As expected, the left and right nanowires without a junction exhibit linear *I*-*V* characteristics, while the nanowire between *S* and *D*, which has a nanojunction located at the AuNR, shows a typical nonlinear *I*-*V* curve. The junction width is larger than typical nanojunction[79] created by direct cutting of the nanowire, as indicated by large threshold voltages for conduction (> 1 V) (see inset of Figure 31c). These measurements also show that the device is behaving as expected, without any leakage or decay of the interface conductance.

4.3 RESULTS AND DISCUSSION

The steady-state photoresponse is measured electrically by focusing the laser spot onto the nanojunction using a $100\times$ microscope objective with $NA = 0.73$.[79, 81] A constant DC bias (10 mV) is applied between the *S* and *D* electrodes. Two voltage-sensing electrodes are used to measure the photoinduced differential voltage drop $V_{ph} = V_{+} - V_{-}$. An optical chopper modulates the laser beam at a frequency of 2 kHz, and the resulting signal ΔV_{ph} is measured using a lock-in amplifier. A photoconductive map is generated by measuring ΔV_{ph} while raster scanning the focused laser spot. A laser fluence of $10\ \mu J/cm^2$ is used for steady-state measurements. The reflected laser light is simultaneously collected using a photodiode via a separate lock-in amplifier,

allowing the polarization dependence detection of the reflectance of the AuNR deposited sample to be probed. All the optical measurements were performed at 120 K.

4.3.1 Polarization-dependent optical reflectance

Optical reflectance measurements are performed using a Ti: Sapphire laser centered at 800 nm (average power of 200 mW, 30 fs pulses at a repetition rate of 100 MHz). At this wavelength, the AuNRs show up clearly due to the plasmonic enhancement. In addition, the reflectance contrast varies with the polarization angle of the incident laser pulse, as shown in Figure 33a and b. When the laser polarization is parallel to the long axis of the nanorod, i.e., in resonance with the longitudinal mode, the scattering efficiency increases and a relatively high reflectance contrast is observed. To compare the polarization dependence reflectance contrast, the position of each single, multiple and clusters of AuNRs are marked by black circles. Black arrow shows the position of the single nanorod located on the nanojunction device. Spatial mapping of photocurrent is performed by applying a 10 mV DC bias voltage between the *S* and *D* electrodes. Figure 33d shows that the simultaneously measured reflectance and photocurrent scans overlap with each other. The spatial matching between photocurrent maximum and the reflectance maximum in the vicinity of nanorod position verifies the precise alignment of the single AuNR on the junction.

4.3.2 Plasmonic interaction with induced THz field

The ultrafast photoconductive response of the single AuNR is measured by recording the induced THz emission from the nanojunction by employing a pump-probe autocorrelation technique using

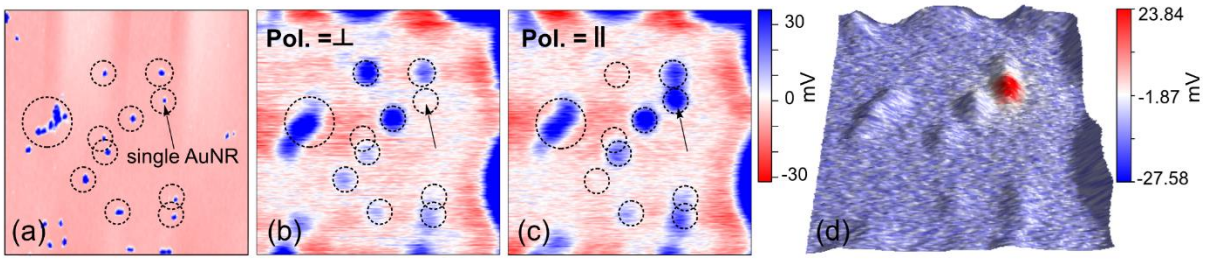

Figure 33 Identification of a single AuNR at the nanojunction device on the LAO/STO sample by using non-contact AFM height topography, optical reflectance, and photocurrent scan. (a) Non-contact AFM height scan acquired before writing the device. (b) and (c) Optical reflectance images recorded at 800nm under two polarization conditions: perpendicular and parallel to the long axis of the nanorod, respectively. Reflectance signal is only visible for some nanorods, which are in resonance with longitudinal plasmon mode of the nanorod at 800nm. (d) Scanning photocurrent map overlaid on simultaneously recorded reflectance image (c), showing the precise positioning of a single AuNR on the nanojunction. All images have the same scan size ($12 \times 12\ \mu m^2$).

ultrafast laser pulses. A DC bias of -1 V is applied between the *S* and *D* electrodes and the photoinduced electrical signal ΔV_{ph} is detected as a function of pump-probe delay time. Details of the optical setup and data acquisition method are described elsewhere.[79] During the measurements, the pump and probe fluences are kept sufficiently low to minimize heating ($25\ \mu J/cm^2$). Spatial mapping of the ultrafast photoconductive response is obtained by recording time resolved ΔV_{ph} at different locations around the nanojunction region. An optical polarizer is used to change the polarization state of both pump and probe pulses simultaneously. Here, we note that both pump and probe laser pulses are polarized along the same direction to generate THz emission because orthogonal polarization cancels out the third-order nonlinear coefficient (χ^3) in STO.

A previous study has confirmed that the THz field is spatially confined,[79] which allows us to probe any interaction caused by the single AuNR positioned at the junction. Figure 34a displays the THz time-domain signals and the corresponding power spectra (inset) measured at two orthogonal polarization conditions of the laser pulses with respect to the single AuNR orientation located at the nanojunction. Each THz waveform represents an average of 100 sequentially acquired time-delay scans. When the laser is polarized parallel to the long axis of the AuNR, the THz signal is enhanced by approximately a factor of two compared to the perpendicular polarization. To confirm that this enhancement is spatially confined in the vicinity of the nanojunction, spatial mapping of both time-domain signal and power spectra are recorded at two polarization conditions without changing the data acquisition parameters and laser fluences. As shown in Figure 34b-e, there is a significant change in the THz response (both signal distribution and the maxima) for the two polarization directions. Such enhancement is directly associated with

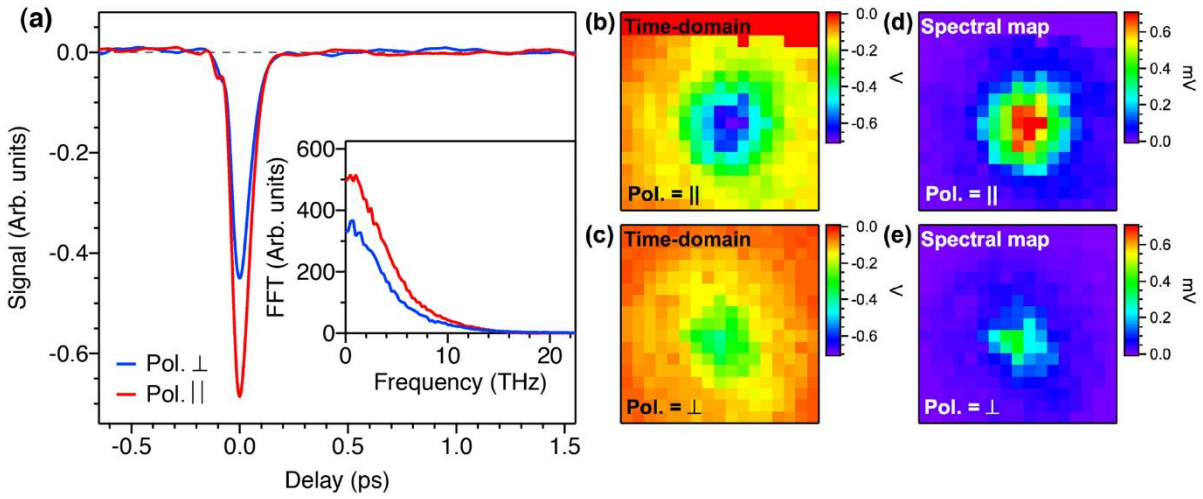

Figure 34 Plasmonic interaction of a single AuNR with the induced THz field at the nanojunction device on LAO/STO heterostructure. (a) Time-domain signals of the generated THz emission at the nanojunction measured at two orthogonal polarization states of the incident laser pulses with respect to the nanorod orientation. The inset shows the corresponding power spectra. (b)-(c) Time-averaged spatial mapping (8×8 μm^2) of time-domain signals at the maxima in the vicinity of the nanojunction at two different polarization states. (d)-(e) Spectral amplitude mapping at the maxima (at 0.8 THz) of the corresponding time-domain signals. Both mappings are shown with equivalent color scales. The THz field enhances almost a factor of two for parallel-polarized laser pulses as compared with the signals from perpendicularly polarized laser pulses, which can be attributed to enhanced efficiency of scattering properties of a single AuNR at the resonance.

the plasmonic coupling with induced THz emission at the nanojunction because the scattering efficiency of AuNR is stronger at parallel polarization conditions. While consistent with previous works on different systems,[135-137] this demonstration offers a unique capability to probe single nanoscale objects.

4.4 CONCLUSIONS

In conclusion, we have demonstrated the photoconductive response of a single isolated plasmonic AuNR coupled to a nanoscale LAO/STO junction. The photoconductive response of this coupled system is measured by detecting plasmonic enhancement of the photoinduced THz emission at the nanojunction. A strong plasmonic enhancement occurs when the incident laser is polarized along the long axis of the AuNR. This technique shows promise for measuring THz and plasmonic properties of single nanoscale objects with unprecedented resolution.

5.0 OVER 100-THZ BANDWIDTH SELECTIVE DIFFERENCE FREQUENCY GENERATION AT LAO/STO NANOJUNCTIONS

The contents of this chapter represent a collaborative work by Chen, Sutton, Lee, Lee, Li, Eom, Irvin and Levy, which has been submitted for publication.

The ability to combine continuously tunable narrow-band terahertz (THz) generation that can access both far-infrared and mid-infrared regime with a nanometer-scale spatial resolution holds great potential for uncovering underlying light-matter interactions as well as realizing selective control of rotational or vibrational resonances in nanoparticles or molecules. Here, selective difference frequency generation with over 100 THz bandwidth through femtosecond optical pulse shaping is reported. The THz emission is generated at nanoscale junctions at the interface of LAO/STO defined by conductive atomic force microscopy lithography, with the potential to perform THz spectroscopy on individual nanoparticles or molecules. Numerical simulation of the time-domain signal helps to identify different contributing components for the THz generation. This ultra-wide bandwidth tunable nanoscale coherent THz source transforms the LAO/STO interface into a promising platform for integrated lab-on-chip optoelectronic devices with various functionalities.

5.1 INTRODUCTION

Electromagnetic waves at terahertz (THz) frequencies allow resonant interactions with matter through various intrinsic low-energy excitations, revealing information related to lattice, charge and spin degrees of freedom. In the past few decades, extensive research efforts have focused on developing narrow-band THz radiation sources in both far-infrared (<10 THz)[138] and mid-infrared (10-100 THz)[139] regimes, due to their potential to provide insight into the fundamental physics of matter by selective excitations of different resonances. For a large number of applications, including spectroscopy,[140] inspection,[108] communication,[141] and coherent control,[142] tunability of the narrow-band THz radiation is required. On the other hand, THz techniques are also often limited by spatial resolution.[143, 144] Owing to the relatively long wavelength of THz radiation, diffraction usually limits the spatial resolution to the order of 10-100 um, making it difficult to resolve features much below this scale. Several techniques have been pursued to reach a nanometer-scale spatial resolution, such as combining THz radiation with scattering-type near-field scanning optical microscopy[145] or scanning tunneling microscopy[146]. However, to date, a continuously tunable, quasi-monochromatic THz source that can cover both the far- and mid-infrared regime with sub-10 nm spatial resolution is not available.

Here, we report >100 THz bandwidth selective difference frequency generation at $LaAlO_3/SrTiO_3$ (LAO/STO) nanojunctions through femtosecond optical pulse shaping. Selected frequency components of a sub-7 fs ultrafast pulse are mixed at the nanojunction through the third-order nonlinear effect in STO,[79] and their frequency difference results in narrow-band THz emission. By controlling the selected frequency components, the frequency of narrow-band THz emission can be tuned from far-infrared to mid-infrared regime. The spatial resolution of this THz source is determined by the nanojunction size, typically around 10 nm, but can be as small as 2

nm,[43, 79] thus realizing an ultra-broad bandwidth, continuously tunable, quasi-monochromatic THz source with a spatial resolution comparable to a single nanoparticle or even a single molecule.[147]

5.2 MATERIALS AND METHODS

The LAO/STO samples are grown by pulsed laser deposition. A thin film (3.4 unit cells) of LAO is deposited epitaxially on the (001) TiO_2-terminated STO substrate at 550 °C and in an oxygen pressure of 10^{-3} mbar, with its thickness monitored in-situ by high-pressure reflection high-energy electron diffraction (RHEED). This thickness is just below the critical thickness of the metal-insulator transition, resulting in an insulating interface. Additional details of the growth method are described elsewhere.[33] Electrical contacts to the interface are fabricated by conventional photolithography, where pre-defined regions are etched by Ar^+ ion milling (25 nm) then filled with Ti/Au (4 nm/25 nm). A second layer of Ti/Au is added on top of the LAO surface for wire bonding. The LAO/STO nanojunctions are created by conductive atomic force microscopy (c-AFM) lithography,[43] as shown in Figure 35. A positively biased AFM tip, scanned along a line in contact over the LAO surface, locally charges the LAO surface with protons,[34, 86] which then attract electrons to the buried interface to form a conducting nanowire with a typical width of 10 nm. A negatively biased AFM tip scanned over the conducting regions removes the adsorbed protons, restoring the interface to an insulating state. Of particular relevance to this work is the "nanojunction" pattern, in which a nanowire is created with a nanoscale (~10 nm) insulating gap (Figure 35b).

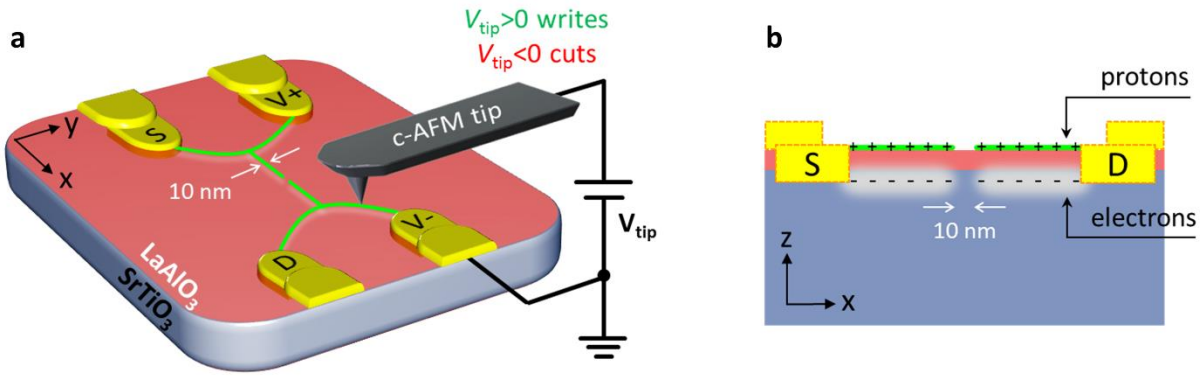

Figure 35 Schematic drawing of the four-terminal nanojunction device at the interface of LAO/STO for selective difference frequency generation. a Conductive atomic force microscopy (c-AFM) lithography. Gold electrodes are patterned by conventional photolithography to form direct contact with the LAO/STO interface. The green wires represent the designed device geometry. A positively-biased AFM tip writes the conducting nanowires in contact mode, while a negatively-biased AFM tip creates a nanojunction by cutting across the nanowire. **b** Side view of the sample shows that the c-AFM lithography defined device is located at the interface of LAO/STO heterostructure. Both nanowires and the nanojunction have a spatial confinement around 10 nm. The dimensions here are not to scale.

A four-terminal structure with a nanojunction in the middle (Figure 35a) is designed and created at the LAO/STO interface for the selective difference frequency THz generation, where electrodes labeled *S* and *D* are used to apply a DC bias voltage V_{dc} across the nanojunction, and two voltage sensing electrodes (V^+ and V^-) are used to measure the induced photovoltage change by ultrafast laser pulses, which will be described in detail below. The four-terminal geometry provides an accurate measurement of the photo-induced voltage change across the nanojunction, since any voltage drops in the leads, external wires or imperfect contacts are eliminated in this geometry.

Figure 36a shows the schematic drawing of the experimental setup. The ultrafast pulses from a sub-7 fs Ti: Sapphire oscillator (Spectra-Physics Rainbow 2 UHP) are directed into an optical pulse shaper based on a dual-mask spatial light modulator (SLM, Jenoptik SLM-S640d), where different wavelengths are spatially separated by a grating and focused onto different pixels of the SLM. Both the amplitude and the phase of the ultrafast pulse can be controlled independently. Here we focus on spectral amplitude control. After the pulse shaper, the manipulated pulses are redirected to a compact Michelson interferometer, which has two approximately equal length arms. A p-polarized 50/50 ultrafast beam splitter (BS) splits the input pulses into two beams. The reflected beam incident normally onto a plane mirror (PM) that is mounted on a piezoelectric stage (PS) which serves as an optical delay line. The transmitted beam reflects off a plane mirror that is mounted on a mechanical stage, which provides coarse adjustment of the time delay. Both beams are re-combined by the same beam splitter after normal reflection and then focused on the nanojunction by an objective (OB). During the measurement, the delay line is scanned continuously from negative to positive time delay values. A DC bias voltage ($V_{dc} = -550$ mV) is applied to electrode *S* through a 50 Ω impedance analog output port, while electrode

D is grounded. The photovoltage, which is the voltage difference $\Delta V = V^+ - V^-$ between the two voltage sensing electrodes, is measured and amplified by a differential voltage amplifier (DVA) with 1 MΩ input impedance, and recorded as a function of the time delay τ.

Figure 36b shows an example of the pulse spectral amplitude control by the pulse shaper. The red curve represents the full spectrum from the Ti: Sapphire oscillator without any spectral amplitude manipulation. A broad spectrum ranging from 650 nm to 920 nm is measured by a spectrometer. By applying an appropriate voltage to each pixel of the SLM, the output at all wavelengths can be efficiently suppressed (green curve). We can then specifically select one, two or a few wavelengths to pass through the SLM, while keeping all the other wavelengths suppressed. The blue curve shows a configuration in which light at 735 nm and 768 nm is allowed to pass through the SLM, while other wavelengths are suppressed.

5.3 RESULTS AND DISCUSSION

5.3.1 Experimental results

To demonstrate the ultra-broad bandwidth selective difference frequency generation capability at the LAO/STO nanojunction, we perform nonlinear wavelength mixing experiments. We select 35 different fundamental wavelength pairs with the frequency difference within each pair ranging from 2 THz to 106 THz. The total input excitation power is on the order of 100 μW. For each fundamental wavelength pair, the amplified photovoltage ΔV is recorded as the optical time delay line varies from τ =-500 fs to +500 fs, and the same measurement is repeated 40 times for averaging purposes. Figure 37a shows six representative averaged time-domain signals, with their

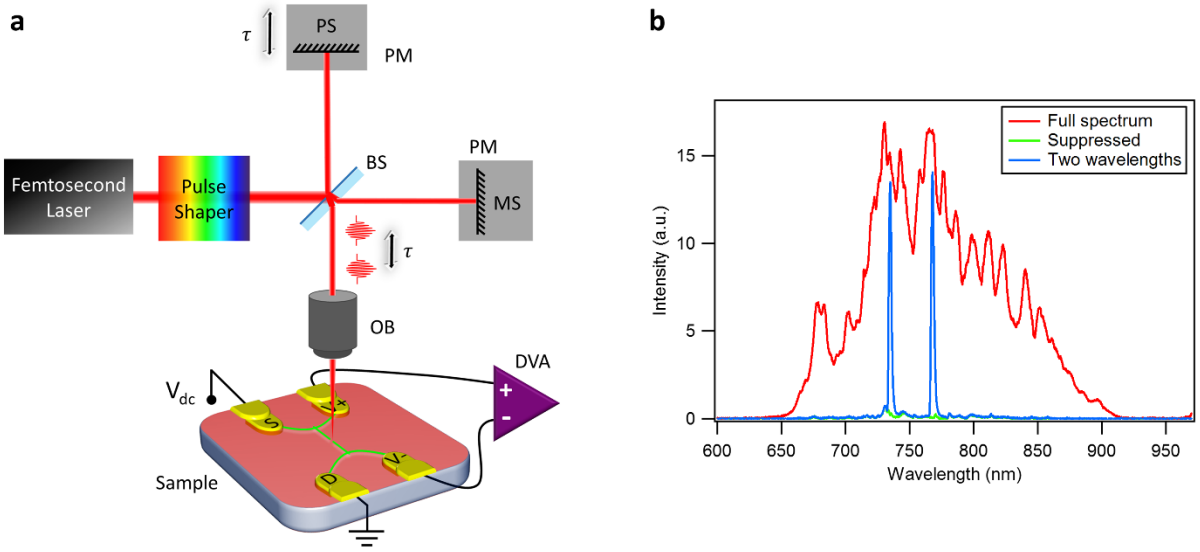

Figure 36 Optical setup and the spectral amplitude control. a Schematic drawing of the optical setup. BS: beam splitter, PM: plane mirror, MS: mechanical stage, PS: piezoelectric stage, OB: objective, DVA: differential voltage amplifier. The dimensions here are not to scale. **b** Spectral amplitude control of the femtosecond optical pulse by the pulse shaper.

difference frequencies and fundamental wavelength pairs labeled accordingly. Different curves are distinguished by color, and all plots in Figure 37 share the same color code. A constant background has been subtracted for each curve, which originates from the DC bias voltage as well as from persistent photoconductance by mid-gap states in STO.[81] A beating envelope can be clearly seen in each signal, and the lower half of the envelope has a larger amplitude than the upper half. Power spectra (Figure 37b,c) are calculated from the time-domain signals to reveal the frequency components. Figure 37b shows the frequency of all the 35 selected fundamental wavelength pairs, while Figure 37c displays the 35 resulting selective difference frequencies generated at the LAO/STO nanojunction. For example, a fundamental wavelength pair of 757 nm (396 THz) and 797 nm (376 THz) is selected from the ultrafast pulse by the pulse shaper to generate a narrow-band emission at 20 THz. The corresponding time-domain signal is measured and plotted in Figure 37a (yellow curve), and its power spectrum clearly shows the fundamental wavelength pair (at the arrowheads in Figure 37b) and confirms that a 20 THz difference frequency is generated (indicated in Figure 37c). The measured linewidth of the narrow-band THz generation (~2 THz on average) in this configuration is limited by the spectral resolution of the SLM as well as the total travel range of the optical delay line (1 ps, which corresponds to 1 THz resolution).

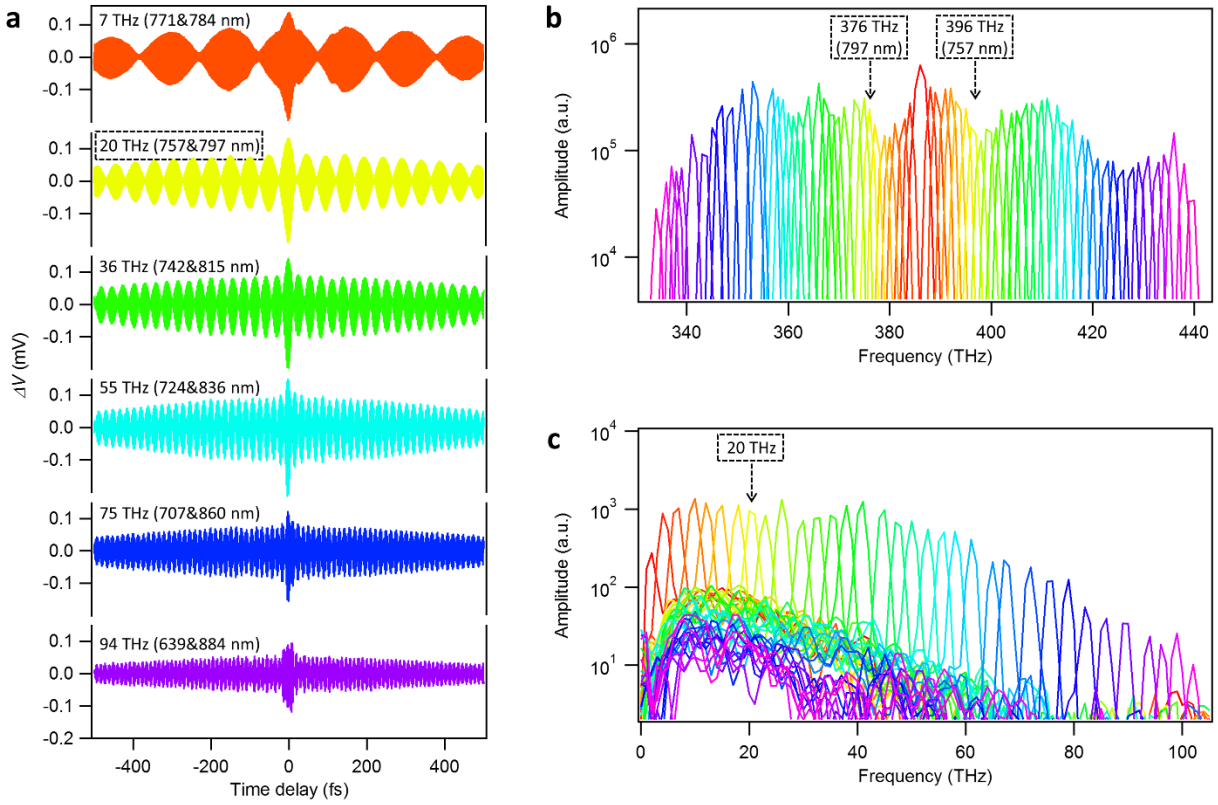

Figure 37 Over 100 THz ultra-broad bandwidth selective difference frequency generation at the LAO/STO nanojunction. a Time-domain signals of six representative difference frequency generations. **b** Power spectra of time-domain signals showing 35 pairs of selected fundamental frequencies. **c** The generated 35 difference frequencies through the third-order nonlinear effect at the nanojunction that spans the entire far- to mid-infrared regime. All plots are color coded.

5.3.2 Theoretical model

Due to the large bandgaps for both LAO and STO, the input photon energies in the experiments are not sufficient to excite valence electrons to the conduction band. Though there are mid-gap states exist in STO,[80] the reported lifetime for STO photo-excited carriers is at least on the order of nanoseconds,[148, 149] which is not relevant for the time scale involved here. On the other hand, the nonlinear optical process (optical rectification) is known to be able to generate a broadband THz field. The experiments are performed at temperature T =80 K. Below T =105 K, bulk STO undergoes a cubic-to-tetragonal transition; however, the STO remains centrosymmetric, with a vanishing second-order susceptibility $\chi^{(2)}$. Even though the breaking of inversion symmetry at the interface of LAO/STO can produce a $\chi^{(2)}$ response,[150, 151] the 2D nature of the interface makes it unlikely for the second-order nonlinear effect to play a dominant role. In contrast, the third-order susceptibility $\chi^{(3)}$ is known to be exceedingly large for bulk STO.[28] It has been experimentally demonstrated that the ultrafast photoconductive response at the LAO/STO nanojunction is DC electric field tunable and spatially confined in the region of the nanojunction.[79] These prior results suggest that the third-order nonlinear effect is the leading mechanism for wave mixing. The nanometer scale dimension (~10 nm) of the nanojunction provides a strong confinement of the DC bias field, resulting in 5.5×10^5 V/cm for V_{dc} = -550 mV. In this sense, the third-order nonlinear process can also be viewed as a DC bias field mediated second-order nonlinear process.

The electric field of the fundamental wavelength pair selected by the pulse shaper can be expressed as

$$E_{input} = E_1 \cos(\omega_1 t) + E_2 \cos(\omega_2 t) \tag{5.1}$$

where E_1 and E_2 are the amplitude, and ω_1 and ω_2 are the angular frequency of the plane wave for the two fundamental wavelengths, respectively. The intensity of this input field E_{input} is then divided equally by a 50/50 ultrafast beam splitter. An additional time delay τ is added to the reflected beam by scanning the piezoelectric stage, compared to the transmitted beam. The electric field for the transmitted beam E_{tran} and the reflected beam E_{refl} are thus given by

$$E_{tran} = \frac{1}{\sqrt{2}}[E_1 \cos(\omega_1 t) + E_2 \cos(\omega_2 t)] \tag{5.2}$$

$$E_{refl} = \frac{1}{\sqrt{2}}(E_1 \cos[\omega_1(t-\tau)] + E_2 \cos[\omega_2(t-\tau)]) \tag{5.3}$$

The two beams are re-combined by the same beam splitter, and focused onto the $LaAlO_3/SrTiO_3$ (LAO/STO) nanojunction, yielding an optical electric field E_{opt} in the following form

$$\begin{aligned} E_{opt} = \frac{1}{2}(&E_1 \cos(\omega_1 t) + E_2 \cos(\omega_2 t) + E_1 \cos[\omega_1(t-\tau)] \\ &+ E_2 \cos[\omega_2(t-\tau)]) \end{aligned} \tag{5.4}$$

A DC bias voltage is applied across the nanojunction, which can be described as a quasi-static local field E_{bias}. The optical field and the bias field interact at the nanojunction, resulting in a change in the polarization *P* in STO:

$$P = \varepsilon_0\left(\chi^{(1)}E_{opt} + \chi^{(3)}E_{bias}^2 E_{opt} + \chi^{(3)}E_{bias}E_{opt}^2 + \chi^{(3)}E_{opt}^3\right) \tag{5.5}$$

where ε_0 is vacuum permittivity, $\chi^{(1)}$ and $\chi^{(3)}$ are the linear and third-order nonlinear susceptibility of STO, respectively. The second-order nonlinear response is neglected, for reasons that are described above. This time-varying polarization generates an induced electric field $E_{induced}$, which offsets the photovoltage across the nanojunction. In addition, the induced field can also mix with the bias field, optical field and itself, further modulating the polarization in STO.

The resulting photo-induced voltage change $\Delta V_{selected}(\tau)$ at the nanojunction for the selected wavelength pair thus takes the form

$$\begin{aligned}\Delta V_{selected}(\tau) \sim\ & E_{induced} + \chi^{(1)}E_{induced} + \chi^{(3)}E_{bias}^2 E_{induced} \\ & + \chi^{(3)}E_{bias}E_{opt}E_{induced} + \chi^{(3)}E_{bias}E_{induced}^2 \\ & + \chi^{(3)}E_{opt}^2 E_{induced} + \chi^{(3)}E_{opt}E_{induced}^2 + \chi^{(3)}E_{induced}^3\end{aligned} \tag{5.6}$$

We ignore $\left(\chi^{(3)}\right)^3$ terms. And due to the slow sample response time compared to the optical frequencies, terms containing $\omega_1 t$ or $\omega_2 t$ vanish, leading to

$$\begin{aligned}\Delta V_{selected}(\tau) \sim\ & \frac{\chi^{(3)}E_{bias}}{64}\Big(4E_1^2\left[4 + 6\chi^{(3)}E_1^2 + 12\chi^{(3)}E_2^2 + 8\chi^{(3)}E_{bias}^2\right. \\ & + \left(\chi^{(1)}\right)^2\left(4 + 9\chi^{(3)}E_1^2 + 18\chi^{(3)}E_2^2\right) \\ & \left. + 4\chi^{(1)}\left(2 + 3\chi^{(3)}E_1^2 + 6\chi^{(3)}E_2^2 + 2\chi^{(3)}E_{bias}^2\right)\right]\cos(\omega_1\tau) \\ & + 4E_2^2\left[4 + 6\chi^{(3)}E_2^2 + 12\chi^{(3)}E_1^2 + 8\chi^{(3)}E_{bias}^2\right. \\ & + \left(\chi^{(1)}\right)^2\left(4 + 9\chi^{(3)}E_2^2 + 18\chi^{(3)}E_1^2\right) \\ & \left. + 4\chi^{(1)}\left(2 + 3\chi^{(3)}E_2^2 + 6\chi^{(3)}E_1^2 + 2\chi^{(3)}E_{bias}^2\right)\right]\cos(\omega_2\tau) \\ & + 3\left[2 + 4\chi^{(1)} + 3\left(\chi^{(1)}\right)^2\right]\chi^{(3)}[E_1^4\cos(2\omega_1\tau) \\ & + E_2^4\cos(2\omega_2\tau)] \\ & + 12E_1^2E_2^2\left[2 + 4\chi^{(1)} + 3\left(\chi^{(1)}\right)^2\right]\chi^{(3)}(\cos[(\omega_1 - \omega_2)\tau] \\ & + \cos[(\omega_1 + \omega_2)\tau])\Big)\end{aligned} \tag{5.7}$$

The small non-vanishing fundamental pulse background after the pulse shaper also contributes to the measured photo-induced voltage change. We approximate the input pulse shape as a Gaussian:

$$E_{input}^{Pulse}(t) = E_0 e^{-(t/t_p)^2} \cos(\omega_c t) \tag{5.8}$$

Where t_p is the pulse width, E_0 is the amplitude and ω_c is the central angular frequency of the pulse wave. Similarly, the focused pulse optical field at the nanojunction is given by

$$E_{opt}^{pulse} = \frac{E_0}{2}\left(e^{-\left(\frac{t}{t_p}\right)^2}\cos(\omega_c t) + e^{-\left(\frac{t-\tau}{t_p}\right)^2}\cos[\omega_c(t-\tau)]\right) \tag{5.9}$$

Since the material response time is much longer than the pulse duration, an integral of t from $-\infty$ to ∞ is needed to derive the pulse-induced photovoltage change $\Delta V_{pulse}(\tau)$ across the nanojunction:

$$\begin{aligned}\Delta V_{pulse}(\tau) \sim \int_{-\infty}^{\infty} \Big(& E_{induced} + \chi^{(1)} E_{induced} + \chi^{(3)} E_{bias}^2 E_{induced} \\ & + \chi^{(3)} E_{bias} E_{opt}^{pulse} E_{induced} + \chi^{(3)} E_{bias} E_{induced}^2 \\ & + \chi^{(3)} \left(E_{opt}^{pulse}\right)^2 E_{induced} + \chi^{(3)} E_{opt}^{pulse} E_{induced}^2 \\ & + \chi^{(3)} E_{induced}^3 \Big) dt\end{aligned} \tag{5.10}$$

Ignore $\left(\chi^{(3)}\right)^3$ and higher order terms. Terms containing $e^{-(\omega_c t_p)^2}$ can also be ignored owing to their extreme small values ($-\left(\omega_c t_p\right)^2 \cong -590$). The computed $\Delta V_{pulse}(\tau)$ then reads

$$\begin{aligned}\Delta V_{pulse}(\tau) \sim \frac{\chi^{(3)} E_0^2 E_{bias}}{128} t_p \sqrt{\pi} \Bigg(\Bigg(& 12E_0^2\left[2 + \chi^{(1)}\left(4 + 3\chi^{(1)}\right)\right]\chi^{(3)} e^{-\frac{3}{4}\left(\frac{\tau}{t_p}\right)^2} \\ & + 16\sqrt{2}\left(1 + \chi^{(1)}\right)\left(1 + \chi^{(1)} + 2\chi^{(3)} E_{bias}^2\right) e^{-\frac{1}{2}\left(\frac{\tau}{t_p}\right)^2} \Bigg) \cos(\omega_c \tau) \\ & + 3E_0^2\left[2 + \chi^{(1)}\left(4 + 3\chi^{(1)}\right)\right]\chi^{(3)} e^{-\left(\frac{\tau}{t_p}\right)^2}\left[2 + \cos(2\omega_c \tau)\right] \Bigg)\end{aligned} \tag{5.11}$$

The measured photo-induced voltage change $\Delta V(\tau)$ across the LAO/STO nanojunction is the sum of both $\Delta V_{selected}(\tau)$ and $\Delta V_{pulse}(\tau)$:

$$\Delta V(\tau) = \Delta V_{selected}(\tau) + \Delta V_{pulse}(\tau) \tag{5.12}$$

For simplicity, we further assume $E_2 \cong E_1$, and rewrite Eq. (5.7) and Eq. (5.11) into

$$\begin{aligned}\Delta V(\tau) \sim a\Bigg(& [\cos(\omega_1\tau) + \cos(\omega_2\tau)] \\ & + b[\cos(2\omega_1\tau) + \cos(2\omega_2\tau) \\ & + 4(\cos[(\omega_1 - \omega_2)\tau] + \cos[(\omega_1 + \omega_2)\tau])] + [ce^{-\frac{1}{2}\left(\frac{\tau}{t_p}\right)^2} \\ & + 4\,d\,e^{-\frac{3}{4}\left(\frac{\tau}{t_p}\right)^2}]\cos(\omega_c\tau) + de^{-\left(\frac{\tau}{t_p}\right)^2}[2 + \cos(2\omega_c\tau)]\Bigg)\end{aligned} \tag{5.13}$$

using following abbreviations

$$\begin{aligned}a = \frac{1}{16}[4 + 18\chi^{(3)}E_1^2 + 8\chi^{(3)}E_{bias}^2 + \left(\chi^{(1)}\right)^2\left(4 + 27\chi^{(3)}E_1^2\right) + 4\chi^{(1)}(2 + \\ 9\chi^{(3)}E_1^2 + 2\chi^{(3)}E_{bias}^2)]\chi^{(3)}E_1^2E_{bias}\end{aligned} \tag{5.14}$$

$$b = \frac{3}{64a}\left[2 + \chi^{(1)}\left(4 + 3\chi^{(1)}\right)\right]\left(\chi^{(3)}\right)^2E_1^4E_{bias} \tag{5.15}$$

$$c = \frac{1}{8a}t_p\sqrt{2\pi}\left(1 + \chi^{(1)}\right)\left(1 + \chi^{(1)} + 2\chi^{(3)}E_{bias}^2\right)\chi^{(3)}E_0^2E_{bias} \tag{5.16}$$

$$d = \frac{3}{128a}t_p\sqrt{\pi}\left[2 + \chi^{(1)}\left(4 + 3\chi^{(1)}\right)\right]\left(\chi^{(3)}\right)^2E_0^4E_{bias} \tag{5.17}$$

A nonlinear least-squares fit is performed to obtain the initial fitting parameters. The initial values for *a*-*d* and their corresponding standard errors are listed below

Table 2 Initial fitting parameter values and standard errors

	Estimate	Standard Error
a	-0.0000425596	3.46618×10^{-8}
b	0.0128076	0.000221672
c	0.887046	0.0123936
d	0.147767	0.00276426

A slight fine-tuning of *a*-*d* is then performed manually around the initial values to better reproduce the experimental data, and final values used for the simulation in the next section are $a \cong 4.33 \times 10^{-5}$ (V), $b = 0.018$, $c = 1.10$, $d = 0.154$.

5.3.3 Numerical simulation and discussion

The time-varying optical field E_{opt} from ultrafast pulses and the quasi-static bias field E_{bias} from the DC bias voltage interact at the LAO/STO nanojunction, resulting in a change in the polarization in STO. Frequency components ω_1 and ω_2 in the optical fields mix, and the resulting time-varying polarization produces an induced field, which offsets the applied DC electric field, as well as further mix with the bias field, the optical field and even with itself to produce a photo-induced voltage change at the difference frequency $\omega_1 - \omega_2$ at the LAO/STO nanojunction.

To better understand the different contributing components for the THz generation, a numerical simulation of the measured time-domain signal has been performed using Eq.(5.13), and the result is shown in Figure 38. The first term represents the linear response of the two selected frequencies at the LAO/STO nanojunction. The second term corresponds to the frequency

mixing through the third-order nonlinear effect. The third and fourth terms are the induced linear and third-order nonlinear photoconductive response by the pulse at the nanojunction, respectively. These two terms exist because of the small non-vanishing fundamental pulse background (baseline of the blue curve in Figure 36b). In Figure 38, we compare the measured time-domain signal at a difference frequency of 20 THz (yellow curve in Figure 37a) with the numerical simulation. Both the beating envelope and the asymmetry in the upper and lower amplitude of the envelope are reproduced. The overall decay of the signal amplitude is due to the finite width of the two selected fundamental wavelengths. Figure 38b shows a close-up of the measured signal and simulated response near $\tau = 0$, showing good agreement between the two. The unequal amplitudes of the lower and upper envelope are a result of the nonlinear process that produces the THz response. The fast oscillation with beating envelope mostly comes from the superposition of the two fundamental frequencies. Discrepancies between the measured signal and the simulation are most visible at the node (near $\tau = 20$ fs), and are attributed to imperfect alignment of the two beams during the movement of the optical time delay line. In addition to the main non-resonant three-wave mixing process, other responses could also take place. For example, the mid-gap states, which are known to form in STO,[80] could introduce near-resonant structure to the response. Nonetheless, the good agreement between the simulation (fit to Eq. (5.13)) and the experimental data indicates that these responses are unlikely to play a dominant role. The linear dependence of signal amplitude on the bias voltage (as indicated by the theoretical model) has also been confirmed experimentally.[79]

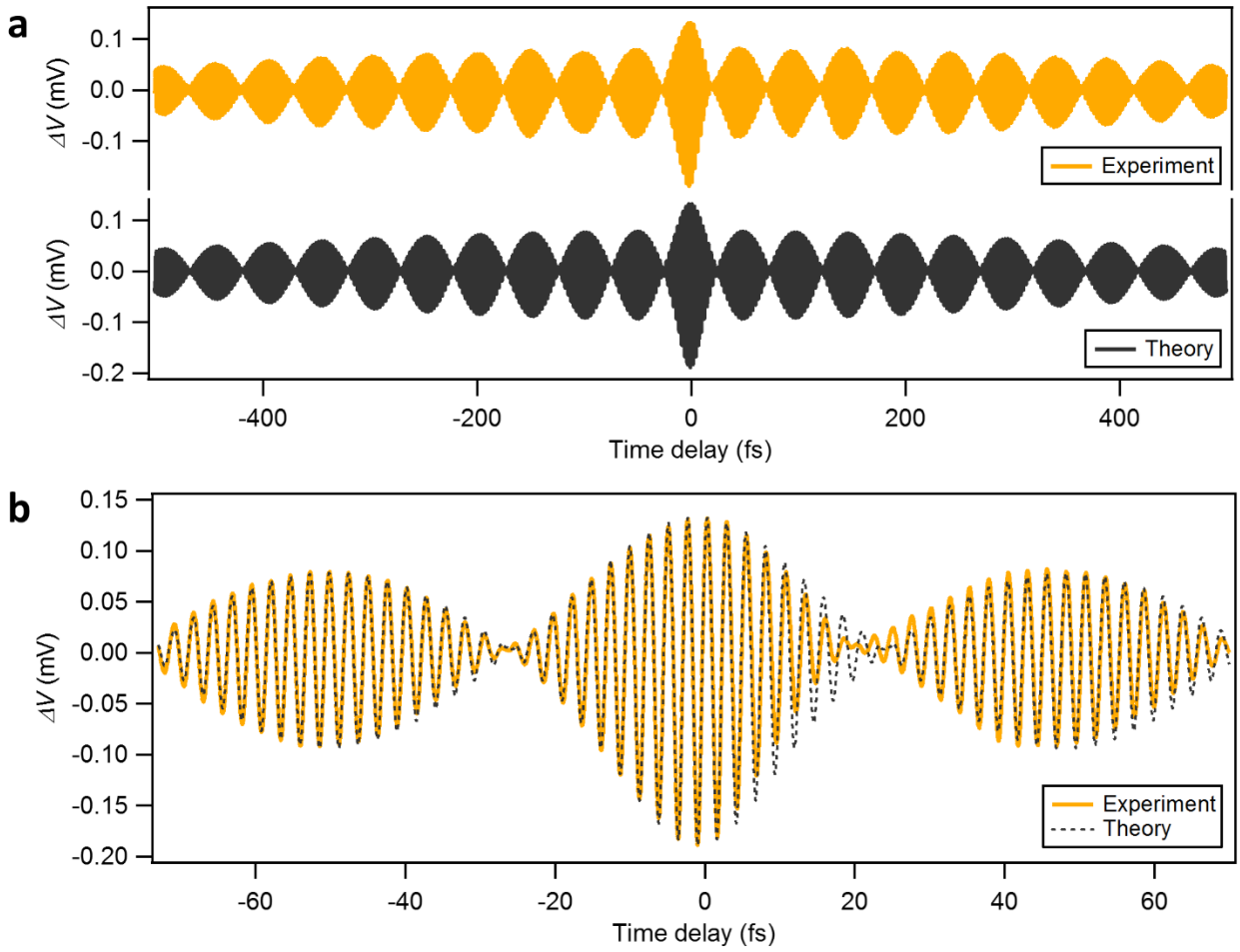

Figure 38 Comparison between the numerical simulation and measured time-domain signal. **a** Both the beating envelope and the asymmetry in the upper and lower amplitude of the envelope are reproduced in the simulation plot. **b** A close-up of the measured and simulated time-domain signal near time delay $\tau = 0$, showing good agreement between the two.

Compared to other existing ultra-broad bandwidth THz sources, such as free-electron lasers,[73] or nonlinear crystals such as GaSe crystals,[152] the LAO/STO nanojunctions are easy to fabricate and reconfigurable, and do not rely on phase matching due to the extremely small dimension of the device. Here, the bandwidth of the THz emission is not restricted by the material, but rather limited only by the spectral bandwidth of the ultrafast pulses. Moreover, a high spatial resolution comes naturally with the LAO/STO nanojunctions. By simply drop-casting the target nanoscale objects onto LAO/STO surface, and creating a nanojunction in the vicinity of a single particle or molecule, individual nanoscale objects can be addressed independently, offering insights that would otherwise be inaccessible from averaging over the ensemble. Spatial mapping of arbitrary substrates is also possible by scanning an LAO/STO nanojunction device in close proximity to the sample (or the other way around). Variations on the sample surface lead to modifications in the interaction among different fields at the nanojunction, which can be reflected by the measured photo-induced voltage change, with a spatial resolution determined by the nanojunction size. In this work, we only control the amplitude of the input ultrafast pulse. Full use of the dual-mask SLM, which can achieve both amplitude and phase modulation, can enable arbitrary shape of the THz waveform for future applications.

5.4 CONCLUSIONS

In conclusion, we have demonstrated over 100 THz bandwidth selective difference frequency generation at LAO/STO nanojunctions that spans the entire far-infrared to mid-infrared regime by femtosecond optical pulse shaping. The ultra-broad tunability, combined with an exceptional spatial precision of 10 nm, shows great promise for exploring fundamental physics in single

nanoscale objects such as quantum dots, nanoparticles or individual molecules. The low optical excitation power imposes minimal heating or other adverse effect on the analyte. The LAO/STO nanojunction serves both as generator and detector of THz emission.[79] By writing two similar nanojunctions adjacent to each other, one can achieve both generation and detection of tunable ultra-broad bandwidth THz fields in a micro-scale area. On the other hand, numerous nanoelectronic devices have already been realized at the LAO/STO interface, such as photodetectors[81] and field-effect transistors.[82] Combining the versatility of the LAO/STO nanodevices with tunable THz functionality further enables a new pathway towards integrated lab-on-chip optoelectronic devices.

6.0 ULTRAFAST OPTICAL RESPONSE OF GRAPHENE/LAO/STO NANOSTRUCTURES

The contents of this chapter represent a collaborative work involving several projects. Section 6.1.1 represents a collaborative work submitted in Li, Hsu, Lee, Tripathi, Guo, Chen, Huang, Dhingra, Lee, Eom, Irvin, Levy and D'Urso, arXiv:1606.08802. Section 6.1.2 represents a collaborative work published in Huang, Jnawali, Hsu, Dhingra, Lee, Ryu, Bi, Ghahari, Ravichandran, Chen, Kim, Eom, D'Urso, Irvin and Levy, *APL Materials* **3**, 062502 (2015). Section 6.2 and 6.3 discuss some preliminary results of an on-going study of the ultrafast optical response of graphene/LAO/STO nanostructures.

Graphene exhibits exceptional electronic and optical properties in the THz regime. For example, plasmons can be induced in graphene by femtosecond pulses, and their resonance frequencies can be gate-tuned over a broad THz range through varying the graphene pattern sizes or gate voltages.[153] Another 2D electron system, the complex-oxide heterostructure LAO/STO, has also shown great promise for control and detection of broadband THz emissions at extreme nanoscale dimensions.[79] Recently, these two platforms have been successfully integrated. A graphene/LAO/STO structure with a high mobility in the graphene channel[154, 155] and oxide nanostructures directly underneath the graphene layer has been created[156]. Here, efforts to probe ultrafast optical responses of graphene in the THz regime using nanoscale THz spectrometer at the LAO/STO interface are discussed.

6.1 GRAPHENE/LAO/STO HETEROSTRUCTURE

6.1.1 Graphene transfer with perfluoropolymers

Chemical vapor deposition (CVD) grown graphene offers large sizes and uniform graphene sheets, making it ideal for a variety of device applications. Commonly used transferring techniques usually involve a polymeric layer, such as poly(methyl methacrylate) (PMMA), which leave residues on or under the graphene sheet. And those hard-to-remove residues act as additional scattering centers, posing a detrimental effect on the electrical properties of graphene, such as limiting its mobility. Recently, a new wet-transferring handle that uses Hyflon instead is reported.[155] A small amount of remnants is observed on the sample surface after transferring, and those remnants can be easily removed with contact mode AFM scans, leading to an atomically clean graphene sheet and a high mobility near the Dirac point at low temperatures.[155]

The high-quality graphene used throughout this chapter is grown by atmospheric pressure CVD on ultra-flat diamond turned copper substrates.[157] Compared to traditional copper foils, ultra-flat copper substrates provide much smoother graphene and larger domain sizes.[157] The as-grown graphene/copper substrate is then spin-coated with a Hyflon buffer layer. Hyflon is a perfluoropolymer. It is hydrophobic and shows a high resistance to solvents or acids, so graphene remains attached to the Hyflon coat during etching of copper substrate in ammonium persulfate. After rinsed in deionized water, the Hyflon/graphene layer is transferred onto the LAO/STO substrate, followed by spin-coating photoresist for the subsequent standard photolithography to define graphene patterns. The photoresist is later removed by acetone, and the Hyflon buffer layer is finally dissolved in FC-40, leaving only patterned graphene on LAO/STO surface. Figure 39 shows a non-contact mode AFM scan phase image right after the transferring and patterning

procedures. A Hall bar patterned graphene sheet can be clearly seen as the light grey contrast compared to the darker grey LAO/STO surface. Only a small amount of Hyflon residues can be seen on the sample surface, and those residues can be further cleaned with simple AFM contact mode scans. The Hyflon buffer layer protects the graphene and LAO/STO surface from directly contacting the photoresist, resulting in very little hard-to-remove contaminations.

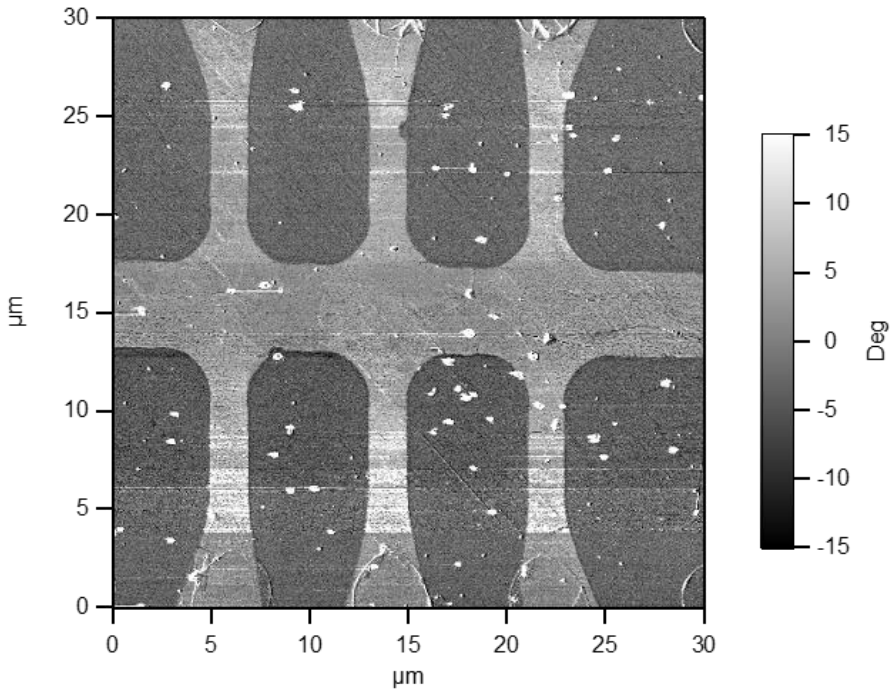

Figure 39 AFM non-contact mode phase image of patterned graphene on LAO/STO surface. The light grey area represents the graphene Hall bar pattern, and the darker grey surroundings are the LAO/STO surface.

6.1.2 c-AFM lithography on graphene/LAO/STO

Since the LAO layer only has a thickness of around 1.2 nm (3.4 unit cells), a strong coupling between the 2D graphene sheet and quasi-2D LAO/STO interface is expected. But in order to probe the ultrafast optical response from this hybrid graphene-complex-oxide heterostructure, an important question of whether the c-AFM lithography still works with graphene on top of the LAO/STO surface needs to be answered first. Recently, the ability to control the metal-insulator transition at the LAO/STO interface underneath single-layer graphene has been reported.[156] Raman spectra taken over areas that have been exposed to the c-AFM lithography show no distinguishable difference compared to the unexposed areas, proving that the graphene quality is not affected by the c-AFM lithography. Interestingly, no conductance jump is observed when writing across multi-layer graphene flakes.[156] It is believed that surface protons can penetrate the single-layer graphene, allowing modulation doping at the LAO/STO interface. However, this process does not work for the multi-layer situation.[158]

Figure 40 shows an example of creating a four-terminal nanostructure in the graphene/LAO/STO heterostructure. Figure 40a displays the designed c-AFM lithography pattern overlaid with a non-contact mode AFM topography image. Green triangles are the virtual electrodes, and pink wires are four-terminal leads. The main channel is represented by the yellow wire, which runs across the graphene sheet. The two-terminal conductance between different electrodes is monitored during the c-AFM lithography. Figure 40b shows that a conductance jump measured between electrode 1 and 4 is observed once the main channel is complete, indicating the nanowire at the LAO/STO interface, which is also partly underneath graphene, is conducting without interruption.

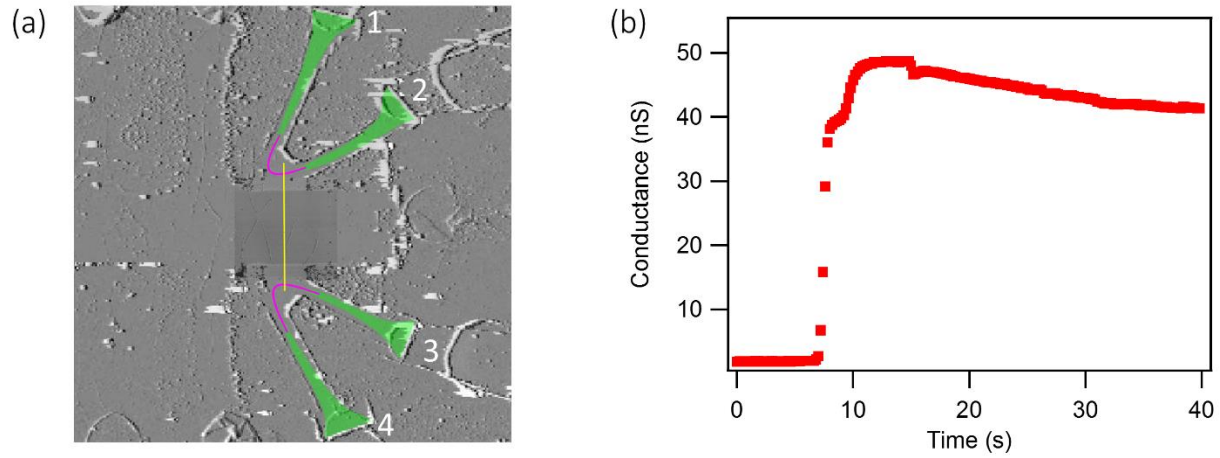

Figure 40 C-AFM lithography on the Graphene/LAO/STO heterostructure. (a) The designed c-AFM lithography pattern overlaid on a non-contact mode AFM topography image of the canvas. Green triangles represent virtual electrodes, while pink wires show the four-terminal leads. The path of the main channel, which is designed across the graphene sheet, is indicated by the yellow wire. (b) Two-terminal conductance monitored between electrode 1 and 4 during the c-AFM lithography. Once the main channel is complete, a conductance jump is observed.

6.2 ULTRAFAST OPTICAL RESPONSE OF GRAPHENE/LAO/STO NANOSTRUCTURES

6.2.1 Experimental approach

To study the ultrafast optical response of graphene/LAO/STO nanostructures, a high-quality single-layer CVD grown graphene flake needs to be transferred onto the LAO/STO substrate and patterned into an ideal shape (for example, a Hall bar). A four-terminal structure is then designed and created by the c-AFM lithography to ensure a nanojunction is located underneath the graphene flake (Figure 41). A planner side gate (*SG*) parallel to the main channel can also be created for applying electric fields to the nanojunction as well as to graphene. After c-AFM lithography, the graphene/LAO/STO sample is transferred to an optical cryostat to study its behavior at low temperatures. Ultrafast pulses are focused on the nanojunction, with a controlled time delay between adjacent pulses. A DC bias voltage is applied between the source (*S*) and drain (*D*) electrodes to provide the initial field offset across the nanojunction. Ultrafast optical responses can then be monitored by measuring the photo-induced voltage change $\Delta V = V_+ - V_-$ as a function of time delay τ. The tunability of the ultrafast optical response can also be studied by applying different gate voltage combinations to the top-gate (*TG*), which is connected to the graphene sheet directly, *SG* and/or back gate (*BG*).

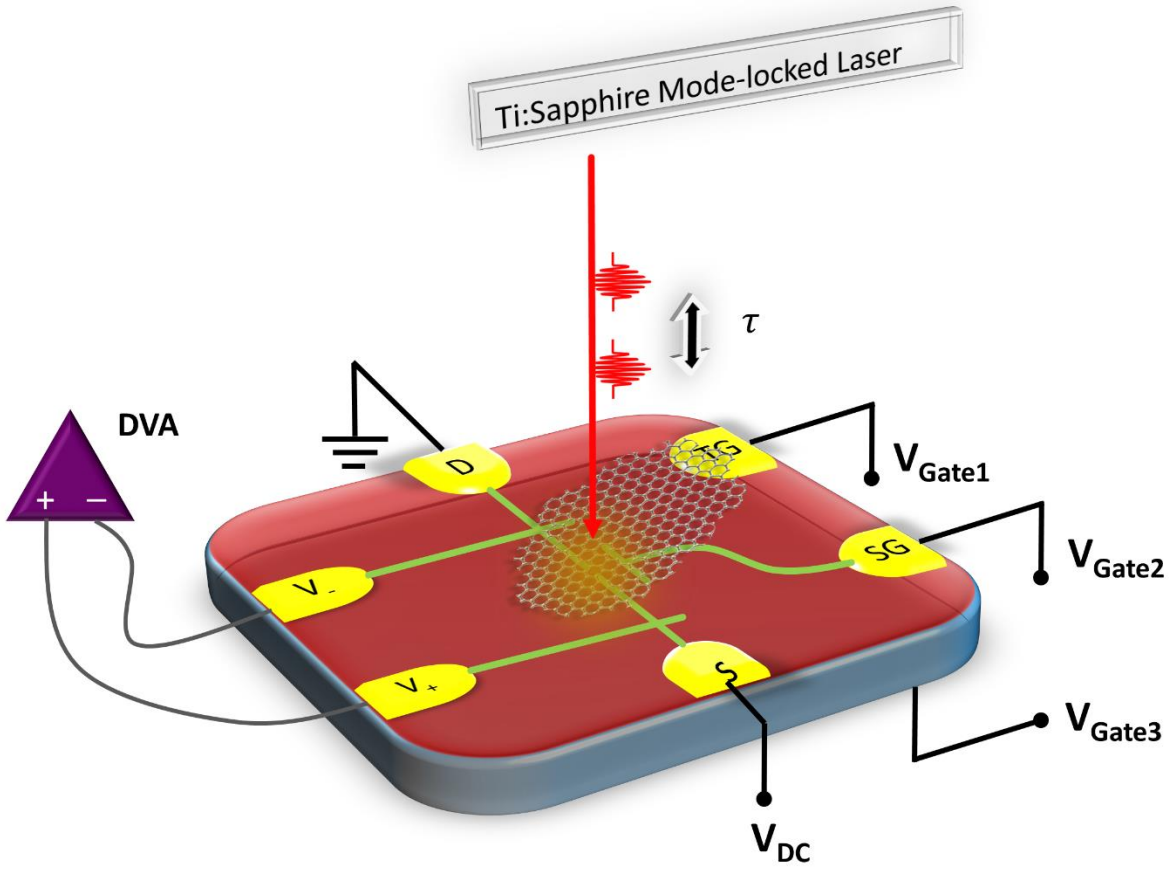

Figure 41 Experimental approach to studying ultrafast optical responses of graphene/LAO/STO nanostructures. DVA: differential voltage amplifier, SG: side gate, TG: top-gate, S: source, D: drain, V_+ and V_- are voltage sensing electrodes, V_{Gate3} represents the voltage applied to the back gate, and τ is the time delay between two adjacent ultrafast pulses.

6.2.2 Preliminary results

An optical reflection scan is taken first to locate the canvas. In Figure 42, the dark blue "fingers" pointing toward the center are 16 gold electrodes. Eight of them are surface electrodes that connect to the graphene sheet, and the other eight electrodes are interface electrodes that are etched through the LAO layer to form a direct contact to the LAO/STO interface. The graphene Hall bar can be barely seen in this image due to its low reflectance, so a fake color (light blue) drawing is overlaid here to guide the eye. Red grains are Hyflon residues being pushed to the edge of the c-AFM lithography defined device region.

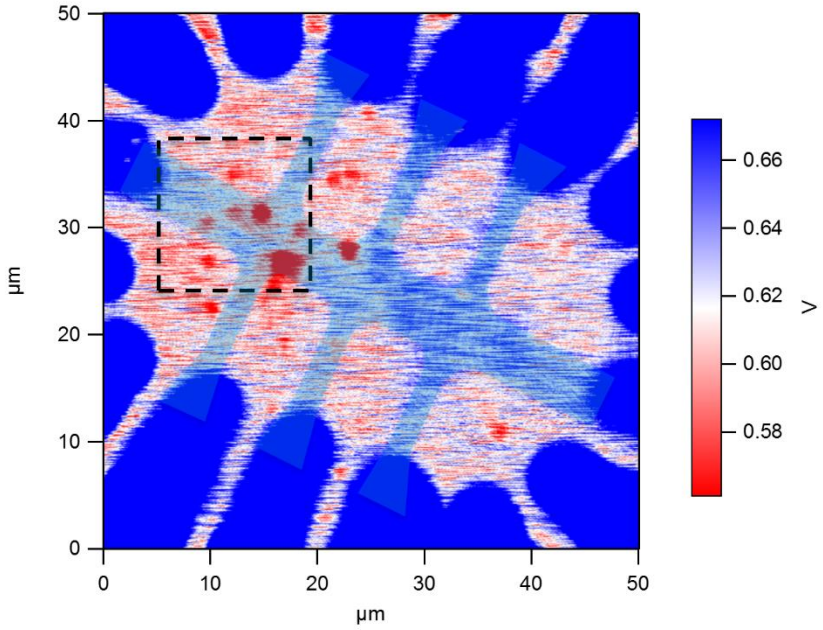

Figure 42 Optical reflection image of the graphene/LAO/STO canvas.

The four-terminal nanojunction structure is exhibited in Figure 43a. The background is a close-up of the reflection scan as indicated by the black dashed box in Figure 42. The main channel is created in three steps. First, the upper half of the curved wire is written from top to bottom, then the lower half is written in the opposite direction. There is a 10 nm gap between the ends of the two wires. After finishing the second half, a negative voltage is applied to the AFM tip and the tip is touched down gently to reaffirm the nanojunction. After the sample is cooled to 80 K, a bias voltage of -400 mV is applied to the *S* electrode, and an input laser power around 20 μW is focused onto the sample through a 100x objective (numerical aperture 0.73). Figure 43b shows the photovoltage scan that is taken simultaneously with the reflection scan in Figure 43a, confirming a nanojunction exists at the LAO/STO interface underneath graphene. Such photovoltage can be tuned by applying different top-gate voltages on graphene as shown in Figure 44. The light remains focused on the nanojunction, and the top-gate voltage is swept from 0 V to positive voltages, followed by negative voltages and then back to 0 V (Figure 44a). As a result, the photovoltage increases first, maximized at the largest top-gate voltage, followed by a decrease with decreasing top-gate voltages, then increases almost back to the initial value when the top-gate is swept back to 0 V. In Figure 44b, a square wave (1 Hz with the peak amplitude $V_p = 0.8$ V) top-gate voltage is applied on graphene, and the simultaneously monitored photovoltage jumps and drops accordingly. A fast rising (falling) time followed by a slow decay (recover) of the photovoltage is observed.

Ultrafast optical responses of graphene/LAO/STO nanostructures have also been studied. The preliminary results show additional oscillations in the THz time-domain signal that possibly originate from the graphene sheet. The bias voltage in this configuration is -500 mV and the input laser power is around 80 μW. In Figure 45a, the photovoltage ΔV is plotted as a function of time

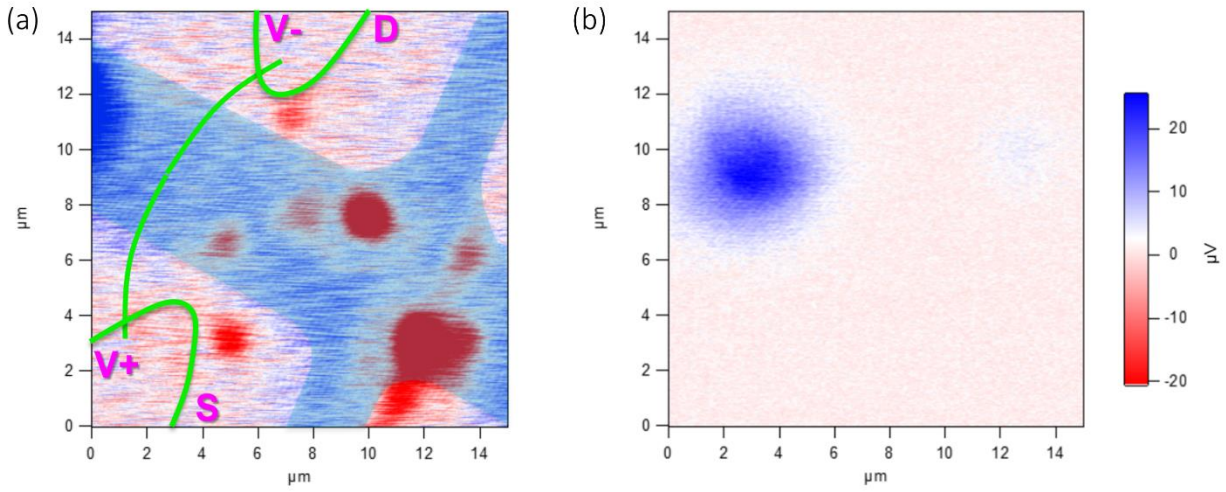

Figure 43 The designed four-terminal nanojunction device across graphene and the measured photovoltage scan. (a) The designed four-terminal nanojunction geometry overlaid on an optical reflection scan of the graphene/LAO/STO canvas. The source (*S*), drain (*D*), and voltage sensing electrodes (*V*+ and *V*-) are labeled accordingly. A nanojunction is located in the middle of the main channel (curved green wire), which is directly underneath the graphene sheet. Note that all the conducting nanostructures are buried at the interface of LAO/STO. (b) The photovoltage scan that is taken simultaneously with the reflection scan in (a). The photo-induced voltage change, which is monitored as $\Delta V = V_+ - V_-$, shows that a nanojunction is created at the interface of LAO/STO and its location matches the designed c-AFM lithography path.

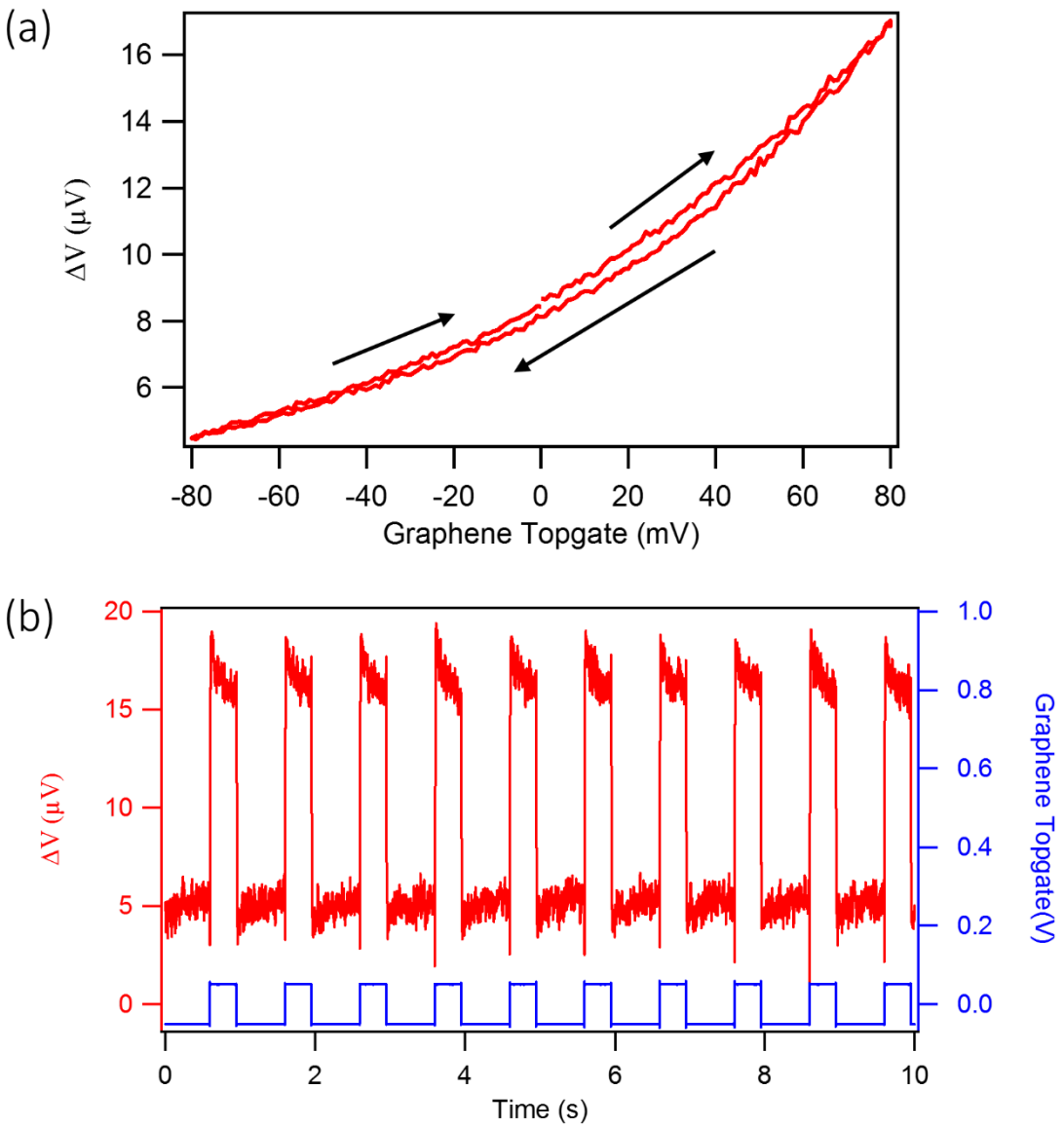

Figure 44 Graphene gate tunable photovoltage across the nanojunction. (a) Tuning the photovoltage ΔV by sweeping the top-gate on graphene. (b) The simultaneously monitored photovoltage ΔV change (red) when a square wave voltage is applied to the top-gate (blue).

delay τ under different configurations. Each curve is an average of 30 consecutive scans. The grey curve is taken from a clean LAO/STO sample without graphene, which shows a standard dip response around $\tau = 0$ with shoulder-like structures coming from the laser itself. The colored curves are from the graphene/LAO/STO sample with 5 different top-gate voltages on graphene. Additional oscillations from the graphene sample can be clearly seen, which have a frequency around 55 THz, as shown in the corresponding power spectra (broad peaks in color curves in Figure 45b). The sharp peaks at 40 THz in Figure 45b are due to the vibrational noise from the cryostat. Both plots here are normalized and shifted for clarity.

6.2.3 Possible physical mechanism

For the additional oscillation around 50-60 THz observed from the graphene/LAO/STO sample, it is still unclear what is the physical origin. However, there are two directions, in particular, that might be worth further looking into.

A single layer defect-free graphene sheet usually exhibits a G peak around 1600 cm^{-1} and a 2D peak around 2600 cm^{-1} in the Raman spectrum.[156] The G peak is due to the doubly degenerate zoon center E_{2g} phonon mode. Converting the wavenumber of G peak to frequency yields 48 THz. So it is possible that the additional oscillation corresponds to a specific phonon mode in graphene. The reason that there is no peak observed in the Raman spectrum that corresponds to a frequency in the range of 50-60 THz might be attributed to the fact that the THz measurements here are done at a spatial confinement of 10 nm×10 nm, so the ultrafast response of graphene is very local. While for the Raman spectrum, the signal is averaged over a large laser spot size that is usually at least on the order of a few hundreds of nanometers.

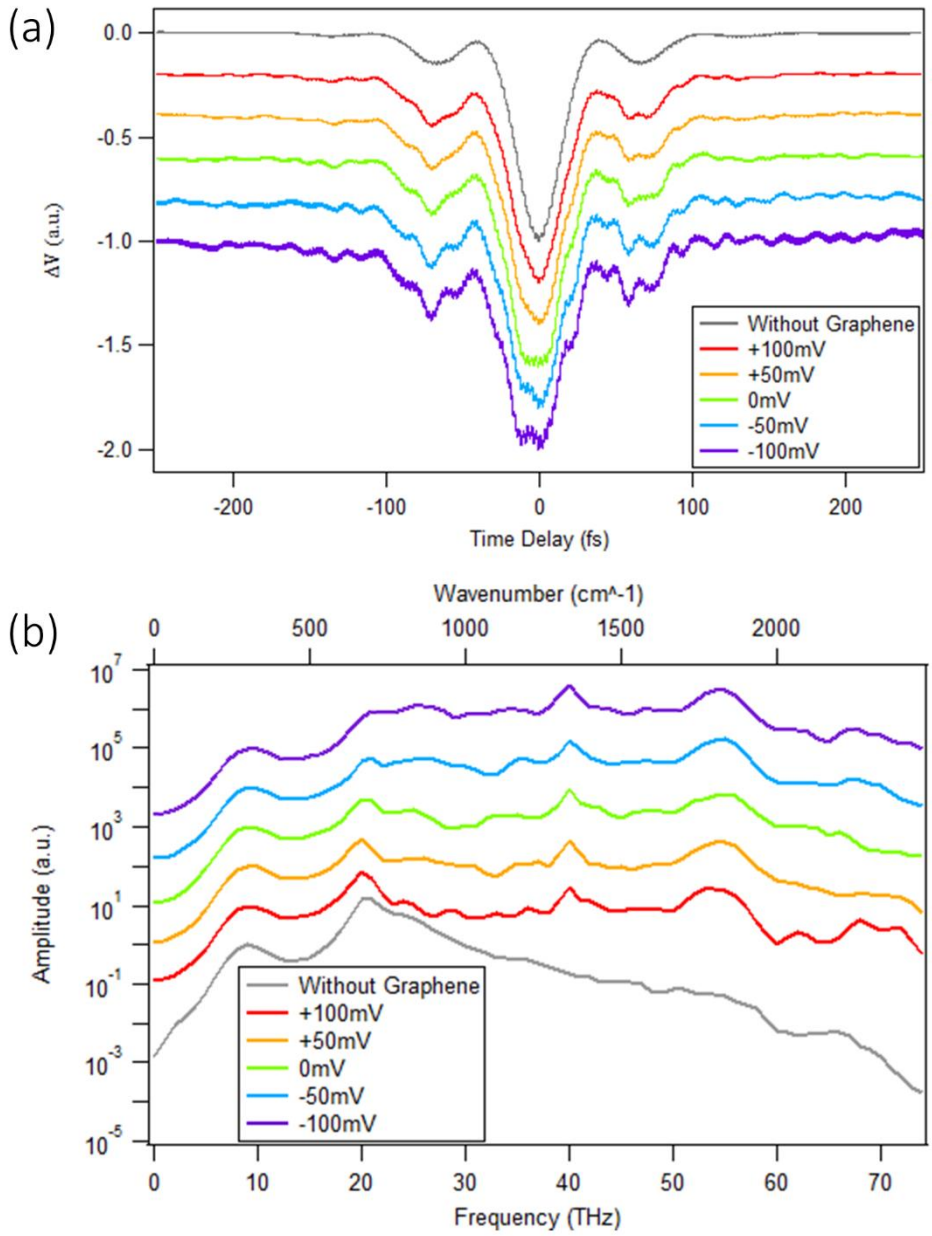

Figure 45 Ultrafast optical responses of graphene/LAO/STO nanostructures. (a) The THz time-domain signal, which measures ΔV as a function of the time delay. The grey curve is from a clean LAO/STO sample without graphene, while colored curves come from the graphene/LAO/STO sample with different top-gate voltages on graphene. (b) Power spectra of signals in (a) show additional peaks around 50-60 THz for the graphene/LAO/STO sample.

Another possible origin of the additional oscillation could be the graphene plasmon resonances. Plasmons can be induced in graphene by femtosecond laser excitations.[153] It has been discussed previously in Chapter 4 that plasmonic response can couple with the induced THz emission at the LAO/STO nanojunctions and modify the measured time-domain signal.

6.3 FUTURE DIRECTIONS

In order to figure out the physical mechanism for the observed additional oscillations in the graphene/LAO/STO sample, as well as explore other ultrafast optical responses and coupling between the two layers of (quasi-)2D materials, several experiments can be done in the future.

Firstly, the gate dependent THz response, where the graphene is gated through its Dirac point, can reveal information relates to the effect of graphene carrier density and even carrier type on the ultrafast optical response. The gating can be done through several schemes. The simplest case would be back gating. STO has a large dielectric constant at low temperatures, and the small size of conducting nanostructures at the LAO/STO interface further provides electric flux focusing, thus the back gating can be very efficient. Another gating scheme that is more direct involves applying the same offset on both sides of the nanojunction while keeping the bias voltage across the nanojunction unchanged. This can be referred to as the interface gating. Since the LAO/STO interface is only 1.2 nm away from graphene, interface gating requires even smaller voltage to tune the graphene across its Dirac point. Both schemes mentioned so far can offer a gate-dependent THz response, but with the price of changing the property of the nanojunction itself at the same time. To accommodate this side effect, a separate side gate can be created when writing the nanostructure, as shown in Figure 41. The combination of the side gate and back gate and/or

interface gate, in principle, could tune the graphene carrier density while maintaining the properties of the nanojunction.

More exotic patterns can also be created underneath graphene, such as superlattices or structures ensemble metamaterials, which provide further possibility and controllability for the coupling between graphene and the LAO/STO interface.

7.0 SUMMARY AND OUTLOOK

Combining the rich physics in STO-based complex oxide heterostructures with the versatile c-AFM lithography technique has enabled the exploration of electron-electron interactions and other emergent properties in these strongly correlated systems at reduced dimensionalities. A vast variety of nanodevices with different functionalities have also been developed, making the STO-based complex oxide heterostructure continued to be a promising candidate for next-generation nanoelectronic and nanophotonic devices.

In this dissertation, the c-AFM lithography has been proved to be able to control the metal-insulator transition at the interface of a nonpolar/nonpolar complex oxide heterostructure of CZO/STO, with extreme feature size as small as 1.2 nm at room temperature. The created nanodevices shed light on the electronic structure of the CZO/STO interface through transport measurements at low temperatures. This successful demonstration shows great potential in patterning the conductivity in other types of heterostructures by the c-AFM lithography, providing a new way to engineer their own unique properties for more complicated applications. Furthermore, the nanodevices can, in turn, reveal the underlying electronic behavior of the heterostructures that would otherwise be inaccessible.

One interesting future experiment for the CZO/STO sample is to measure the lattice distortion using piezoresponse force microscopy (PFM). It has been shown that the charge accumulation at the interface of LAO/STO leads to a lattice elongation. [159] However, the lattice mismatch between CZO and STO has an opposite sign compared to the mismatch between LAO and STO (+2.67% for CZO/STO and -2.79% for LAO/STO). It is possible that the CZO/STO may exhibit a different carrier-mediated lattice distortion, which can result in very different band

structures compared to the extensively studied LAO/STO system. It would be interesting to measure the electro-mechanical response of the c-AFM lithography written and un-written area of CZO/STO by taking PFM scans.

It has been previously demonstrated that both THz emission and detection can be realized using LAO/STO nanojunctions.[79] In this dissertation, this nanoscale THz source is proved to be able to detect the plasmonic response of a single gold nanorod, with a size of tens of nanometers. The capability of this THz source is further expanded by upgrading the femtosecond laser and adding a home-built pulse shaper to the setup. Over 100 THz selective difference frequency generation has been demonstrated. Besides the already investigated quasi-1D nanorod and the still under investigation quasi-2D graphene, this exceptional control of THz fields has unlimited potential for studying individual nanoscale objects or local responses, as shown in Figure 46. Among the quasi-0D nanoparticles, CdSe/CdS core/shell nanoparticles are of particular interest due to their large two-photon absorption cross-sections. Initial experiments to probe the selective two-photon excitation are already underway.

Another direction that is definitely worth pursuing is to incorporate the MIIPS and arbitrary pulse shaping functionalities in the THz setup. Our pulse shaper has the capability to control both pulse amplitude and phase independently. After compressing the femtosecond pulse back to its transform limited width, a user-defined amplitude and/or phase mask can be applied to the pulse for any given applications, thus maximizing the potential of the nanoscale THz generator and detector at LAO/STO nanojunctions.

The STO-based complex oxide heterostructure is an ideal platform for realizing integrated oxide-based circuits as well. Devices such as photodetectors, THz sources and detectors,

waveguides, and transistors can be created by c-AFM lithography on a single micrometer scale substrate, providing numerous complex functionalities that are only limited by our imagination.

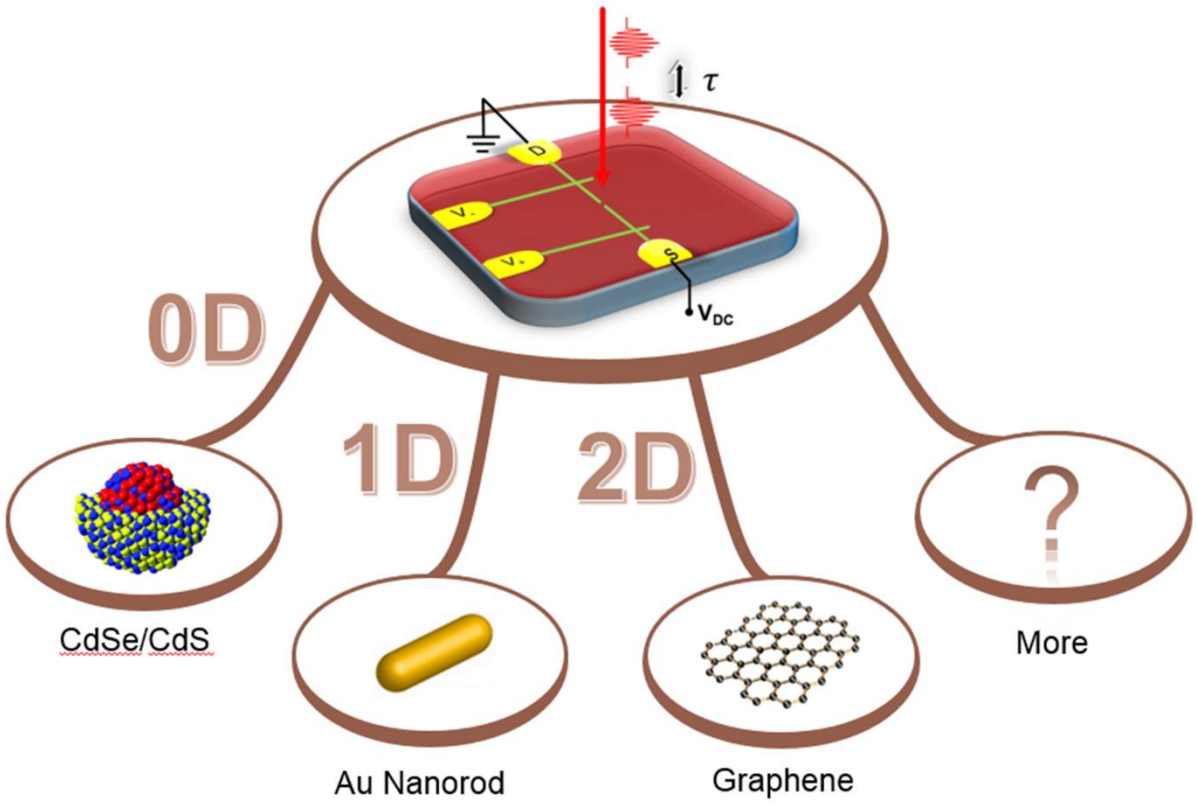

Figure 46 The nanoscale THz platform based on LAO/STO nanojunctions. Materials that be investigated include quasi-0D nanoparticles, quasi-1D nanorods or nanowires, quasi-2D graphene or MoS_2 sheets, and possibly many other materials or systems.

APPENDIX A

SPATIAL LIGHT MODULATOR

A.1 SLM WORKING PRINCIPLE

A.1.1 Birefringence

Anisotropic materials often exhibit birefringence, in which lights with different polarizations and propagation directions experience different refractive indices. This phenomenon was first observed in calcite in 1669. By rotating the calcite crystal on top of a target, a second transmission image may occur and rotate with respect to a fix transmission image. This phenomenon was later explained by the concept of light polarization.

If we describe light as an electromagnetic wave with a propagation direction along the z-axis, then the oscillation direction of the electrical field, which is also called the "polarization", lies in the xy-plane. In principle, any polarization state can be projected to two orthogonal axes. And when the light is incident on a birefringent crystal, these two perpendicular polarizations may experience different refractive indices, thus leaving the crystal with different output trajectory, resulting in two images.

Crystals with non-cubic lattice structures are often birefringent. The simplest case for birefringence is the uniaxial crystal, like calcite. The term "uniaxial" refers to the fact that there is only one direction in this kind of crystal, along which different polarizations propagate with the

same refractive index. This direction is also called the "optical axis" (OA in Figure 47a). For any polarizations perpendicular to the optical axis, the refractive index is termed as the "ordinary refractive index" (n_o). While for polarization along the optical axis, it experiences an "extraordinary refractive index" (n_e). A beam polarized in between has an effective refractive index

$$\frac{1}{n(\theta)^2} = \frac{cos^2(\theta)}{n_o^2} + \frac{sin^2(\theta)}{n_e^2} \tag{A.1}$$

where θ is the angle between the input beam and the optical axis. Note that both n_o and n_o depend on the wavelength as well. Conventionally, if a crystal exhibits $n_o > n_e$, then the crystal is classified as a negative birefringent material. Oppositely, if $n_o < n_e$ then the crystal is a positive birefringent material.

A special configuration is when the optical axis is parallel to the crystal surface, and light is incident normally. In this case, the two orthogonal polarizations still experience different refractive indices, but their propagation directions are the same. For a positive birefringent crystal, the extraordinary beam arrives after the ordinary beam, which means a phase retardation has been introduced to the extraordinary beam. This principle can be used to realize wave plates, in which by varying the thickness of the crystal, certain phase retardation can be specified to change the output polarization state. Figure 47b shows an example of different output polarizations that can be achieved by adding different phase retardations between the two orthogonal polarizations.

A more complicated case for birefringence is the biaxial crystal, which involves three different refractive indices, each along one principal axis. However, there are two unique directions, along which light may propagate without birefringence, hence termed as "biaxial". Mathematical description for a biaxial crystal is much more complicated than the uniaxial case, and we will not go into details here.

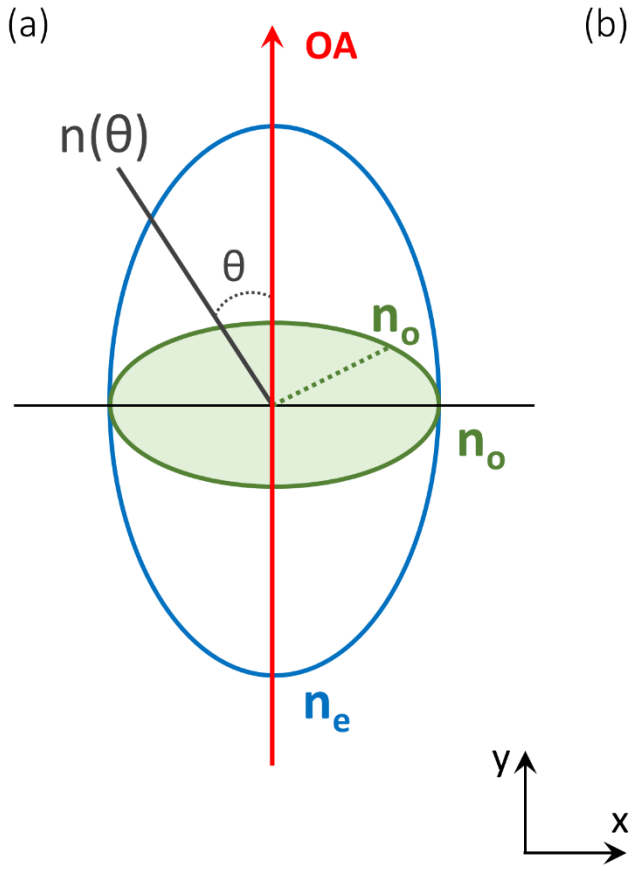

(b)

Phase retardation	Polarization
-180°	
-135°	
-90°	
-45°	
0°	
45°	
90°	
135°	
180°	

Figure 47 Birefringence. (a) Refractive index ellipsoid of a uniaxial positive birefringent crystal. (b) Different polarization states that can be achieved by adding different phase retardations to a linearly polarized input light.

A.1.2 Liquid crystal cells

Besides naturally available crystals, there are various artificial birefringent materials. For example, the liquid crystal cell. As shown in Figure 48, a liquid crystal cell consists of a thin layer of nematic planar liquid crystal that is in between two parallel glass substrates. Transparent electrodes are attached to the inner surface of the glass substrate, on top of which an alignment layer is coated to provide an initial orientation of the nematic liquid crystal molecules. The oval shape of these molecules yields an optical anisotropy in refractive index once they are aligned, with the optical axis parallel to the long axis of the molecules.

At zero bias voltage on the transparent electrodes, no electric field is applied to the molecules, thus they are simply aligned with the alignment layer, as shown in the left image in Figure 48. The optical axis is along the x-axis. Once a bias voltage is applied, the electric field across glass substrates turns the direction of liquid crystal molecules, rotating the optical axis towards the z-axis accordingly. For a normally incident light along the z-axis, this process can be equivalently described as follows: light with polarization along x- and y-axis starts with the maximum phase retardation at zero bias voltage, and as the bias voltage increases, the retardation decreases until all the molecules are aligned parallel to the z-axis. At that time, the induced phase retardation is zero.

The maximum phase retardation a liquid crystal cell can offer depends on both the difference between n_e and n_o (sometimes defined as the birefringence of a material) as well as the total thickness of the liquid crystal layer d

$$\phi_{max} = 2\pi \frac{(n_e - n_o)d}{\lambda} \tag{A.2}$$

where λ is the input light wavelength.

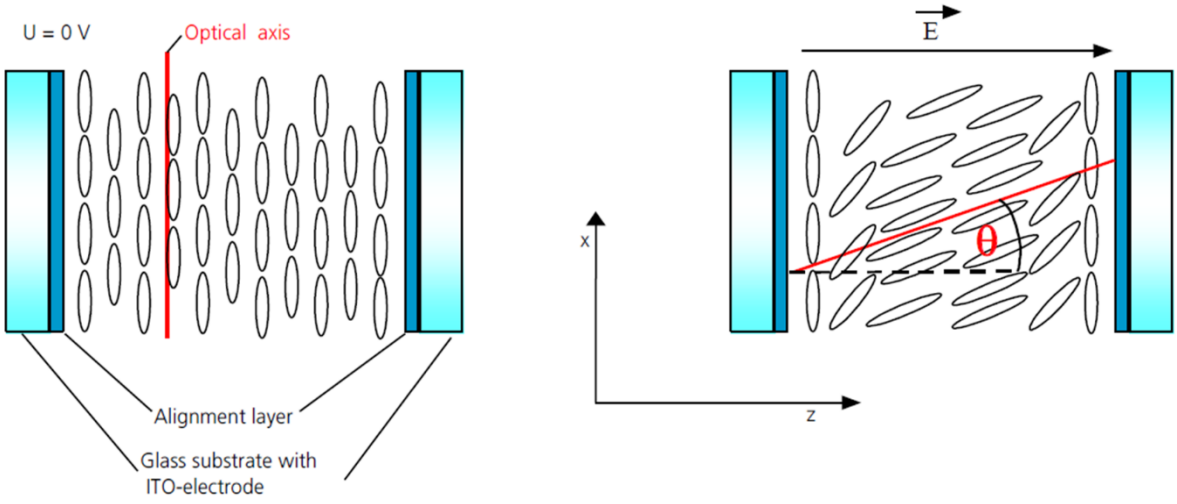

Figure 48 Schematic drawing for the liquid crystal cell and its birefringence. Image adopted from the Jenoptik SLM-S640d manual.

A.1.3 SLM structure

In Chapter 5, a Jenoptik spatial light modulator (SLM-S640d) is used for the femtosecond pulse shaping. This SLM has a dual mask design, with 640 pixels on each mask, for independently controlling the phase and amplitude of different wavelengths in the femtosecond pulse. A layout of one mask is shown in Figure 49a. There are 640 pixels aligned linearly along the x-axis. Each pixel has a size of 97 μm × 10 mm, and they are separated by 3 μm. Then two identical masks are glued back-to-back, with each pixel precisely aligned (Figure 49b). Voltages can be applied separately to each pixel on the individual mask. An optical anti-reflection (AR) coating from 600 nm to 1200 nm is also added to both masks to minimize unwanted multi-reflections.

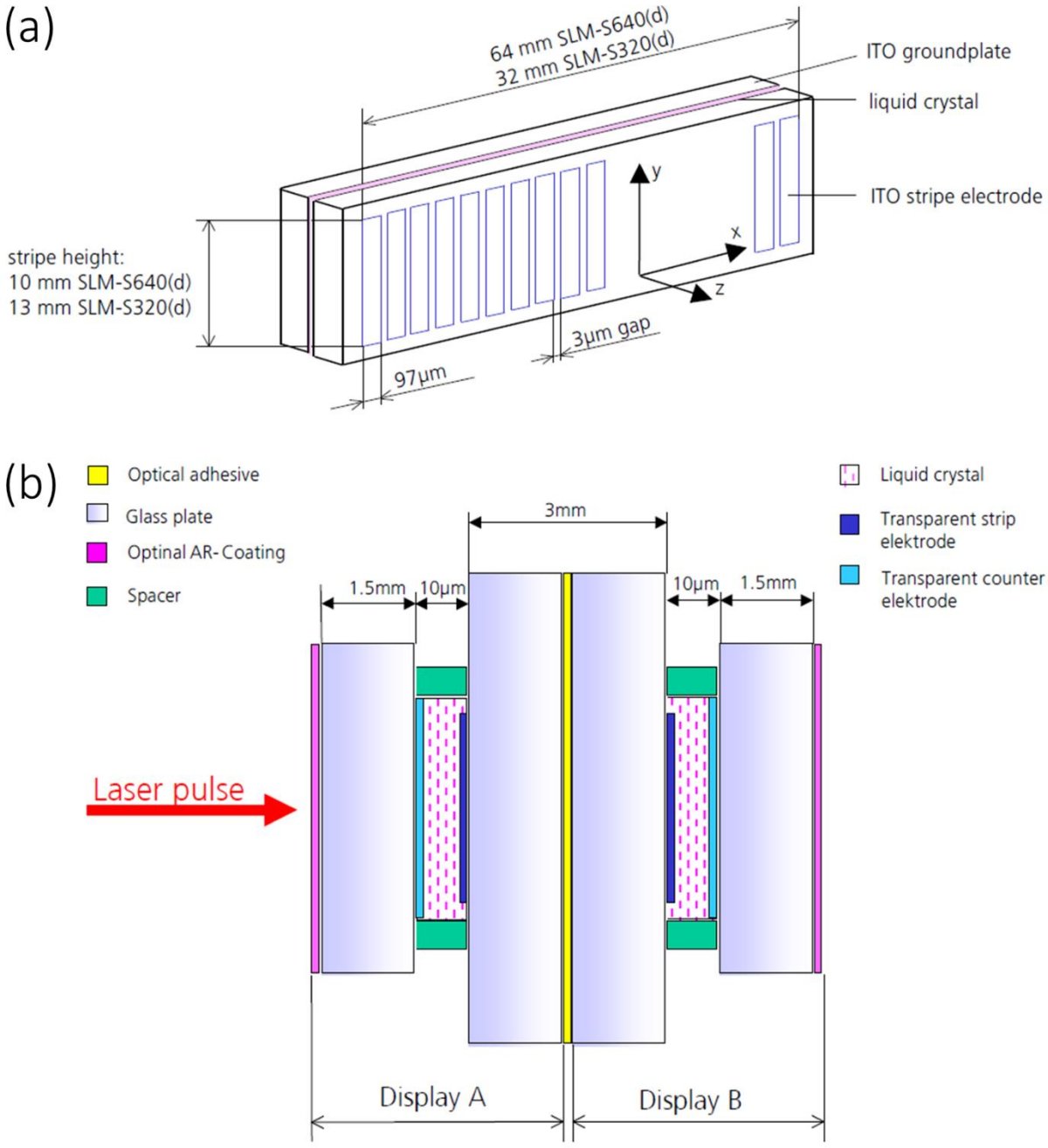

Figure 49 Schematic drawing of Jenoptik SLM-S640d. (a) The layout of the 640 pixels of a single SLM mask. (b) Schematic drawing of the dual mask design, with two SLM masks attached back-to-back. Images adopted from the Jenoptik SLM-S640d manual.

A.2 JONES CALCULUS

Jones calculus can be used to describe the light polarization after different optical components, where light polarization is represented by a Jones vector and each optical element is represented by a Jones matrix. The process of light passing through an optical element is then described by multiply the corresponding Jones matrix to the input light vector. Note that only fully polarized light can be described by the Jones calculus.

If light propagates along the z-axis, then the Jones vector to describe the light polarization is

$$\begin{pmatrix} E_x e^{i\phi_x} \\ E_y e^{i\phi_y} \end{pmatrix} \tag{A.3}$$

For simplicity, the light intensity is usually normalized $E_x^2 + E_y^2 = 1$, and the phase start with 0, which means $e^0 = 1$ and $e^{i\pi/2} = i$. The Jones vectors for most common polarizations are

Table 3 Jones vectors for different polarizations

Polarization	Jones vector
Linear along the x-axis	$\begin{pmatrix} 1 \\ 0 \end{pmatrix}$
Linear along the y-axis	$\begin{pmatrix} 0 \\ 1 \end{pmatrix}$
Linear +45° from the x-axis	$\frac{1}{\sqrt{2}}\begin{pmatrix} 1 \\ 1 \end{pmatrix}$
Linear -45° from the x-axis	$\frac{1}{\sqrt{2}}\begin{pmatrix} 1 \\ -1 \end{pmatrix}$
Right-hand circular	$\frac{1}{\sqrt{2}}\begin{pmatrix} 1 \\ -i \end{pmatrix}$

Left-hand circular	$\frac{1}{\sqrt{2}}\begin{pmatrix}1\\ i\end{pmatrix}$

The Jones matrices for a few commonly used optical elements are

Table 4 Jones matrices for different optical element

Optical element	Jones vector
Linear polarizer along the x-axis	$\begin{pmatrix}1 & 0\\ 0 & 0\end{pmatrix}$
Linear polarizer along the y-axis	$\begin{pmatrix}0 & 0\\ 0 & 1\end{pmatrix}$
Linear polarizer +45° from the x-axis	$\frac{1}{2}\begin{pmatrix}1 & 1\\ 1 & 1\end{pmatrix}$
Linear polarizer -45° from the x-axis	$\frac{1}{2}\begin{pmatrix}1 & -1\\ -1 & 1\end{pmatrix}$
Right-hand circular polarizer	$\frac{1}{2}\begin{pmatrix}1 & i\\ -i & 1\end{pmatrix}$
Left-hand circular polarizer	$\frac{1}{2}\begin{pmatrix}1 & -i\\ i & 1\end{pmatrix}$
Quarter-wave plate with fast axis at θ from the x-axis	$\begin{pmatrix}cos^2\theta + isin^2\theta & (1-i)sin\theta cos\theta\\ (1-i)sin\theta cos\theta & icos^2\theta + sin^2\theta\end{pmatrix}$
Half-wave plate with fast axis at θ from the x-axis	$\begin{pmatrix}cos2\theta & sin2\theta\\ sin2\theta & -cos2\theta\end{pmatrix}$
Arbitrary phase retardation $\Delta\phi$ with fast axis at θ from the x-axis	$\begin{pmatrix}cos^2\theta + e^{i\Delta\phi}sin^2\theta & \left(1-e^{i\Delta\phi}\right)sin\theta cos\theta\\ \left(1-e^{i\Delta\phi}\right)sin\theta cos\theta & e^{i\Delta\phi}cos^2\theta + sin^2\theta\end{pmatrix}$

In our home-built pulse shaper setup, the optical axis of the first mask in the SLM (Display A in Figure 50) is at +45° from the x-axis, while the second mask (Display B) is at -45° from

the x-axis. The SLM works in a reflection mode, which means light gets reflected back after Display B and re-enters Display B and Display A consecutively. The input light has a linear polarization parallel to the x-axis and a linear polarizer that passes the horizontal polarization is placed after the pulse shaper. In this configuration, the output light can be described as

$$
\begin{aligned}
&\overrightarrow{E_{out}} \\
&= \begin{pmatrix} 1 & 0 \\ 0 & 0 \end{pmatrix} \cdot \begin{pmatrix} cos^2\left(\frac{\pi}{4}\right) + e^{i\Delta\phi_A} sin^2\left(\frac{\pi}{4}\right) & \left(1 - e^{i\Delta\phi_A}\right) sin\left(\frac{\pi}{4}\right) cos\left(\frac{\pi}{4}\right) \\ \left(1 - e^{i\Delta\phi_A}\right) sin\left(\frac{\pi}{4}\right) cos\left(\frac{\pi}{4}\right) & e^{i\Delta\phi_A} cos^2\left(\frac{\pi}{4}\right) + sin^2\left(\frac{\pi}{4}\right) \end{pmatrix} \\
&\cdot \begin{pmatrix} cos^2\left(-\frac{\pi}{4}\right) + e^{i\Delta\phi_B} sin^2\left(-\frac{\pi}{4}\right) & \left(1 - e^{i\Delta\phi_B}\right) sin\left(-\frac{\pi}{4}\right) cos\left(-\frac{\pi}{4}\right) \\ \left(1 - e^{i\Delta\phi_B}\right) sin\left(-\frac{\pi}{4}\right) cos\left(-\frac{\pi}{4}\right) & e^{i\Delta\phi_B} cos^2\left(-\frac{\pi}{4}\right) + sin^2\left(-\frac{\pi}{4}\right) \end{pmatrix} \\
&\cdot \begin{pmatrix} cos^2\left(-\frac{\pi}{4}\right) + e^{i\Delta\phi_B} sin^2\left(-\frac{\pi}{4}\right) & \left(1 - e^{i\Delta\phi_B}\right) sin\left(-\frac{\pi}{4}\right) cos\left(-\frac{\pi}{4}\right) \\ \left(1 - e^{i\Delta\phi_B}\right) sin\left(-\frac{\pi}{4}\right) cos\left(-\frac{\pi}{4}\right) & e^{i\Delta\phi_B} cos^2\left(-\frac{\pi}{4}\right) + sin^2\left(-\frac{\pi}{4}\right) \end{pmatrix} \\
&\cdot \begin{pmatrix} cos^2\left(\frac{\pi}{4}\right) + e^{i\Delta\phi_A} sin^2\left(\frac{\pi}{4}\right) & \left(1 - e^{i\Delta\phi_A}\right) sin\left(\frac{\pi}{4}\right) cos\left(\frac{\pi}{4}\right) \\ \left(1 - e^{i\Delta\phi_A}\right) sin\left(\frac{\pi}{4}\right) cos\left(\frac{\pi}{4}\right) & e^{i\Delta\phi_A} cos^2\left(\frac{\pi}{4}\right) + sin^2\left(\frac{\pi}{4}\right) \end{pmatrix} \cdot \begin{pmatrix} 1 \\ 0 \end{pmatrix} \\
&= \frac{1}{2}\left(e^{i2\Delta\phi_A} + e^{i2\Delta\phi_B}\right) \cdot \begin{pmatrix} 1 \\ 0 \end{pmatrix}
\end{aligned}
\tag{A.4}
$$

The output can be further rewritten into

$$\cos(\Delta\phi_A - \Delta\phi_B)\, e^{i(\Delta\phi_A + \Delta\phi_B)} \cdot \begin{pmatrix} 1 \\ 0 \end{pmatrix} \tag{A.5}$$

with the amplitude A and phase ϕ of the output light expressed as

$$A = \cos(\Delta\phi_A - \Delta\phi_B) \tag{A.6}$$

$$\phi = \Delta\phi_A + \Delta\phi_B \tag{A.7}$$

By controlling the phase retardation in mask A and mask B, both amplitude and phase of the output beam can be controlled. In addition, pure amplitude (or phase) modulation can be achieved by changing both $\Delta\phi_A$ and $\Delta\phi_B$ in a way that $\Delta\phi_A + \Delta\phi_B = constant$ (or $\Delta\phi_A - \Delta\phi_B = constant$). Writing out the phase retardation for each mask specifically yields

$$\phi_A = \frac{1}{2}\left(\phi + acrcos(A)\right) \tag{A.8}$$

$$\phi_B = \frac{1}{2}\left(\phi - acrcos(A)\right) \tag{A.9}$$

Note that what is actually being measured experimentally is the intensity of the output light $I = A^2$.

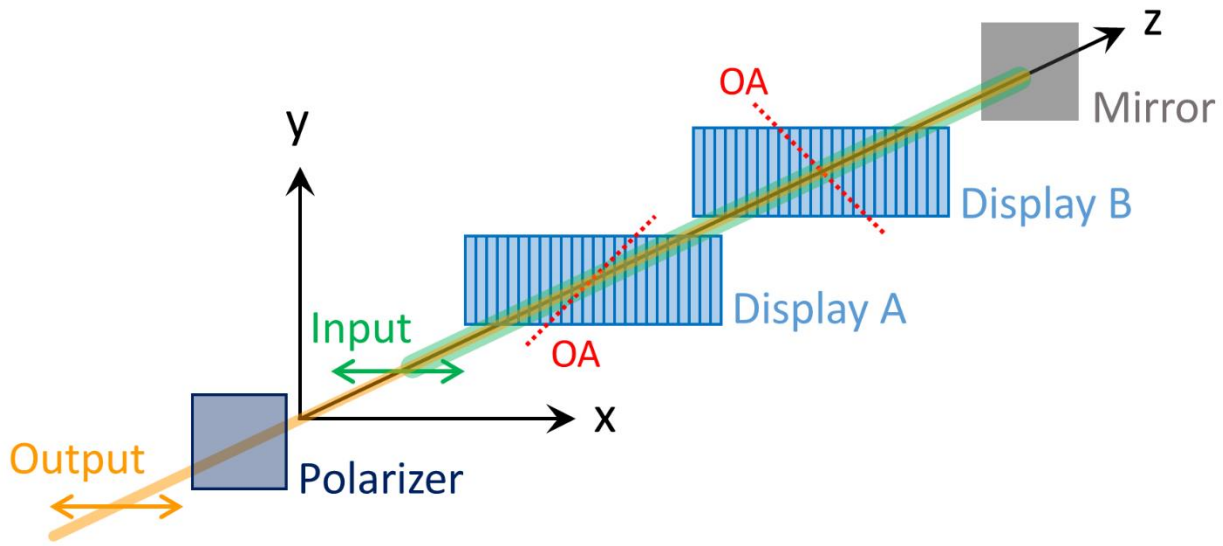

Figure 50 Schematic drawing for a horizontally polarized input light passing through two SLM masks and a horizontal polarizer.

BIBLIOGRAPHY

[1] F. El-Mellouhi, E. N. Brothers, M. J. Lucero, and G. E. Scuseria, Modeling of the cubic and antiferrodistortive phases of $SrTiO_3$ with screened hybrid density functional theory, *Physical Review B* **84**, 115122 (2011).

[2] K. van Benthem, C. Elsässer, and R. H. French, Bulk electronic structure of $SrTiO_3$: Experiment and theory, *Journal of Applied Physics* **90**, 6156 (2001).

[3] H. Noad, E. M. Spanton, K. C. Nowack, H. Inoue, M. Kim, T. A. Merz, C. Bell, Y. Hikita, R. Xu, W. Liu, A. Vailionis, H. Y. Hwang, and K. A. Moler, Variation in superconducting transition temperature due to tetragonal domains in two-dimensionally doped $SrTiO_3$, *Physical Review B* **94**, 174516 (2016).

[4] G. Cheng, A. Annadi, S. Lu, H. Lee, J.-W. Lee, M. Huang, C.-B. Eom, P. Irvin, and J. Levy, Shubnikov-de Haas-like Quantum Oscillations in Artificial One-Dimensional $LaAlO_3/SrTiO_3$ Electron Channels, *Physical Review Letters* **120**, 076801 (2018).

[5] Y.-Y. Pai, H. Lee, J.-W. Lee, A. Annadi, G. Cheng, S. Lu, M. Tomczyk, M. Huang, C.-B. Eom, P. Irvin, and J. Levy, One-Dimensional Nature of Superconductivity at the $LaAlO_3/SrTiO_3$ Interface, *Physical Review Letters* **120**, 147001 (2018).

[6] B. Kalisky, E. M. Spanton, H. Noad, J. R. Kirtley, K. C. Nowack, C. Bell, H. K. Sato, M. Hosoda, Y. Xie, Y. Hikita, C. Woltmann, G. Pfanzelt, R. Jany, C. Richter, H. Y. Hwang, J. Mannhart, and K. A. Moler, Locally enhanced conductivity due to the tetragonal domain structure in $LaAlO_3/SrTiO_3$ heterointerfaces, *Nature Materials* **12**, 1091 (2013).

[7] K. A. Muller and H. Burkard, $SrTiO_3$ - Intrinsic quantum paraelectric below 4 K, *Physical Review B* **19**, 3593 (1979).

[8] J. H. Haeni, P. Irvin, W. Chang, R. Uecker, P. Reiche, Y. L. Li, S. Choudhury, W. Tian, M. E. Hawley, B. Craigo, A. K. Tagantsev, X. Q. Pan, S. K. Streiffer, L. Q. Chen, S. W. Kirchoefer, J. Levy, and D. G. Schlom, Room-temperature ferroelectricity in strained $SrTiO_3$, *Nature* **430**, 758 (2004).

[9] D. Rytz, U. T. Höchli, and H. Bilz, Dielectric susceptibility in quantum ferroelectrics, *Physical Review B* **22**, 359 (1980).

[10] R. C. Neville, B. Hoeneisen, and C. A. Mead, Permittivity of Strontium Titanate, *Journal of Applied Physics* **43**, 2124 (1972).

[11] T. Sakudo and H. Unoki, Dielectric Properties of $SrTiO_3$ at Low Temperatures, *Physical Review Letters* **26**, 851 (1971).

[12] J. Hemberger, P. Lunkenheimer, R. Viana, R. Bohmer, and A. Loidl, Electric-Field-Dependent Dielectric-Constant and Nonlinear Susceptibility in $SrTiO_3$, *Physical Review B* **52**, 13159 (1995).

[13] T. Mitsui and W. B. Westphal, Dielectric and X-Ray Studies of $Ca_xBa_{1-x}TiO_3$ and $Ca_xSr_{1-x}TiO_3$, *Physical Review* **124**, 1354 (1961).

[14] Y. S. Kim, J. Kim, S. J. Moon, W. S. Choi, Y. J. Chang, J. G. Yoon, J. Yu, J. S. Chung, and T. W. Noh, Localized electronic states induced by defects and possible origin of ferroelectricity in strontium titanate thin films, *Applied Physics Letters* **94**, 202906 (2009).

[15] K. Shirai and K. Yamanaka, Mechanism behind the high thermoelectric power factor of $SrTiO_3$ by calculating the transport coefficients, *Journal of Applied Physics* **113**, 053705 (2013).

[16] S. Piskunov, E. Heifets, R. I. Eglitis, and G. Borstel, Bulk properties and electronic structure of $SrTiO_3$, $BaTiO_3$, $PbTiO_3$ perovskites: an ab initio HF/DFT study, *Computational Materials Science* **29**, 165 (2004).

[17] Y. Kim, R. M. Lutchyn, and C. Nayak, Origin and transport signatures of spin-orbit interactions in one- and two-dimensional $SrTiO_3$-based heterostructures, *Physical Review B* **87**, 245121 (2013).

[18] A. Annadi, G. Cheng, H. Lee, J.-W. Lee, S. Lu, A. Tylan-Tyler, M. Briggeman, M. Tomczyk, M. Huang, D. Pekker, C.-B. Eom, P. Irvin, and J. Levy, Quantized Ballistic Transport of Electrons and Electron Pairs in $LaAlO_3/SrTiO_3$ Nanowires, *Nano Letters* **18**, 4473 (2018).

[19] Y. J. Chang, G. Khalsa, L. Moreschini, A. L. Walter, A. Bostwick, K. Horn, A. H. MacDonald, and E. Rotenberg, Uniaxial strain induced band splitting in semiconducting $SrTiO_3$, *Physical Review B* **87**, 115212 (2013).

[20] E. Heifets, E. Kotomin, and V. A. Trepakov, Calculations for antiferrodistortive phase of $SrTiO_3$ perovskite: hybrid density functional study, *Journal of Physics: Condensed Matter* **18**, 4845 (2006).

[21] M. Marques, L. K. Teles, V. Anjos, L. M. R. Scolfaro, J. R. Leite, V. N. Freire, G. A. Farias, and E. F. da Silva, Full-relativistic calculations of the $SrTiO_3$ carrier effective masses and complex dielectric function, *Applied Physics Letters* **82**, 3074 (2003).

[22] J. F. Schooley, W. R. Hosler, and M. L. Cohen, Superconductivity in semiconducting $SrTiO_3$, *Physical Review Letters* **12**, 474 (1964).

[23] C. S. Koonce, M. L. Cohen, J. F. Schooley, W. R. Hosler, and E. R. Pfeiffer, Superconducting Transition Temperatures of Semiconducting $SrTiO_3$, *Physical Review* **163**, 380 (1967).

[24] X. Lin, Z. Zhu, B. Fauqué, and K. Behnia, Fermi surface of the most dilute superconductor, *Physical Review X* **3**, 021002 (2013).

[25] J. Bardeen, L. N. Cooper, and J. R. Schrieffer, Theory of Superconductivity, *Physical Review* **108**, 1175 (1957).

[26] L. P. Gor'kov, Phonon mechanism in the most dilute superconductor n-type $SrTiO_3$, *Proceedings of the National Academy of Sciences* **113**, 4646 (2016).

[27] D. M. Eagles, Possible pairing without superconductivity at low carrier concentrations in bulk and thin-film superconducting semiconductors, *Physical Review* **186**, 456 (1969).

[28] R. Nakamura and Y. Kanematsu, Femtosecond spectral snapshots based on electronic optical Kerr effect, *Review of Scientific Instruments* **75**, 636 (2004).

[29] A. Ohtomo and H. Y. Hwang, A high-mobility electron gas at the $LaAlO_3/SrTiO_3$ heterointerface, *Nature* **427**, 423 (2004).

[30] S. Thiel, G. Hammerl, A. Schmehl, C. W. Schneider, and J. Mannhart, Tunable quasi-two-dimensional electron gases in oxide heterostructures, *Science* **313**, 1942 (2006).

[31] M. Basletic, J. L. Maurice, C. Carretero, G. Herranz, O. Copie, M. Bibes, E. Jacquet, K. Bouzehouane, S. Fusil, and A. Barthelemy, Mapping the spatial distribution of charge carriers in $LaAlO_3/SrTiO_3$ heterostructures, *Nature Materials* **7**, 621 (2008).

[32] O. Copie, V. Garcia, C. Bödefeld, C. Carrétéro, M. Bibes, G. Herranz, E. Jacquet, J. L. Maurice, B. Vinter, S. Fusil, K. Bouzehouane, H. Jaffrès, and A. Barthélémy, Towards Two-Dimensional Metallic Behavior at $LaAlO_3/SrTiO_3$ Interfaces, *Physical Review Letters* **102**, 216804 (2009).

[33] C. W. Bark, D. A. Felker, Y. Wang, Y. Zhang, H. W. Jang, C. M. Folkman, J. W. Park, S. H. Baek, H. Zhou, D. D. Fong, X. Q. Pan, E. Y. Tsymbal, M. S. Rzchowski, and C. B. Eom, Tailoring a two-dimensional electron gas at the $LaAlO_3/SrTiO_3$ (001) interface by epitaxial strain, *Proceedings of the National Academy of Sciences of the United States of America* **108**, 4720 (2011).

[34] K. A. Brown, S. He, D. J. Eichelsdoerfer, M. Huang, I. Levy, H. Lee, S. Ryu, P. Irvin, J. Mendez-Arroyo, C.-B. Eom, C. A. Mirkin, and J. Levy, Giant conductivity switching of $LaAlO_3/SrTiO_3$ heterointerfaces governed by surface protonation, *Nature Communications* **7**, 10681 (2016).

[35] P. Irvin, J. P. Veazey, G. Cheng, S. Lu, C.-W. Bark, S. Ryu, C.-B. Eom, and J. Levy, Anomalous High Mobility in $LaAlO_3/SrTiO_3$ Nanowires, *Nano Letters* **13**, 364 (2013).

[36] G. Herranz, F. Sánchez, N. Dix, M. Scigaj, and J. Fontcuberta, High mobility conduction at (110) and (111) $LaAlO_3/SrTiO_3$ interfaces, *Scientific Reports* **2**, 758 (2012).

[37] N. Nakagawa, H. Y. Hwang, and D. A. Muller, Why some interfaces cannot be sharp, *Nat Mater* **5**, 204 (2006).

[38] A. Kalabukhov, R. Gunnarsson, J. Börjesson, E. Olsson, T. Claeson, and D. Winkler, Effect of oxygen vacancies in the $SrTiO_3$ substrate on the electrical properties of the $LaAlO_3$ / $SrTiO_3$ interface, *Physical Review B* **75**, 121404 (2007).

[39] P. R. Willmott, S. A. Pauli, R. Herger, C. M. Schleputz, D. Martoccia, B. D. Patterson, B. Delley, R. Clarke, D. Kumah, C. Cionca, and Y. Yacoby, Structural basis for the conducting interface between $LaAlO_3$ and $SrTiO_3$, *Physical Review Letters* **99**(2007).

[40] H. K. Sato, C. Bell, Y. Hikita, and H. Y. Hwang, Stoichiometry control of the electronic properties of the $LaAlO_3/SrTiO_3$ heterointerface, *Applied Physics Letters* **102**(2013).

[41] S. Frank, A. C. Michael, E. V. Mary, E. Mehmet, F. Thomas, E. K. Josée, L. M.-D. Judith, and G. B. Mark, Carrier density modulation by structural distortions at modified $LaAlO_3/SrTiO_3$ interfaces, *Journal of Physics: Condensed Matter* **25**, 175005 (2013).

[42] L. Yu and A. Zunger, A polarity-induced defect mechanism for conductivity and magnetism at polar--nonpolar oxide interfaces, *Nature Communications* **5**, 5118 (2014).

[43] C. Cen, S. Thiel, G. Hammerl, C. W. Schneider, K. E. Andersen, C. S. Hellberg, J. Mannhart, and J. Levy, Nanoscale control of an interfacial metal-insulator transition at room temperature, *Nature Materials* **7**, 298 (2008).

[44] N. Reyren, S. Thiel, A. D. Caviglia, L. F. Kourkoutis, G. Hammerl, C. Richter, C. W. Schneider, T. Kopp, A. S. Ruetschi, D. Jaccard, M. Gabay, D. A. Muller, J. M. Triscone, and J. Mannhart, Superconducting interfaces between insulating oxides, *Science* **317**, 1196 (2007).

[45] A. Brinkman, M. Huijben, M. Van Zalk, J. Huijben, U. Zeitler, J. C. Maan, W. G. Van der Wiel, G. Rijnders, D. H. A. Blank, and H. Hilgenkamp, Magnetic effects at the interface between non-magnetic oxides, *Nature Materials* **6**, 493 (2007).

[46] F. Bi, M. Huang, S. Ryu, H. Lee, C.-W. Bark, C.-B. Eom, P. Irvin, and J. Levy, Room-temperature electronically-controlled ferromagnetism at the $LaAlO_3/SrTiO_3$ interface, *Nature Communications* **5**, 5019 (2014).

[47] A. D. Caviglia, M. Gabay, S. Gariglio, N. Reyren, C. Cancellieri, and J. M. Triscone, Tunable Rashba Spin-Orbit Interaction at Oxide Interfaces, *Physical Review Letters* **104**, 126803 (2010).

[48] D. A. Dikin, M. Mehta, C. W. Bark, C. M. Folkman, C. B. Eom, and V. Chandrasekhar, Coexistence of Superconductivity and Ferromagnetism in Two Dimensions, *Physical Review Letters* **107**, 056802 (2011).

[49] Y. Chen, F. Trier, T. Kasama, D. V. Christensen, N. Bovet, Z. I. Balogh, H. Li, K. T. S. Thydén, W. Zhang, S. Yazdi, P. Norby, N. Pryds, and S. Linderoth, Creation of High

Mobility Two-Dimensional Electron Gases via Strain Induced Polarization at an Otherwise Nonpolar Complex Oxide Interface, *Nano Letters* **15**, 1849 (2015).

[50] S. Nazir, J. Cheng, and K. Yang, Creating Two-Dimensional Electron Gas in Nonpolar/Nonpolar Oxide Interface via Polarization Discontinuity: First-Principles Analysis of $CaZrO_3/SrTiO_3$ Heterostructure, *Acs Applied Materials & Interfaces* **8**, 390 (2016).

[51] J. Cheng, S. Nazir, and K. Yang, First-Principles Prediction of Two-Dimensional Electron Gas Driven by Polarization Discontinuity in Nonpolar/Nonpolar $AHfO_3/SrTiO_3$ (A = Ca, Sr, and Ba) Heterostructures, *Acs Applied Materials & Interfaces* **8**, 31959 (2016).

[52] G. Cheng, M. Tomczyk, S. Lu, J. P. Veazey, M. Huang, P. Irvin, S. Ryu, H. Lee, C. B. Eom, C. S. Hellberg, and J. Levy, Electron pairing without superconductivity, *Nature* **521**, 196 (2015).

[53] R. Waser, ed., *Nanotechnology: Volume 3 Information Technology I* (Wiley-VCH, 2008).

[54] S. Datta, *Electronic transport in mesoscopic systems*, Cambridge studies in semiconductor physics and microelectronic engineering (Cambridge University Press, Cambridge ; New York, 1995), pp. xv.

[55] F. D. M. Haldane, 'Luttinger liquid theory' of one-dimensional quantum fluids. I. Properties of the Luttinger model and their extension to the general 1D interacting spinless Fermi gas, *Journal of Physics C: Solid State Physics* **14**, 2585 (1981).

[56] C. L. Kane and M. P. A. Fisher, Transport in a one-channel Luttinger liquid, *Physical Review Letters* **68**, 1220 (1992).

[57] T. H. Maiman, Stimulated Optical Radiation in Ruby, *Nature* **187**, 493 (1960).

[58] L. E. Hargrove, R. L. Fork, and M. A. Pollack, Locking of He–Ne laser modes induced by synchronous intracavity modulation, *Applied Physics Letters* **5**, 4 (1964).

[59] E. P. Ippen, C. V. Shank, and A. Dienes, Passive mode locking of the cw dye laser, *Applied Physics Letters* **21**, 348 (1972).

[60] D. E. Spence, P. N. Kean, and W. Sibbett, 60-fsec pulse generation from a self-mode-locked Ti:sapphire laser, *Optics Letters* **16**, 42 (1991).

[61] D. H. Sutter, G. Steinmeyer, L. Gallmann, N. Matuschek, F. Morier-Genoud, U. Keller, V. Scheuer, G. Angelow, and T. Tschudi, Semiconductor saturable-absorber mirror–assisted Kerr-lens mode-locked Ti:sapphire laser producing pulses in the two-cycle regime, *Optics Letters* **24**, 631 (1999).

[62] R. Trebino and D. J. Kane, Using phase retrieval to measure the intensity and phase of ultrashort pulses: frequency-resolved optical gating, *Journal of the Optical Society of America A* **10**, 1101 (1993).

[63] C. Iaconis, V. Wong, and I. A. Walmsley, Direct interferometric techniques for characterizing ultrashort optical pulses, *Ieee Journal of Selected Topics in Quantum Electronics* **4**, 285 (1998).

[64] K. A. Walowicz, I. Pastirk, V. V. Lozovoy, and M. Dantus, Multiphoton Intrapulse Interference. 1. Control of Multiphoton Processes in Condensed Phases, *The Journal of Physical Chemistry A* **106**, 9369 (2002).

[65] J. M. Dela Cruz, I. Pastirk, V. V. Lozovoy, K. A. Walowicz, and M. Dantus, Multiphoton Intrapulse Interference 3: Probing Microscopic Chemical Environments, *The Journal of Physical Chemistry A* **108**, 53 (2004).

[66] I. Pastirk, J. M. D. Cruz, K. A. Walowicz, V. V. Lozovoy, and M. Dantus, Selective two-photon microscopy with shaped femtosecond pulses, *Optics Express* **11**, 1695 (2003).

[67] J. M. Dela Cruz, I. Pastirk, M. Comstock, V. V. Lozovoy, and M. Dantus, Use of coherent control methods through scattering biological tissue to achieve functional imaging, *Proceedings of the National Academy of Sciences of the United States of America* **101**, 16996 (2004).

[68] A. M. Weiner, Ultrafast optical pulse shaping: A tutorial review, *Optics Communications* **284**, 3669 (2011).

[69] F. F. John, S. Brian, H. Feng, G. Dale, B. Robert, O. Filipe, and Z. David, THz imaging and sensing for security applications—explosives, weapons and drugs, *Semiconductor Science and Technology* **20**, S266 (2005).

[70] G. Mourou, C. V. Stancampiano, A. Antonetti, and A. Orszag, Picosecond microwave pulses generated with a subpicosecond laser ‐ driven semiconductor switch, *Applied Physics Letters* **39**, 295 (1981).

[71] M. Bass, P. A. Franken, J. F. Ward, and G. Weinreich, Optical Rectification, *Physical Review Letters* **9**, 446 (1962).

[72] A. Masaaki, Ultra-Broadband Terahertz Wave Detection Using Photoconductive Antenna, *Japanese Journal of Applied Physics* **47**, 8221 (2008).

[73] S. Casalbuoni, B. Schmidt, P. Schmüser, V. Arsov, and S. Wesch, Ultrabroadband terahertz source and beamline based on coherent transition radiation, *Physical Review Special Topics - Accelerators and Beams* **12**, 030705 (2009).

[74] D. Hashimshony, A. Zigler, and K. Papadopoulos, Conversion of Electrostatic to Electromagnetic Waves by Superluminous Ionization Fronts, *Physical Review Letters* **86**, 2806 (2001).

[75] D. W. V. d. Weide, J. Murakowski, and F. Keilmann, Gas-absorption spectroscopy with electronic terahertz techniques, *Ieee Transactions on Microwave Theory and Techniques* **48**, 740 (2000).

[76] F. Maiwald, S. Martin, J. Bruston, A. Maestrini, T. Crawford, and P. H. Siegel, 2.7 THz waveguide tripler using monolithic membrane diodes, in *2001 IEEE MTT-S International Microwave Sympsoium Digest (Cat. No.01CH37157)*, 2001), 1637.

[77] E. R. Brown, K. A. McIntosh, K. B. Nichols, and C. L. Dennis, Photomixing up to 3.8 THz in low-temperature-grown GaAs, *Applied Physics Letters* **66**, 285 (1995).

[78] J. M. Gary, R. S. John, L. N. A. Matthew, A. B. Edwin, C. Gordon, R. E. Neal, F. G. Paul, H. Martin, E. H. John, C. K. Steven, G. K. David, A. N. David, M. P. Brian, P. René, S. Rudolf, L. S. Ronald, T. Volker, W. Zhong, W. Gisbert, and Z. Yun Fei, The Submillimeter Wave Astronomy Satellite: Science Objectives and Instrument Description, *The Astrophysical Journal Letters* **539**, L77 (2000).

[79] Y. Ma, M. Huang, S. Ryu, C. W. Bark, C.-B. Eom, P. Irvin, and J. Levy, Broadband Terahertz generation and detection at 10 nm scale, *Nano Letters* **13**, 2884 (2013).

[80] T. Feng, Anomalous photoelectronic processes in $SrTiO_3$, *Physical Review B* **25**, 627 (1982).

[81] P. Irvin, Y. J. Ma, D. F. Bogorin, C. Cen, C. W. Bark, C. M. Folkman, C. B. Eom, and J. Levy, Rewritable nanoscale oxide photodetector, *Nature Photonics* **4**, 849 (2010).

[82] C. Cen, S. Thiel, J. Mannhart, and J. Levy, Oxide nanoelectronics on demand, *Science* **323**, 1026 (2009).

[83] G. Cheng, P. F. Siles, F. Bi, C. Cen, D. F. Bogorin, C. W. Bark, C. M. Folkman, J. W. Park, C. B. Eom, G. Medeiros-Ribeiro, and J. Levy, Sketched oxide single-electron transistor, *Nature Nanotechnology* **6**, 343 (2011).

[84] M. Tomczyk, G. Cheng, H. Lee, S. Lu, A. Annadi, J. P. Veazey, M. Huang, P. Irvin, S. Ryu, C.-B. Eom, and J. Levy, Micrometer-scale ballistic transport of electron pairs in $LaAlO_3/SrTiO_3$ nanowires, *Physical Review Letters* **117**, 096801 (2016).

[85] D. F. Bogorin, C. W. Bark, H. W. Jang, C. Cen, C. M. Folkman, C.-B. Eom, and J. Levy, Nanoscale rectification at the $LaAlO_3/SrTiO_3$ interface, *Applied Physics Letters* **97**, 013102 (2010).

[86] F. Bi, D. F. Bogorin, C. Cen, C. W. Bark, J. W. Park, C. B. Eom, and J. Levy, "Water-cycle" mechanism for writing and erasing nanostructures at the $LaAlO_3/SrTiO_3$ interface, *Applied Physics Letters* **97**, 173110 (2010).

[87] A. D. Caviglia, S. Gariglio, N. Reyren, D. Jaccard, T. Schneider, M. Gabay, S. Thiel, G. Hammerl, J. Mannhart, and J. M. Triscone, Electric field control of the $LaAlO_3/SrTiO_3$ interface ground state, *Nature* **456**, 624 (2008).

[88] M. Ben Shalom, M. Sachs, D. Rakhmilevitch, A. Palevski, and Y. Dagan, Tuning spin-orbit coupling and superconductivity at the $SrTiO_3/LaAlO_3$ interface: a magnetotransport study, *Physical Review Letters* **104**, 126802 (2010).

[89] D. V. Christensen, M. von Soosten, F. Trier, T. S. Jespersen, A. Smith, Y. Chen, and N. Pryds, Controlling the Carrier Density of $SrTiO_3$-Based Heterostructures with Annealing, *Advanced Electronic Materials* **3**, 1700026 (2017).

[90] J. S. Langer and V. Ambegaokar, Intrinsic Resistive Transition in Narrow Superconducting Channels, *Physical Review* **164**, 498 (1967).

[91] W. J. Skocpol, M. R. Beasley, and M. Tinkham, Self‐heating hotspots in superconducting thin‐film microbridges, *Journal of Applied Physics* **45**, 4054 (1974).

[92] M. Tinkham, J. U. Free, C. N. Lau, and N. Markovic, Hysteretic IV curves of superconducting nanowires, *Physical Review B* **68**, 134515 (2003).

[93] J. A. Bert, K. C. Nowack, B. Kalisky, H. Noad, J. R. Kirtley, C. Bell, H. K. Sato, M. Hosoda, Y. Hikita, H. Y. Hwang, and K. A. Moler, Gate-tuned superfluid density at the superconducting $LaAlO_3/SrTiO_3$ interface, *Physical Review B* **86**, 060503 (2012).

[94] J. P. Veazey, G. Cheng, P. Irvin, C. Cen, D. F. Bogorin, F. Bi, M. Huang, C.-W. Bark, S. Ryu, K.-H. Cho, C.-B. Eom, and J. Levy, Oxide-based platform for reconfigurable superconducting nanoelectronics, *Nanotechnology* **24**, 375201 (2013).

[95] M. Honig, J. A. Sulpizio, J. Drori, A. Joshua, E. Zeldov, and S. Ilani, Local electrostatic imaging of striped domain order in $LaAlO_3/SrTiO_3$, *Nature Materials* **12**, 1112 (2013).

[96] S. Mathew, A. Annadi, T. K. Chan, T. C. Asmara, D. Zhan, X. R. Wang, S. Azimi, Z. Shen, A. Rusydi, Ariando, M. B. H. Breese, and T. Venkatesan, Tuning the Interface Conductivity of $LaAlO_3/SrTiO_3$ Using Ion Beams: Implications for Patterning, *ACS Nano* **7**, 10572 (2013).

[97] C. He, T. D. Sanders, M. T. Gray, F. J. Wong, V. V. Mehta, and Y. Suzuki, Metal-insulator transitions in epitaxial $LaVO_3$ and $LaTiO_3$ films, *Physical Review B* **86**, 081401 (2012).

[98] A. Annadi, A. Putra, Z. Q. Liu, X. Wang, K. Gopinadhan, Z. Huang, S. Dhar, T. Venkatesan, and Ariando, Electronic correlation and strain effects at the interfaces between polar and nonpolar complex oxides, *Physical Review B* **86**, 085450 (2012).

[99] C. P. Chang, J. G. Lin, H. T. Jeng, S. L. Cheng, W. F. Pong, Y. C. Shao, Y. Y. Chin, H. J. Lin, C. W. Chen, J. R. Yang, C. H. Chen, and M. W. Chu, Atomic-scale observation of a graded polar discontinuity and a localized two-dimensional electron density at an insulating oxide interface, *Physical Review B* **87**, 075129 (2013).

[100] P. Xu, W. Han, P. M. Rice, J. Jeong, M. G. Samant, K. Mohseni, H. L. Meyerheim, S. Ostanin, I. V. Maznichenko, I. Mertig, E. K. U. Gross, A. Ernst, and S. S. P. Parkin, Reversible Formation of 2D Electron Gas at the $LaFeO_3/SrTiO_3$ Interface via Control of Oxygen Vacancies, *Advanced Materials* **29**, 1604447 (2017).

[101] K. Shibuya, T. Ohnishi, M. Lippmaa, and M. Oshima, Metallic conductivity at the $CaHfO_3/SrTiO_3$ interface, *Applied Physics Letters* **91**, 232106 (2007).

[102] S. Zeng, W. Lü, Z. Huang, Z. Liu, K. Han, K. Gopinadhan, C. Li, R. Guo, W. Zhou, H. H. Ma, L. Jian, T. Venkatesan, and Ariando, Liquid-Gated High Mobility and Quantum Oscillation of the Two-Dimensional Electron Gas at an Oxide Interface, *ACS Nano* **10**, 4532 (2016).

[103] M. Yang, K. Han, O. Torresin, M. Pierre, S. Zeng, Z. Huang, T. V. Venkatesan, M. Goiran, J. M. D. Coey, Ariando, and W. Escoffier, High field magneto-transport in two-dimensional electron gas $LaAlO_3/SrTiO_3$, *Applied Physics Letters* **109**, 122106 (2016).

[104] Y. Kozuka, M. Kim, C. Bell, B. G. Kim, Y. Hikita, and H. Y. Hwang, Two-dimensional normal-state quantum oscillations in a superconducting heterostructure, *Nature* **462**, 487 (2009).

[105] B. Jalan, S. Stemmer, S. Mack, and S. J. Allen, Two-dimensional electron gas in δ-doped $SrTiO_3$, *Physical Review B* **82**, 081103 (2010).

[106] Y. Matsubara, K. S. Takahashi, M. S. Bahramy, Y. Kozuka, D. Maryenko, J. Falson, A. Tsukazaki, Y. Tokura, and M. Kawasaki, Observation of the quantum Hall effect in δ-doped $SrTiO_3$, *Nature Communications* **7**, 11631 (2016).

[107] Y. Frenkel, N. Haham, Y. Shperber, C. Bell, Y. Xie, Z. Chen, Y. Hikita, H. Y. Hwang, and B. Kalisky, Anisotropic Transport at the $LaAlO_3/SrTiO_3$ Interface Explained by Microscopic Imaging of Channel-Flow over $SrTiO_3$ Domains, *Acs Applied Materials & Interfaces* **8**, 12514 (2016).

[108] M. Tonouchi, Cutting-edge terahertz technology, *Nature Photonics* **1**, 97 (2007).

[109] B. Ferguson and X.-C. Zhang, Materials for terahertz science and technology, *Nature Materials* **1**, 26 (2002).

[110] R. Ulbricht, E. Hendry, J. Shan, T. F. Heinz, and M. Bonn, Carrier dynamics in semiconductors studied with time-resolved terahertz spectroscopy, *Reviews of Modern Physics* **83**, 543 (2011).

[111] K.-E. Peiponen, A. Zeitler, and M. Kuwata-Gonokami, eds., *Terahertz spectroscopy and imaging* (Springer-Verlag Berlin Heidelberg, 2013).

[112] D. Mittleman, ed., *Sensing with terahertz radiation*, Springer Series in Optical Sciences (Springer-Verlag Berlin Heidelberg, 2003).

[113] M. C. Lemme, T. J. Echtermeyer, M. Baus, and H. Kurz, A Graphene Field-Effect Device, *Ieee Electron Device Letters* **28**, 282 (2007).

[114] G. Gallot, S. P. Jamison, R. W. McGowan, and D. Grischkowsky, Terahertz waveguides, *Journal of the Optical Society of America B* **17**, 851 (2000).

[115] N. Laman, S. S. Harsha, and D. Grischkowsky, Narrow-Line Waveguide Terahertz Time-Domain Spectroscopy of Aspirin and Aspirin Precursors, *Applied Spectroscopy* **62**, 319 (2008).

[116] N. Laman, S. S. Harsha, D. Grischkowsky, and J. S. Melinger, High-Resolution Waveguide THz Spectroscopy of Biological Molecules, *Biophysical Journal* **94**, 1010 (2008).

[117] J. S. Melinger, N. Laman, and D. Grischkowsky, The underlying terahertz vibrational spectrum of explosives solids, *Applied Physics Letters* **93**, 011102 (2008).

[118] J. F. O'Hara, R. Singh, I. Brener, E. Smirnova, J. Han, A. J. Taylor, and W. Zhang, Thin-film sensing with planar terahertz metamaterials: sensitivity and limitations, *Optics Express* **16**, 1786 (2008).

[119] M. A. Seo, H. R. Park, S. M. Koo, D. J. Park, J. H. Kang, O. K. Suwal, S. S. Choi, P. C. M. Planken, G. S. Park, N. K. Park, Q. H. Park, and D. S. Kim, Terahertz field enhancement by a metallic nano slit operating beyond the skin-depth limit, *Nature Photonics* **3**, 152 (2009).

[120] H.-R. Park, K. J. Ahn, S. Han, Y.-M. Bahk, N. Park, and D.-S. Kim, Colossal Absorption of Molecules Inside Single Terahertz Nanoantennas, *Nano Letters* **13**, 1782 (2013).

[121] K. Kneipp, Y. Wang, H. Kneipp, L. T. Perelman, I. Itzkan, R. R. Dasari, and M. S. Feld, Single Molecule Detection Using Surface-Enhanced Raman Scattering (SERS), *Physical Review Letters* **78**, 1667 (1997).

[122] S. Nie and S. R. Emory, Probing Single Molecules and Single Nanoparticles by Surface-Enhanced Raman Scattering, *Science* **275**, 1102 (1997).

[123] D.-K. Lim, K.-S. Jeon, H. M. Kim, J.-M. Nam, and Y. D. Suh, Nanogap-engineerable Raman-active nanodumbbells for single-molecule detection, *Nature Materials* **9**, 60 (2009).

[124] F. De Angelis, M. Patrini, G. Das, I. Maksymov, M. Galli, L. Businaro, L. C. Andreani, and E. Di Fabrizio, A Hybrid Plasmonic−Photonic Nanodevice for Label-Free Detection of a Few Molecules, *Nano Letters* **8**, 2321 (2008).

[125] J. Pérez-Juste, I. Pastoriza-Santos, L. M. Liz-Marzán, and P. Mulvaney, Gold nanorods: Synthesis, characterization and applications, *Coordination Chemistry Reviews* **249**, 1870 (2005).

[126] R. Gans, Über die Form ultramikroskopischer Goldteilchen, *Annalen Der Physik* **342**, 881 (1912).

[127] S. Link and M. A. El-Sayed, Shape and size dependence of radiative, non-radiative and photothermal properties of gold nanocrystals, *International Reviews in Physical Chemistry* **19**, 409 (2000).

[128] M. Hu, J. Chen, Z.-Y. Li, L. Au, G. V. Hartland, X. Li, M. Marquez, and Y. Xia, Gold nanostructures: engineering their plasmonic properties for biomedical applications, *Chemical Society Reviews* **35**, 1084 (2006).

[129] A. D. Boardman, ed., *Electromagnetic Surface Modes* (John Wiley & Sons, New York, 1982).

[130] A. V. Zayats, I. I. Smolyaninov, and A. A. Maradudin, Nano-optics of surface plasmon polaritons, *Physics Reports* **408**, 131 (2005).

[131] X. Huang, S. Neretina, and M. A. El-Sayed, Gold Nanorods: From Synthesis and Properties to Biological and Biomedical Applications, *Advanced Materials* **21**, 4880 (2009).

[132] J. A. Schuller, E. S. Barnard, W. Cai, Y. C. Jun, J. S. White, and M. L. Brongersma, Plasmonics for extreme light concentration and manipulation, *Nature Materials* **9**, 193 (2010).

[133] D. K. Gramotnev and S. I. Bozhevolnyi, Plasmonics beyond the diffraction limit, *Nature Photonics* **4**, 83 (2010).

[134] V. Giannini, A. I. Fernández-Domínguez, S. C. Heck, and S. A. Maier, Plasmonic Nanoantennas: Fundamentals and Their Use in Controlling the Radiative Properties of Nanoemitters, *Chemical Reviews* **111**, 3888 (2011).

[135] W.-J. Lee, J. W. Ma, J. M. Bae, K.-S. Jeong, M.-H. Cho, C. Kang, and J.-S. Wi, Strongly Enhanced THz Emission caused by Localized Surface Charges in Semiconducting Germanium Nanowires, *Scientific Reports* **3**, 1984 (2013).

[136] S. Diefenbach, N. Erhard, J. Schopka, A. Martin, C. Karnetzky, D. Iacopino, and A. W. Holleitner, Polarization dependent, surface plasmon induced photoconductance in gold nanorod arrays, *physica status solidi (RRL) – Rapid Research Letters* **8**, 264 (2014).

[137] W. Cao, C. Song, T. E. Lanier, R. Singh, J. F. O'Hara, W. M. Dennis, Y. Zhao, and W. Zhang, Tailoring terahertz plasmons with silver nanorod arrays, *Scientific Reports* **3**, 1766 (2013).

[138] R. A. Kaindl, M. A. Carnahan, D. Hägele, R. Lövenich, and D. S. Chemla, Ultrafast terahertz probes of transient conducting and insulating phases in an electron–hole gas, *Nature* **423**, 734 (2003).

[139] M. Rini, R. a. Tobey, N. Dean, J. Itatani, Y. Tomioka, Y. Tokura, R. W. Schoenlein, and A. Cavalleri, Control of the electronic phase of a manganite by mode-selective vibrational excitation, *Nature* **449**, 72 (2007).

[140] P. Y. Han and X. C. Zhang, Free-space coherent broadband terahertz time-domain spectroscopy, *Measurement Science and Technology* **12**, 1747 (2001).

[141] T. Kleine-Ostmann and T. Nagatsuma, A Review on Terahertz Communications Research, *Journal of Infrared, Millimeter, and Terahertz Waves* **32**, 143 (2011).

[142] T. Feurer, J. C. Vaughan, and K. A. Nelson, Spatiotemporal Coherent Control of Lattice Vibrational Waves, *Science* **299**, 374 (2003).

[143] S. Hunsche, M. Koch, I. Brener, and M. C. Nuss, THz near-field imaging, *Optics Communications* **150**, 22 (1998).

[144] A. Bitzer, A. Ortner, and M. Walther, Terahertz near-field microscopy with subwavelength spatial resolution based on photoconductive antennas, *Applied Optics* **49**, E1 (2010).

[145] M. Eisele, T. L. Cocker, M. A. Huber, M. Plankl, L. Viti, D. Ercolani, L. Sorba, M. S. Vitiello, and R. Huber, Ultrafast multi-terahertz nano-spectroscopy with sub-cycle temporal resolution, *Nature Photonics* **8**, 841 (2014).

[146] T. L. Cocker, V. Jelic, M. Gupta, S. J. Molesky, J. A. J. Burgess, G. D. L. Reyes, L. V. Titova, Y. Y. Tsui, M. R. Freeman, and F. A. Hegmann, An ultrafast terahertz scanning tunnelling microscope, *Nature Photonics* **7**, 620 (2013).

[147] G. Jnawali, L. Chen, M. Huang, H. Lee, S. Ryu, J. P. Podkaminer, C.-B. Eom, P. Irvin, and J. Levy, Photoconductive response of a single Au nanorod coupled to $LaAlO_3/SrTiO_3$ nanowires, *Applied Physics Letters* **106**, 211101 (2015).

[148] Y. Kanemitsu and Y. Yamada, Light emission from $SrTiO_3$, *physica status solidi (b)* **248**, 416 (2010).

[149] A. Yamakata, J. J. M. Vequizo, and M. Kawaguchi, Behavior and Energy State of Photogenerated Charge Carriers in Single-Crystalline and Polycrystalline Powder $SrTiO_3$ Studied by Time-Resolved Absorption Spectroscopy in the Visible to Mid-Infrared Region, *The Journal of Physical Chemistry C* **119**, 1880 (2015).

[150] T. Günter, A. Rubano, D. Paparo, M. Lilienblum, L. Marrucci, F. Miletto Granozio, U. Scotti di Uccio, R. Jany, C. Richter, J. Mannhart, and M. Fiebig, Spatial inhomogeneities at the $LaAlO_3/SrTiO_3$ interface: Evidence from second harmonic generation, *Physical Review B* **86**, 235418 (2012).

[151] A. Rubano, C. Aruta, U. S. d. Uccio, F. M. Granozio, L. Marrucci, T. Günter, T. Fink, M. Fiebig, and D. Paparo, Electronic states at polar/nonpolar interfaces grown on $SrTiO_3$ studied by optical second harmonic generation, *Physical Review B* **88**, 245434 (2013).

[152] R. Huber, A. Brodschelm, F. Tauser, and A. Leitenstorfer, Generation and field-resolved detection of femtosecond electromagnetic pulses tunable up to 41 THz, *Applied Physics Letters* **76**, 3191 (2000).

[153] L. Ju, B. Geng, J. Horng, C. Girit, M. Martin, Z. Hao, H. A. Bechtel, X. Liang, A. Zettl, Y. R. Shen, and F. Wang, Graphene plasmonics for tunable terahertz metamaterials, *Nature Nanotechnology* **6**, 630 (2011).

[154] G. Jnawali, M. Huang, J.-F. Hsu, H. Lee, J.-W. Lee, P. Irvin, C.-B. Eom, B. D'Urso, and J. Levy, Room-Temperature Quantum Transport Signatures in Graphene/$LaAlO_3$/$SrTiO_3$ Heterostructures, *Advanced Materials* **29**, 1603488 (2017).

[155] J. Li, J.-F. Hsu, H. Lee, S. Tripathi, Q. Guo, L. Chen, M. Huang, S. Dhingra, J.-W. Lee, C.-B. Eom, P. Irvin, J. Levy, and B. D'Urso, Method for Transferring High-Mobility CVD-Grown Graphene with Perfluoropolymers, *arXiv:1606.08802* (2016).

[156] M. Huang, G. Jnawali, J.-F. Hsu, S. Dhingra, H. Lee, S. Ryu, F. Bi, F. Ghahari, J. Ravichandran, L. Chen, P. Kim, C.-B. Eom, B. D'Urso, P. Irvin, and J. Levy, Electric field effects in graphene/$LaAlO_3$/$SrTiO_3$ heterostructures and nanostructures, *APL Materials* **3**, 062502 (2015).

[157] S. Dhingra, J.-F. Hsu, I. Vlassiouk, and B. D'Urso, Chemical vapor deposition of graphene on large-domain ultra-flat copper, *Carbon* **69**, 188 (2014).

[158] S. Hu, M. Lozada-Hidalgo, F. C. Wang, A. Mishchenko, F. Schedin, R. R. Nair, E. W. Hill, D. W. Boukhvalov, M. I. Katsnelson, R. A. W. Dryfe, I. V. Grigorieva, H. A. Wu, and A. K. Geim, Proton transport through one-atom-thick crystals, *Nature* **516**, 227 (2014).

[159] F. Bi, M. Huang, C.-W. Bark, S. Ryu, S. Lee, C.-B. Eom, P. Irvin, and J. Levy, Electro-mechanical response of top-gated $LaAlO_3$/$SrTiO_3$, *Journal of Applied Physics* **119**, 025309 (2016).